Aalborg Universitet

AALBORG UNIVERSITY

DENMARK

Power Electronic Systems for Switched Reluctance Generator based Wind Farms and DC Networks

Park, Kiwoo

Publication date:
2014

Document Version
Publisher's PDF, also known as Version of record

Power Electronic Systems

for Switched Reluctance Generator based

Wind Farms and DC Networks

Kiwoo Park

PhD Dissertation

Aalborg, September 2014

DEPARTMENT OF ENERGY TECHNOLOGY

AALBORG UNIVERSITY

Power Electronic Systems

for Switched Reluctance Generator based

Wind Farms and DC Networks

By

Kiwoo Park

Department of Energy Technology

A Dissertation Submitted to

The Faculty of Engineering, Science and Medicine, Aalborg University

in Partial Fulfillment for the Degree of Doctor of Philosophy

September 2014

Aalborg, Denmark

Statement

Thesis title:

Power Electronic Systems for Switched Reluctance Generator based Wind Farms and DC Networks

Name of PhD student:

Kiwoo Park

Name and title of supervisor and any other supervisors:

Professor Zhe Chen

Assessment committee:

Professor Stig Munk-Nielsen (chairman), Aalborg University, Denmark

Professor Alfred Rufer, Ecole Polytechnique Federal de Lausanne (EPFL), Switzerland

Professor Poul Ejnar Sørensen, Technical University of Denmark (DTU), Denmark

PhD. defense date:

31. October. 2014

List of published papers:

A. Journal Papers

[1]   Xiao Liu, Kiwoo Park, and Zhe Chen, "A novel excitation assistance switched reluctance wind power generator", *IEEE Trans. on Magnetics*, Accepted.

[2]   Kiwoo Park and Zhe Chen, "Control and dynamic analysis of a parallel-connected SAB dc-dc converter for dc-grid wind farm application,"

submitted to *IET Power Electronics* and provisionally accepted with minor review.

[3]   Kiwoo Park and Zhe Chen, "A double uneven power converter based dc-dc converter for high-power dc grid systems," submitted to *IEEE Trans. on Industrial Electronics* and under a reviewing process.

B. Conference Papers

[4]   Kiwoo Park and Zhe Chen, "Self-tuning fuzzy logic control of a switched reluctance generator for wind energy applications" in Proc. *3rd IEEE International Symposium on Power Electronics for Distributed Generation Systems (PEDG)*, pp. 357-363, Jun 2012.

[5]   Kiwoo Park and Zhe Chen, "Analysis and design of a parallel-connected single active bridge dc-dc converter for high-power wind farm application" in Proc. *15th European Conference on Power Electronics and Applications (EPE)*, pp. 1-10, Sep. 2013.

[6]   Kiwoo Park, Xiao Liu, and Zhe Chen, "A non-unity torque sharing function for torque ripple minimization of switched reluctance generators" in Proc. *15th European Conference on Power Electronics and Applications (EPE)*, pp. 1-10, Sep. 2013.

[7]   Kiwoo Park and Zhe Chen, "Open-circuit fault detection and tolerant operation for a parallel-connected SAB dc-dc converter" in Proc. *Applied Power Electronics Conference and Exposition (APEC)*, pp. 1966-1972, Mar. 2014.

[8]   Kiwoo Park and Zhe Chen, "A Double Uneven Power Converter based DC-DC Converter," submitted to *Applied Power Electronics Conference and Exposition (APEC)* 2015.

This present report combined with the above listed scientific papers has been submitted for assessment in partial fulfilment of the PhD degree. The scientific papers are not included in this version due to copyright issues. Detailed publication information is provided above and the interested reader is referred to the original published papers. As part of the assessment, co-author statements have been made available to the assessment committee and are also available at the Faculty of Engineering and Science, Aalborg University.

Acknowledgement

I would like to express my sincere gratitude and appreciation to my PhD supervisor Professor Zhe Chen for his kindness, patience, suggestions and encouragement throughout the whole PhD study. His invaluable support, understanding and expertise have been very important in completing this work.

I also would like to thank Professor Kyo-Beum Lee from Ajou University in Korea. He has always been giving me a lot of guidance and offered me the opportunity to study abroad, here, in Denmark.

Furthermore, many thanks go to my friends and colleagues in the Department of Energy Technology, especially Iker Diaz de Cerio Mendaza, Pietro Raboni, Andres Revilla Aguilar, Zakir Hussain Rather, Xiao Liu, Weihao Hu, Xiongfei Wang, Uimin Choi, and JunBum Kwon for their help in work and life.

Last but not least, I want to thank my parents, my only sister, and my wife, Sera, for their love and support.

Kiwoo Park

September, 2014

Aalborg

Abstract

Wind power technology, as the most competitive renewable energy technology, is quickly developing. The wind turbine size is growing and the grid penetration of wind power is increasing rapidly. Recently, the developments on wind power technology pay more attentions on efficiency and reliability. Under these circumstances, research on dc network connection with a novel wind power generator system is presented in this thesis, which mainly consists of two major parts: control of a Switched Reluctance Generator (SRG) system and development of high-power dc-dc converters for a dc network system in a wind farm.

The SRG, which eliminates permanent magnets, brushes, commutators, and coil windings in the rotor, could be a promising wind power generator. It has various desirable features, such as simple and solid structure, easiness of maintenance, fault tolerance, and low cost. These features are suitable for generators in wind turbine systems. However, despite all these advantageous features, the SRG has not been widely employed in wind energy applications. The most renowned technical disadvantages of the SRG are its nonlinearity and high torque ripples, which should be overcome to promote the application of the SRG in wind energy conversion systems.

To overcome the nonlinear characteristics of the SRG, which makes it difficult to achieve satisfactory control performance, a novel SRG speed controller based on self-tuning Fuzzy Logic Control (FLC) is proposed. The proposed controller utilizes the FLC with a self-tuning mechanism to improve the performance of controlling the speed of the SRG. Furthermore, a novel non-unity Torque Sharing Function (TSF) is proposed to minimize the torque ripple over a wide speed range of operation. Unlike the traditional TSFs, the proposed TSF injects deliberate ripple components into the torque reference to compensate the ripples in the actual output torque. The effectiveness and resulting improvement in the performance of both the proposed speed controller and the torque minimization technique are demonstrated by simulation results.

The modern power electronic interfaces enable various renewable energy sources, such as Photovoltaic (PV) and wind, to produce dc power directly. In addition, battery-based energy storage systems inherently operate with dc power. Hence, dc network (dc-grid) systems, which connect these dc sources and storages directly using dc networks, are gaining

much attention. The dc network system has a great potential to outdo the traditional ac systems in many technical challenges and could be highly profitable especially for offshore wind farm applications, where the size and weight of the components are crucial to the entire system costs in terms of substructure requirements, shipping, and installation.

The success of the dc network system is critically dependent upon high-efficient and high-power dc-dc converters. However, no practical high-power (MW-levels) dc-dc converter is commercially available yet. Although lots of research on the dc-dc converters for high-power applications has been carried out to improve their performance, efficiency, and reliability, there still exist several major obstacles, which hamper the further growth of the converter's power level, such as high power losses in the switching devices and large filter inductance requirement. To overcome these problems, two novel high-power dc-dc converter topologies are proposed and analyzed in this thesis: Parallel-Connected Single Active Bridge (PCSAB) dc-dc converter and Double Uneven Power (DUP) converter based dc-dc converter. Various simulation studies and experimental results are presented to verify the feasibility and operational principles of the proposed converters.

Finally, modelling and control of a dc-grid wind farm using one of the proposed dc-dc converters are presented. An average model provides insight into the overall performance of the system. Meanwhile, a switching model provides much detailed information, such as actual peak values of current and voltage ripples in the system. The control of the dc-grid wind farm is developed based on the obtained models and evaluated through various simulation studies. The developed models and control methods are expected to be useful for further studies on the operation of the dc-grid wind farm under various input wind speeds and/or fault conditions.

Dansk Resumé

Den mest konkurrencedygtige vedvarende energiteknologi, vindenergi, er i hurtig udvikling. Vindmøllernes størrelser vokser, og integrationen af vindenergi i elnettet er ligeledes tiltagende. Meget fokus er i øjeblikket rettet mod effektiviteten og reliabiliteten ved udnyttelse af denne energiform. Derfor præsenterer denne afhandling research omkring jævnstrømsnetværksforbindelse med et nyt vindkraftgeneratorsystem. Afhandlingen består af to hoveddele: Kontrol af Switched Reluctance Generator System (SRG) og udvikling af dc-dc transformer til jævnstrømsnetværk i vindmøllepark.

SRG-systemet som afløser permanent magnetering, børster, strømfordelere og spolevikling i rotoren, kan være en lovende løsning som vindenergigenerator. Det har mange gode og brugbare egenskaber, som for eksempel en simpel og solid struktur, det er let at håndtere, har fejltolerance og lave omkostninger. Disse egenskaber gør systemet velegnet som generatorer i vindmøllesystemer. Alligevel, trods disse fordelagtige egenskaber, er SRG-systemer endnu ikke blevet anvendt til vindenergi i et særligt stort omfang. Den største ulempe som kendetegner SRG-systemet er dens ulineære drejningsmomentskrusninger / torsionskraftskrusninger, hvilket er en ulempe som må løses, for at SRG-systemet kan benyttes til vindenergikonverteringssystemer.

For at løse ovenstående problem, som gør det svært at opnå tilfredsstillende kontrolydeevne, foreslås en ny SRG hastighedsstyreenhed, Fuzzy Logic Control (FLC), som er baseret på selv-justering. Den foreslåede styreenhed anvender FLC med en selv-justerbar mekanisme til at gøre kontrolydeevnen bedre i forhold til kontrol af hastigheden af SRG-systemet. Ydermere foreslås en ny non-unity Torque Sharing Function (TSF) med det formål at minimere torsionskraftskrusningen over et bredt drifts-omdrejningsområde. I modsætning til den traditionelle TSF, injicerer den foreslåede TSF tilsigtede krusningskomponenter ind i torsionskraften/drejningsmomentet for at kompensere for krusningseffekterne i den/det faktiske torsionskraftsresultat/drejningsmomentsresultat. Effektiviteten og den dermed forbedrede ydeevne af både den foreslåede hastighedsstyreenhed og torsionsminimerings-teknikken er begge demonstrerede med simuleringsresultater.

Moderne elektroniks grænseflader gør det muligt at producere jævnstrøm direkte ved hjælp af adskillelige vedvarende energityper, så som vindenergi og Photovoltaic (PV).

Ydermere opererer batteribaserede energi-lagringssystemer med jævnstrøm. Som følge deraf, er meget opmærksomhed rettet mod jævnstrømsnetværksystemer (elnet) som skaber direkte forbindelse mellem disse jævnstrømskilder og lagring. Jævnstrømsnetværket har stort potentiale til at erstatte det traditionelle vekselstømssystem og kan blive særligt udbytterig hvis anvendt til havmølleparker, hvor størrelsen og vægten af komponenterne spiller en vigtig rolle for systemets omkostninger i forhold til konstruktionskrav, fragt og installation.

Jævnstrømsnetværkets succes er dybt afhængigt af høj-effektive og højspændings dc-dc konverteringsapparater. Dog er praktiske højspændings dc-dc konverteringsapparater (MW-levels) endnu ikke kommercielt tilgængelige. På trods af, at meget research er lavet omkring forbedring af dc-dc konverteringsapparaters ydeevne, effektivitet og reliabilitet til brug for højspænding, findes der stadig store udfordringer hvilket hæmmer konverteringsapparatets effektniveau. Dette er udfordringer som energitab i koblingsudstyr og stort filter-induktans. For at løse disse problemer er to nye højspændings dc-dc konverteringstypologier foreslået og analyseret: Parallelforbundne Single Active Bridge (PCSAB) dc-dc konverteringsapparat og Double Uneven Power (DUP) konverteringsbaseret dc-dc apparat. Adskillelige simuleringsstudier og eksperimentelle resultater er præsenteret for at verificere gennemførlighed og operationelle principper af de foreslåede konverteringsapparater.

Slutteligt præsenteres brugen af et af de foreslåede konverteringsapparater i modellering og kontrol af jævnstrømsnetværk i en vindmøllepark. En gennemsnitlig model giver indsigt i systemets overordnede effektivitet mens en koblingsmodel fremfører detaljeret information om faktiske spidsværdier af strøm og spændingskrusninger i systemet. Kontrollen af vindmølleparkens jævnstrømsnetværk er baseret på de udviklede modeller og evalueret ved hjælp af adskillelige simuleringsstudier. De udviklede modeller og kontrolmetoder forventes at være brugbare til yderligere undersøgelser af driften af vindmølleparkers jævnstrømsnetværk under tilførsel af vindhastighed og/eller fejltilstande.

Abbreviations

AC/ac   Alternating Current

cc   Current Controller

CCM   Continuous Conduction Mode

CCMFB   Continuous Conduction Mode Full-Bridge

DBR   Dynamic Braking Resistor

DC/dc   Direct Current

DCG   Direct Current Generator

DCM   Discontinuous Conduction Mode

DCMFB   Discontinuous Conduction Mode Full-Bridge

DUP   Double Uneven Power

emf   Electromotive Force

FB   Full-Bridge

FEA   Finite Element Analysis

FLC   Fuzzy Logic Control

GA   Genetic Algorithm

HVDC   High-Voltage Direct Current

IG   Induction Generator

MCU   Micro Controller Unit

MPP   Maximum Power Point

MPPT	Maximum Power Point Tracking
NNC	Neural Network Control
PCSAB	Parallel-Connected Single Active Bridge
PD	Proportional Differential
PI	Proportional Integral
PID	Proportional Integral Differential
PMSG	Permanent Magnet Synchronous Generator
SAB	Single Active Bridge
sc	Speed Controller
SRG	Switched Reluctance Generator
SRM	Switched Reluctance Motor/Machine
SQP	Sequential Quadratic Programming
TSF	Torque Sharing Function
VSC	Voltage Source Converter
VSS	Variable Structure System
WECS	Wind Energy Conversion System
WT	Wind Turbine
ZCS	Zero-Current-Switching

Table of Contents

Chapter 1

Introduction

1.1 Background and Motivation

Wind energy offers a practically unlimited, clean, and emissions free power source of which only a tiny fraction is currently being exploited. During the last decade, the global markets of wind energy have grown by an average 28% per year in terms of total installed capacity [1]. Various wind turbine concepts have been developed and different wind generators have been built since 1970s. According to the survey of different wind generator systems and considering the grid connection requirements, the developing trends of wind generator systems can be summarized as the variable-speed concepts with a full-scale power electronic converter [2, 3].

A Switched Reluctance Generator (SRG) has various desirable features and its future is still bright with demanding applications. The absence of windings on the rotor makes an overall structure tolerant of extreme environments and keeps the majority of the losses within the stator, making the SRG relatively easy to cool down. In addition, the switched nature of the SRG makes it compatible with the modern wind energy applications which require variable-speed operation [4].

A review in the relevant literature of the control strategies shows that, although most research attention has been paid to Switched Reluctance Motor (SRM) control, the control of the SRG has not been treated extensively. Some research on control strategies for the SRG has been published though. *Torrey* has presented a discussion of the torque production and energy conversion process of the SRG in [4], which provides insight into the operation of the

SRG. Furthermore, the author proposed a novel control scheme which maximizes the efficiency of the SRG by optimally selecting both turn-on and turn-off angles. Similarly, *Kioskeridis* and *Mademlis* have proposed a controller that determines the optimal turn-on and turn-off angles only in the mode of single-pulse operation, but based on the optimal control of the flux-linkage [5]. In [6], *Chang* and *Liaw* have presented the design method of a dc-link filter and a voltage control scheme to reduce the dc-link voltage ripples in the SRG power circuit, improving the energy conversion efficiency. *Cardenas et al.* have presented a control system for the SRG as a part of a wind energy conversion system (WECS) in [7].

Although there are some important differences in control objectives and control implementation, the SRG can be considered the dual of the SRM [4]. Therefore, well established and developed control schemes for the SRM can also be employed for the control of the SRG with slight modifications. *Buja et al.* in [8] have applied a variable structure system (VSS) to reduce the torque ripple of the SRM and to compensate for the nonlinear torque characteristics. Similarly, *Kjaer et al.* have introduced a high-grade control of the SRM in [9]. "High-grade" means a performance that will enable the SRM to be a serious contender for many applications currently employing vector-controlled ac drives, blushless dc, or even dc commutator drives. In [10], *Sozer et al.* have developed a new algorithm for the automatic control of the turn-on angle of the SRM. This approach provides for automatic turn-on angle adjustment without the need for motor parameters or self-tuning technique.

Since the SRG inherently requires dc voltage source to operate properly, it is advantageous to connect SRG turbines with a dc network to collect and transmit the generated electrical energy. Power transmission by means of high voltage direct current (HVDC) became economically feasible with the development of the high-voltage mercury-arc valve. Since then, the advantage of HVDC power transmission and technological improvements in power system hardware and control methods have combined to make HVDC a major element of the world power market. *Andersen* and *Barker* in [11] have reviewed the advantages of the HVDC transmission, and discussed the benefits that the use of voltage-source converters (VSC) could bring. Similarly, *Flourentzou et al.* have provided an overview of the recent advances in the area of VSC-based HVDC technology in [12]. The authors have pointed out that wind farms and offshore wind farms in particular are well suited for VSC-HVDC application from the technology point of view.

Interconnecting generators using a dc network within wind farms is another issue worth an in-depth study for both onshore and offshore wind farms. The use of high-power dc-dc converters enables development of dc-collection grids. The benefits of dc grids are

critically dependent upon high-power dc-dc converters. However, there are no operational high-power dc-dc converters yet, but several different topologies are under research [13]. *Max et al.* in [14] have presented a detailed study on losses in different wind farm topologies and dc-dc converters such as full-bridge, single active bridge (SAB) and LCC resonance converters. In [15], *Meyer et al.* also have presented the comparisons among different 500 MW wind farm topologies. Furthermore, several papers on interconnecting generators using multitermial HVDC concepts and its control schemes have been published. *Jovcic* in [16] has presented a large offshore wind farm interconnected to the grid using a multiterminal HVDC link. In [17], *Lin* et al. have presented a control strategy of grid-connected converter in the multiterminal dc system consisting of several voltage source converters.

Although substantial work on the SRM and HVDC has already been done, there still are a lot of challenges in employing the SRG in wind energy applications and realizing a dc-grid wind farm. To name a few, more studies on the nonlinear characteristics of the SRG and development of proper nonlinear control strategies are required. High torque ripple problem of the SRG also needs to be solved to promote the application of the SRG. To realize a dc-grid wind farm, a practical high-power dc-dc converter and its control strategy should be developed first. Furthermore, to improve the reliability and efficiency of the overall system, more research on system protection, fault detection, and tolerant operation should be carried out. Therefore, it can be concluded that there are huge opportunities and strong demands in this research field.

1.2 Problem Statement and Project Aims

Despite the SRG has many attractive and advantageous features as a generator in harsh environments, it has not been widely employed in wind energy applications. The SRG inherently has a doubly salient structure and excessive magnetic saturation. Its flux linkage, inductance, and torque are highly coupled with the rotor position and phase current. All these features introduce high nonlinearity to the SRG. This nonlinear characteristic of the SRG makes it difficult to control the generator using traditional linear control methods. Therefore, it is important to introduce a more effective control strategy to promote the application of the SRG.

Another renowned disadvantage of the SRG is its high torque ripple. There are two major causes of the torque ripple: high nonlinear characteristics due to its excessive magnetic saturation and the discrete nature of torque producing mechanism due to its doubly salient structure. The nonlinearity causes the torque ripple when each phase is controlled with a

constant current reference. The SRG has very high torque ripples during the phase commutation period when the torque production is being transferred from the outgoing phase to the incoming phase. Therefore, it is also important to introduce an effective torque minimization technique to promote the application of the SRG.

Therefore, the first aim of this research is

to propose new control methods which can provide better control performance over a wide range of operating conditions and minimizes the torque ripple problem of the SRG.

High-power dc-dc converters are fundamental and essential components when interconnecting wind turbines using a dc network within a wind farm. Since the success of the dc grids is critically dependent upon the high-power dc-dc converters, active research is currently being undertaken to develop practical high-power dc-dc converters.

A lot of research on the dc-dc converters with a medium frequency transformer has been carried out extensively to improve the performance, efficiency, and reliability of the converters. However, there still exist several major obstacles which hamper the further growth of the power level of the converter, such as high power losses in the switching devices and large output filter inductance.

Therefore, the second aim of this research is

to propose not only new dc-dc converter topologies which are practical and reliable for high-power applications, but also their control strategies which have excellent dynamic performance suitable for dc-grid wind farm applications.

There exists no operating dc-grid wind farm yet. To verify the feasibility of a dc-grid wind farm and to investigate its characteristics in detail, an appropriate model of the overall dc-grid wind farm should be established first. The control of the dc-grid wind farm can be developed based on the obtained models and evaluated through various simulation studies. Furthermore, the developed models and control methods can be used for further studies on the operation of a dc-grid wind farm under various input and fault conditions.

Therefore, the final aim of this research is

to construct appropriate models of an entire dc-grid wind farm: an average model and a switch model, and to develop control of the dc-grid wind farm based on the obtained models.

1.3 Outline of the Thesis

The PhD dissertation contains five chapters and is organized as follows:

Chapter 1: Introduction

The background and the motivation for the research project are presented. Based on the problems, the objectives of the project are described as well. Finally, the outline of each chapter is given.

Chapter 2: Control of a Switched Reluctance Generator for Wind Energy Applications

A new self-tuning Fuzzy Logic Control (FLC) based speed controller of the SRG for the wind energy application is presented. The proposed control method has better adaptability which provides better performance over a wide range of operating conditions. Furthermore, a new non-unity Torque Sharing Function (TSF) for the SRG is presented. The proposed technique can minimize the torque ripples over a wider speed range of operation compared with the conventional TSFs.

Chapter 3: High-Power DC-DC Converters

Two high-power dc-dc converter topologies are proposed: a Parallel-Connected Single Active Bridge (PCSAB) dc-dc converter and a Double Uneven Power (DUP) converter based dc-dc converter. Both the steady-state and dynamic analyses of the PCSAB dc-dc converter are presented first. Based on the analyses, new design and control methods are proposed. In addition, a new open-circuit fault detection method and its tolerant control strategy are presented for the PCSAB dc-dc converter. Finally, a novel DUP converter based dc-dc converter and its design and control schemes are introduced. To verify the effectiveness of the proposed converter for the high-power applications, a comparative analysis especially for the dc-grid wind farm application is presented.

Chapter 4: Modelling and Control of a DC-Grid Wind Farm

This chapter presents modelling and control of a dc-grid wind farm with the PCSAB dc-dc converters introduced in the previous chapter. The dc-grid wind farm is modelled in two different ways depending on the requirements of the simulation: an average model and a switching model. The control of the dc-grid wind farm is developed based on the obtained models.

Chapter 5: Conclusions and Future Work

This chapter presents the summary and main findings and conclusions of this thesis. The topics for future work are also discussed in the end.

References

[1]   "Global Wind Energy Outlook 2010," Global Wind Energy Council, http://www.gwec.net, Oct. 2010.

[2]   Z. Chen and F. Blaabjerg, "Wind farm – a power source in future power systems," Renewable and Sustainable Energy Reviews, vol. 13, no. 6-7, pp. 1288-1300, Aug./Sept. 2009.

[3]   H. Li and Z. Chen, "Overview of different wind generator systems and their comparisons," IET Proc. Renew. Power Gener., vol. 2, no. 2, pp. 123-138, 2008.

[4]   D.A. Torrey, "Switched reluctance generators and their control," IEEE Trans. on Industrial Electronics, vol. 49, no. 1, pp. 3-14, Feb. 2002.

[5]   I. Kioskeridis and C. Mademlis, "Optimal efficiency control of switched reluctance generators," IEEE Trans. on Power Electronics, vol. 21, no. 4, pp. 1062-1072, July 2006.

[6]   Y. Chang and C. Liaw, "On the design of power circuit and control scheme for switched reluctance generator," IEEE Trans. on Power Electronics, vol. 23, no. 1, pp. 445-454, Jan. 2008.

[7]   R. Cardenas, T. Pena, M. Peres, J. Clare, G. Asher, and P. Wheeler, "Control of a switched reluctance generator for variable-speed wind energy applications," IEEE Trans. on Energy Conversion, vol. 20, no. 4, pp. 781-791, Dec. 2005.

[8]   G.S. Buja, R. Menis, and M.I. Valla, "Variable structure control of an srm drive," IEEE Trans. on industrial electronics, vol. 40, no. 1, pp. 56-63, Jan./Feb. 1993.

[9]   P.C. Kjaer, J.J. Gribble, and T.J.E. Miller, "High-grade control of switched reluctance machines," IEEE Trans. on Industry Applications, vol. 33, no. 6, pp. 1585-1593, Nov./Dec. 1997.

[10]   Y. Sozer, D.A. Torrey, and E. Mese, "Automatic control of excitation parameters for switched reluctance motor drives," IEEE Trans. on Power Electronics, vol. 18, no. 2, pp. 594-603, May 2006.

[11]   B. Andersen and C. Barker, "A new era in HVDC?," IEE Review, vol. 46, no. 2, pp. 33-39, Mar. 2000.

[12]   N. Flourentzou, V.G. Agelidis, and G.D. Demetriades, "VSC-Based HVDC power transmission systems: an overview," IEEE Trans. on Power Electronics, vol. 24, no. 3, pp. 592-602, Mar. 2009.

[13]   J. Robinson, D. Jovcic, and G. Joos, "Analysis and design of an offshore wind farm using a MV DC grid," IEEE Trans. on Power Delivery, vol. 25, no. 4, pp. 2164-2173, Oct. 2010.

[14]   L. Max and S. Lundberg, "System efficiency of a DC/DC converter-based wind farm," Wind Energy, vol. 11, pp. 109-120, Oct. 2008.

[15]   C. Meyer, M. Hoing, A. Peterson, and R. De Doncker, "Control and design of DC grids for offshore wind farms," IEEE Trans. on Ind. Appl. vol. 43, no. 6, pp. 1475-1482, Nov./Dec. 2007.

[16]   D. Jovcic, "Interconnecting offshore wind farms using multiterminal VSC-based HVDC" in Proc. IEEE Power Eng. Soc. General Meeting, pp. 1-7, Jun. 2006.

[17]   F. Lin, Z. Ma, X. You, and T. Zheng, "The grid connected converter control of multi-terminal DC system for wind farms" in Proc. of the 8th International Conference on Electrical Machines and Systems, vol. 2, pp. 1021-1023, Sept. 2005.

Chapter 2

Control of a Switched Reluctance Generator for Wind Energy Applications

2.1 Introduction

Although a Switched Reluctance Generator (SRG) has many advantages owing to its unique structural configuration, it is difficult to achieve satisfactory control performance because of its nature of nonlinearity and exquisite current commutation requirement. However, with the rapid technological development in power electronics and micro controller units (MCU) in recent years, the SRG is gaining increasing attention in various applications such as aerospace power systems, starter/alternators for hybrid vehicles, and wind energy conversion systems (WECS).

Due to the absence of windings and permanent magnets on the rotor, the SRG possesses various advantages as a generator, such as simple and robust construction, low inertia, fault tolerance, and ability to operate in high temperature and harsh environments. The stator of the SRG has simple and singly-excited windings so that the mutual influences among the stator phases are very low or even negligible, which enhances the fault tolerance ability of the SRG. Furthermore, since the majority of the losses are kept within the stator, which is relatively easy to cool down, the SRG can be realized to have high power density [1]-[4].

Despite all these advantageous features which make application of the SRG to WECSs attractive, the SRG has not been widely employed in wind energy applications. One of the difficulties is to achieve satisfactory control performance. The SRG inherently has a doubly salient structure and excessive magnetic saturation. Its flux linkage, inductance, and torque are highly coupled with a rotor position and a phase current. All these features

introduce high nonlinearity to the SRG. This nonlinear characteristic of the SRG makes it difficult to achieve satisfactory control performance by using traditional linear control methods such as proportional, integral and/or derivative (PI, PD, and PID) controllers [5]-[9]. Therefore, it is important to introduce a more effective control strategy to promote the application of the SRG.

The traditional linear controller could be tuned to obtain desired performance under a specific set of operating conditions. However, its performance significantly deteriorates as the operating conditions vary with the strong nonlinearity of the SRG [5]. For nonlinear systems, intellectual control techniques, such as Fuzzy Logic Control (FLC), Neural Network Control (NNC), and Genetic Algorithm (GA), allow better performance. The FLC is one of the most powerful control methods, which depends more on a logical model of the human behavior of a process operator than on an analytical model of a set of differential equations [6]. For this reason, the FLC has been widely studied for switched reluctance machines and various types of the FLC have been proposed in the literature. However, there are few publications on the application to generator systems [5], but mostly on the application to motor drive systems [6-9].

In the earlier part of this chapter, the theoretical background of the SRG will be given and a noble SRG speed controller based on self-tuning FLC will be presented for a wind energy application. The proposed controller utilizes the FLC with a self-tuning mechanism to improve the performance of controlling the speed of the SRG. The controller dynamically determines the turn-on and turn-off angles depending on the magnitude of phase currents and the rotational speed of the SRG. These features make the controller insensitive to modeling uncertainties and strong nonlinearities of the SRG, and improve the performance both in the steady-state and transient responses. The effectiveness and resulting improvement in performance of the proposed controller will be demonstrated by simulation results.

Another renowned disadvantage of the SRG is its high torque ripple, which should be overcome to promote the application of the SRG. There are two major causes of the torque ripple: First, the SRG has very high nonlinear characteristics due to the excessive magnetic saturation. This nonlinearity causes the torque ripple when each phase is controlled with a constant square current waveform. The second cause is the discrete nature of torque producing mechanism due to the doubly salient structure of the SRG. The SRG has very high torque ripples during the phase commutation period when the torque production is being transferred from the outgoing phase to the incoming phase [10]-[13].

9

Since switched reluctance machines have been dominantly used as motor drives, many studies on reducing torque ripples in a motoring mode have been carried out extensively. One of the most convenient and well-known control approaches is a Torque Sharing Function (TSF) method. In order to reduce the torque ripple, the TSF method regulates the torque production of the individual phases to distribute the reference torque among all the phases, while keeping the sum of all the individual torque references equal to the required torque. As far as the basic requirements as a TSF are satisfied, the TSF can have various different shapes. The TSFs can be classified depending on functions used to implement them. Some of the most commonly used TSFs are based on linear [10], sinusoidal [11], cubic, and exponential [12, 13] functions.

Although the aforementioned TSFs, which are mainly developed for the motoring operation, can be directly employed to the SRG, the performance can be significantly improved, if the dynamically varying inductance with respect to the angular position of the rotor is taken into account for the generating operation. Unlike the motoring mode, each phase of the SRG starts conducting current when the phase inductance is around its maximum value. This high inductance prevents a current from building up to a desired value rapidly. This phase current error, in turn, induces an additional torque ripple. In the literature, a new asymmetric TSF [14] which considers this problem has been introduced. However, the asymmetric TSF utilizes a piecewise linear function and is only suitable for low speed operation.

In the latter part of this chapter, a novel non-unity TSF will be introduced to minimize the torque ripple over a wide speed range of operation. Unlike the traditional TSFs, the sum of all the normalized phase torque references is not unity. This intentional ripple component in the torque reference behaves in such a way that it compensates the ripples in the actual output torque. In addition, a piecewise quadratic equation is used, instead of a piecewise linear one, to improve the performance further by reducing the rate-of-change of the current reference. To find optimal parameters for the non-unity TSF at different operating speeds, a sequential quadratic programming method [15] is used. The effectiveness and resulting improvement in the performance of the proposed torque minimization technique will be demonstrated by simulation results.

2.2 Theoretical Background of the SRG Electromechanics

Before introducing new speed controller and torque minimization technique, a brief analysis of the SRG's electromechanics will be given here first. Fig. 2.1(a) shows the cross-

sectional profile of a conventional four phase 8/6-pole SRG and Fig. 2.1(b) shows its equivalent circuit of one phase winding. In Fig. 2.1(a), only one phase winding is shown for the sake of simplicity. Both the stator and the rotor of the SRG are usually made of steel laminations. While each salient pole on the stator has a concentrated winding, the rotor does not have any winding or permanent magnet, but a chunk of laminated steel shaped like a gear. This structural feature makes the SRG simple, robust, and low-cost. The equivalent circuit of one phase wining can be simplified with one phase resistance, R_s, connected to one phase inductance, $L(\theta_r,i)$ in series. It is worth noting that the inductance is a function of the rotor position, θ_r, and the phase current, i.

(a)   (b)
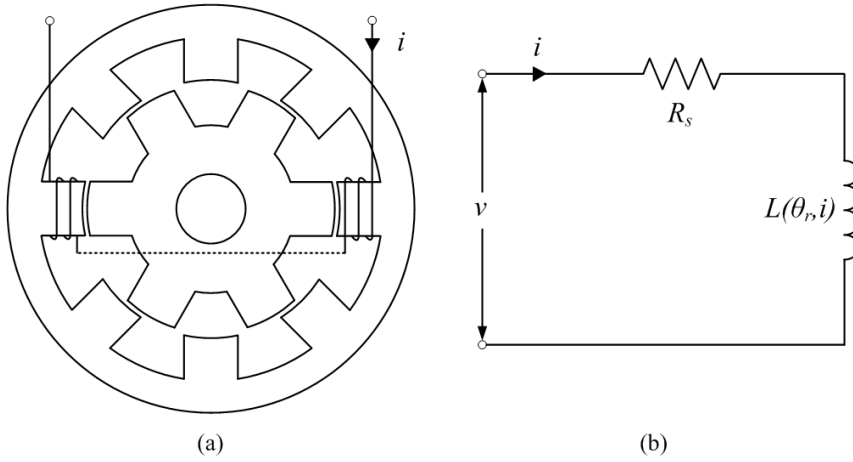
Fig. 2.1. Three-phase 8/6-pole SRG: (a) a cross-sectional profile and (b) an equivalent circuit of one phase winding.

From the equivalent circuit, the voltage equation of one phase winding can be derived as

$$v = R_s i + \frac{d\lambda(\theta_r,i)}{dt} , \tag{2.1}$$

where $\lambda(\theta_r,i)=L(\theta_r,i)\cdot i$ is the phase flux linkage. Using the relationship between the flux linkage and the inductance and current, this voltage equation can be rewritten as

$$v = R_s i + \frac{d[L(\theta_r,i)\cdot i]}{dt} = R_s i + L(\theta_r,i)\frac{di}{dt} + \frac{dL(\theta_r,i)}{d\theta_r}\omega_r i , \tag{2.2}$$

where ω_r is the angular speed of the rotor. In the above equation, the terms on the right-hand side represent the resistive voltage drop, the inductive voltage drop, and the back-electromotive force (back-emf), respectively. It is worth nothing that the voltage equation is

11

also a function of the rotor position and the phase current. Furthermore, it is a nonlinear equation where two state variables (here, the angular speed, ω_r and the phase current, i) are multiplied together.

The electromagnetic torque equation of the SRG can be derived from the magnetization characteristics of one phase winding, which can be achieved through an experimental test or a Finite Element Analysis (FEA). Fig. 2.2 shows the magnetization characteristics of a 7.5 kW SRG. The uppermost line represents the flux linkage when the stator and the rotor are aligned. This line exhibits the high magnetic saturation characteristic of the flux. On the other hand, the lowermost line represents the flux linkage when the stator and the rotor are unaligned completely. This line does not exhibit the saturation characteristic because of a large air gap between the stator and rotor poles.
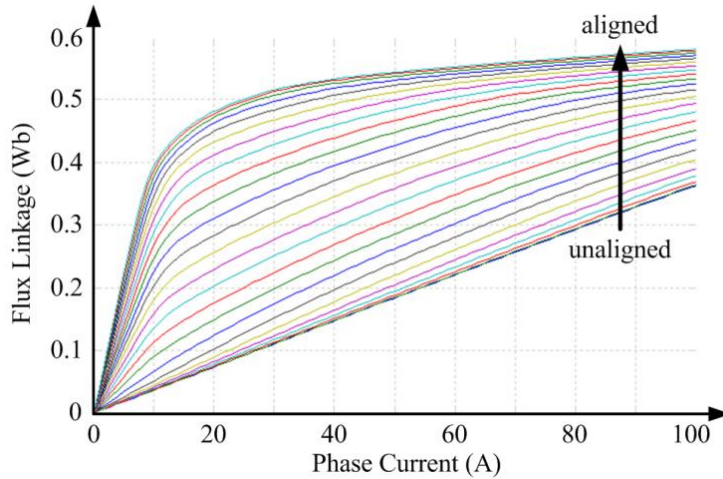

Fig. 2.2. Magnetization characteristics of a 7.5 kW 8/6-pole SRG.

The electromagnetic torque can be calculated by finding the partial derivative of the magnetic co-energy with respect to the angular position of the rotor [16]. The torque equation of the SRG can be expressed as

$$T_e(\theta_r, i) = \frac{1}{2} i^2 \frac{dL(\theta_r, i)}{d\theta_r} \quad . \tag{2.3}$$

This torque is dependent upon the rotor position and the phase current in a nonlinear way because the state variables are multiplied together (here, the phase current, i, is squared). Furthermore, the torque is proportional to the square of the phase current and to the partial derivative of the inductance with respect to the angular position of the rotor.

If the mechanical and stray loses are neglected, the mechanical equation of the SRG is given as

$$T_m - T_e(\theta_r, i) = J\frac{d\omega_r}{dt} + B\omega_r,$$ (2.4)

where J is the moment of inertia, B is the viscous coefficient of friction, and T_m is the mechanical torque which is the accelerating torque of a wind turbine.

Substituting (2.3) into (2.4) yields the overall mechanical equation of the SRG as follows.

$$T_m - \frac{1}{2}i^2\frac{dL(\theta_r, i)}{d\theta_r} = J\frac{d\omega_r}{dt} + B\omega_r$$ (2.5)

Fig. 2.3 shows the torque relationship between an idealized inductance profile and a phase current. The idealized inductance profile can be obtained by neglecting the effect of the magnetic saturation. It varies linearly with respect to the overlap between the stator and rotor poles. As it can be seen from the figure, the inductance has its maximum value, L_a, when the poles of the stator and rotor are fully aligned, whereas it has its minimum value, L_u, when the poles are completely unaligned. If a constant current is drawn in the phase only during the negative slope of the inductance profile, the negative torque can be generated. Therefore, if each phase produces torque in sequence at the right moments, the SRG can produce continuous unidirectional torque.
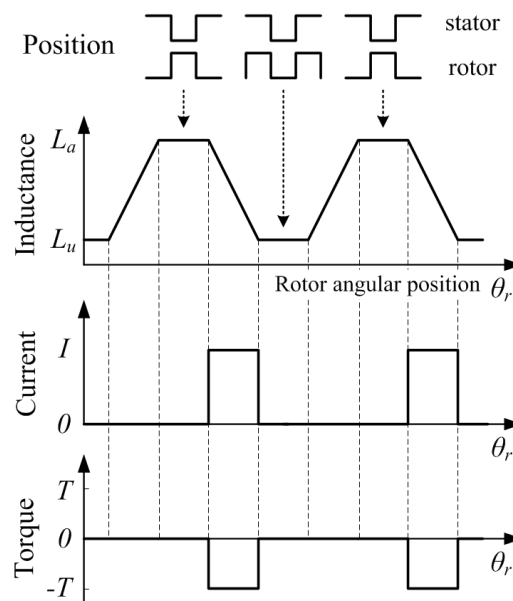

Fig. 2.3. Torque relationship between the idealized inductance profile and the phase current.

13

2.3 Self-Tuning Fuzzy Logic Control based Speed Controller

On the basis of the electromechanics of the SRG, a new speed controller based on the self-tuning Fuzzy Logic Control (FLC) for wind energy applications is presented in this subchapter. Fig. 2.4 shows the overall architecture of the proposed control system.
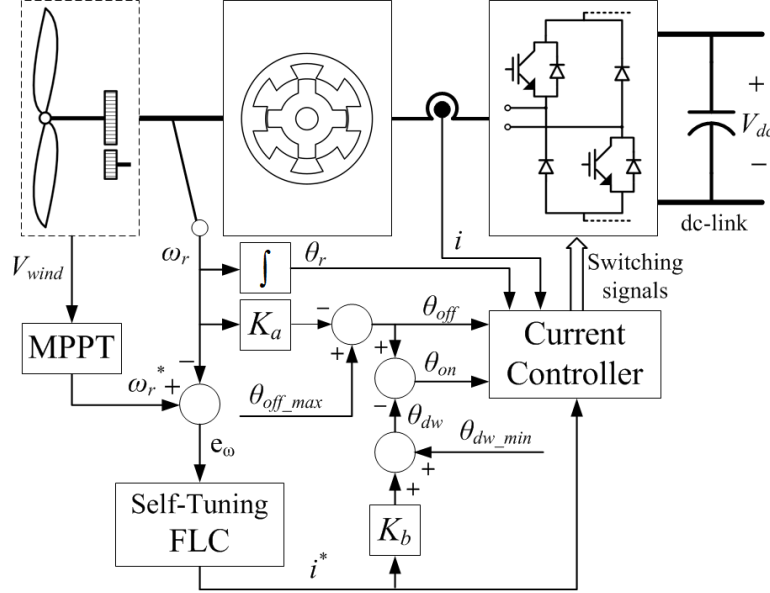

Fig. 2.4. Overall architecture of a proposed control system.

2.3.1 Turn-on Angle (θ_{on}) and Turn-off Angle (θ_{off}) Determination

Referring to (2.3) and Fig. 2.3, unidirectional torque (either positive or negative) is produced if the phase currents flow only when the polarities of the inductance slopes are the same (either positive or negative). In other words, in order to produce negative torque, the phase current needs to be controlled to build up to a desired value and fall back to zero again while the inductance slope is negative. The phase current, however, may not have enough time to fall back to zero before the next rise of the inductance as the rotational speed of the SRG increases. This situation becomes worse especially when a large current has been flowing in the phase winding. Consequently, this remaining current could produce positive torque and, in turn, deteriorate the efficiency and torque regulation of the SRG. Therefore, the turn-off angle (θ_{off}) should be controlled to avoid this undesirable phenomenon. In the proposed control scheme, the turn-off angle is advanced from the pre-set maximum turn-off angle (θ_{off_max}) in proportion to the rotational speed of the SRG with a scaling factor of K_a.

$$\theta_{off} = \theta_{off\_max} - K_a \omega_r \tag{2.6}$$

14

The turn-on angle (θ_{on}) should also be controlled depending on the magnitude of the reference current and the rotational speed of the SRG. It needs to be advanced when the magnitude of the reference current is large and/or the rotational speed is high so that the phase current can grow from zero to a desired value in time. In the proposed control method, an additional dwell angle ($\theta_{dw}= \theta_{off} - \theta_{on}$) is added to the pre-set minimum dwell angle (θ_{dw_min}) in proportion to the magnitude of the reference current (i^*) with a scaling factor of K_b. Finally, the turn-on angle is obtained by subtracting the dwell angle from the turn-off angle. In this way, the effect of the rotational speed variation can also be taken into account in determining the turn-on angle.

$$\theta_{on} = \theta_{off} - (\theta_{dw\_min} + K_b i^*) \tag{2.7}$$

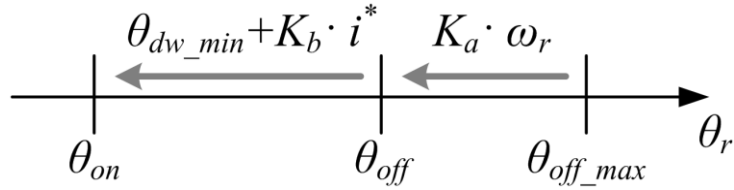Therefore, the turn-on angle and turn-off angle determination method can be summarized as shown in Fig. 2.5.

Fig. 2.5. Turn-on angle and turn-off angle determination method.

2.3.2 Self-Tuning Fuzzy Logic Control

Since the introduction of fuzzy logic by Zadeh in 1970s, The FLC has been widely studied and used to control complex, ill-defined, and/or nonlinear systems. The FLC is an artificial decision maker which depends more on the human behavior of the decision making process using linguistic rules, rather than on the analytic models of mathematical equations. Hence, the FLC does not require an accurate model of the plant and can be designed on the basis of the linguistic information. Furthermore, the FLC usually demonstrates better performance than the conventional linear controllers in terms of response time, settling time, and robustness [6].

Fig. 2.6 shows the block diagram of the self-tuning FLC used in this chapter. The 'self-tuning' means that additional control rules for the gain updating factor, α, are supplemented to the ordinary FLC. By multiplying the gain updating factor to the output gain, G_u, the self-tuning FLC can achieve more adaptability. In other words, it ensures better

control performance over a wide range of load variation regardless of inaccurate operating knowledge of the plant [7].
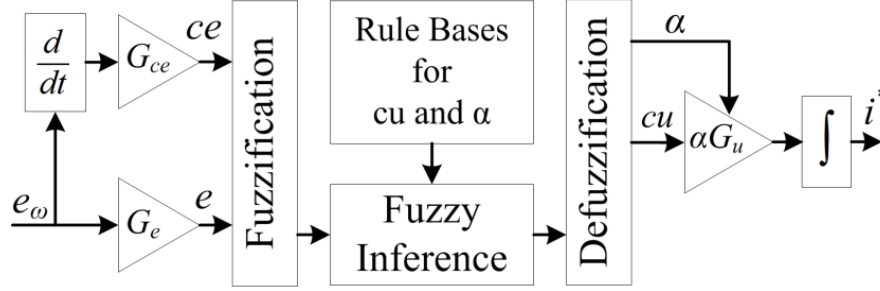

Fig. 2.6. Block diagram of the self-tuning FLC.

The self-tuning FLC uses the error (e_ω) of the rotational speed as an input. The change of error is obtained by differentiating the error. Both the error and the change of error are normalized by multiplying with the corresponding scaling factors G_e and G_{ce}. With these normalized input values, the fuzzification process is performed using the triangular membership functions which are symmetrical on both positive and negative sides as shown in Fig. 2.7(a). The linguistic values NB, NS, Z, PS, and PB stand for Negative Big, Negative Small, Zero, Positive Small, and Positive Big, respectively.

The evaluation of the control rules is performed with the rules shown in Table 2.1 and 2.2 for the incremental change of the output signal (cu) and the gain updating factor (α), respectively. The top row and the leftmost column describe the linguistic fuzzy sets for the input variables. Since there are 5 fuzzy sets for each input variable, there are 25 rules in total for each output.

The defuzzification is carried out using singleton membership functions as shown in Fig. 2.7(b) and (c) for each output. This method is often called the zero-order Sugeno method of implication. The additional linguistic values NM, PM, S, M, and B stand for Negative Medium, Positive Medium, Small, Medium, and Big, respectively. It is worth noting that the universe of discourse of cu is from -1 to 1. On the other hand, the universe of discourse of α is from 0 to 1. The output scaling factor (G_u) is online tuned by α depending on the input conditions. Finally, the output control signal, which is the reference phase current (i^*), can be obtained by integrating cu after multiplying with the tuned scaling factor (αG_u).
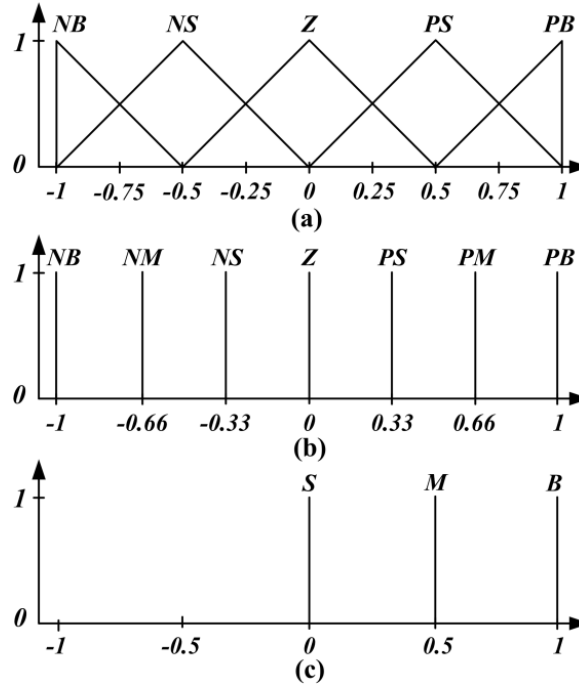
Fig. 2.7. Membership functions for (a) fuzzification, (b) defuzzification for *cu*, and (c) defuzzification for *α*.

Table 2.1. Rule Table for the Incremental Change of Output Signal (*ce*)

ce \ e	NB	NS	Z	PS	PB
NB	NB	NB	NM	NS	Z
NS	NB	NM	NS	Z	PS
Z	NM	NS	Z	PS	PM
PS	NS	Z	PS	PM	PB
PB	Z	PS	PM	PB	PB

Table 2.2. Rule Table for the Gain Updating Factor (*α*)

ce \ e	NB	NS	Z	PS	PB
NB	B	B	M	S	S
NS	B	B	M	S	S
Z	M	M	S	M	M
PS	S	S	M	B	B
PB	S	S	M	B	B

2.3.3 Current Controller

When the SRG operates at a low speed and/or at a light load, the current needs to be controlled at a desired value. Fig. 2.8 shows the block diagram of the proposed current controller which basically utilizes general hysteresis control. If the error (e_i) of the phase current is smaller than the negative pre-set hysteresis value ($-\Delta h$), the power semiconductor switches are turned on to supply the dc voltage (V_{dc}) to the phase winding. This increases the

phase current. On the other hand, if e_i is bigger than Δh, then the switches are turned off and the phase current finds its path through the diodes, which, consequently, supplies negative dc voltage ($-V_{dc}$) to the phase winding and decreases the phase current. This hysteresis output signal is combined with the turn-on and turn-off angle information through a logical 'AND' to produce a final output switching signal. In addition, the current limit is also included for the purpose of protecting the power semiconductor switches from unexpected high current events.
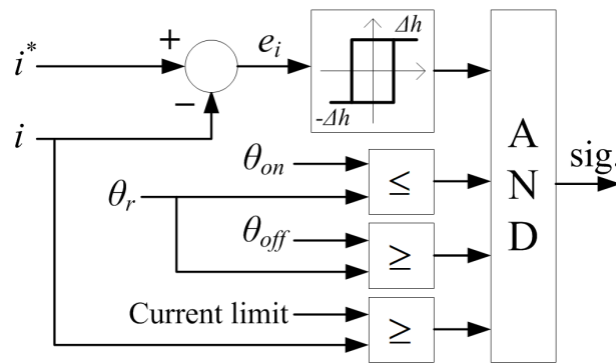

Fig. 2.8. Block diagram of the current controller.

2.3.4 Simulations

Simulations have been performed to verify the effectiveness and resulting improvement of the proposed controller using Matlab/Simulink. The parameters for the simulation are summarized in Table 2.3 [17].

Table 2.3. Parameters for the Simulation

	Parameter	Quantity
SRG	Type (stator/rotor poles)	6/4
	Rated Power	1.5 MW
	Rated Voltage	2.3 kV
	Rated Current	652 A
	Winding Resistance (R_s)	0.01 Ω
	Aligned Inductance (L_a)	23.6 mH
	Saturated Inductance (L_{a_sat})	0.15 mH
	Unaligned Inductance (L_u)	0.67 mH
Wind Turbine	Rated Mechanical Output	1.5 MW
	Base Wind Speed (V_{base})	12 m/s
	Pitch Angle (β)	0°
Mechanical	Inertia (J)	1 kgm²
	Friction (B)	0.01 Nms
DC Link	Supply Voltage (V_{dc})	2.3 kV

18

To compare the performance of the proposed controller with that of the conventional PI controller, the gains of the PI controller are tuned to have the same performance without any external acceleration torque from the wind turbine ($T_{acc}=0$). Fig. 2.9 shows the step responses of the tuned PI controller and the proposed controller, respectively. The reference speed is set to 750 rpm at 0 *s* and changed into 1500 rpm at 0.2 *s* in a step manner. As it can be seen from the figure, both of the controllers demonstrate practically the same dynamic and steady-state responses under the no external acceleration torque condition.

Fig. 2.10 shows the speed and torque waveforms of the PI controller when the acceleration torque is changed from 0 to 1000 *Nm* at 0.2 *s* in a step manner. The reference speed is kept constant at 1500 *rpm*. As it can be seen from the waveform of the controlled speed, the PI controller cannot track the reference speed when the acceleration torque is applied. The fundamental cause of this problem is that the integral gain (I) of the PI controller was tuned too small to eliminate or reduce the steady-state error for this particular operating point. If the gains of the PI controller are retuned to have better performance at one particular operating point, the performance at the other operating points will deteriorate. This means that variable speed operation has some difficulties with a conventional PI controller. Hence, an adaptive online gain tuning mechanism which takes the nonlinearity of the SRG into account is required for this reason.
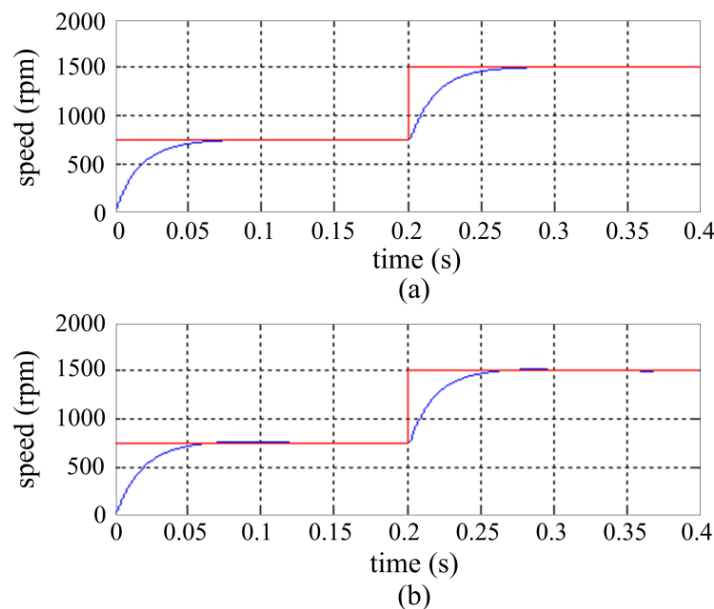

Fig. 2.9. Step responses of (a) the PI controller and (b) the proposed controller under no external acceleration torque condition.
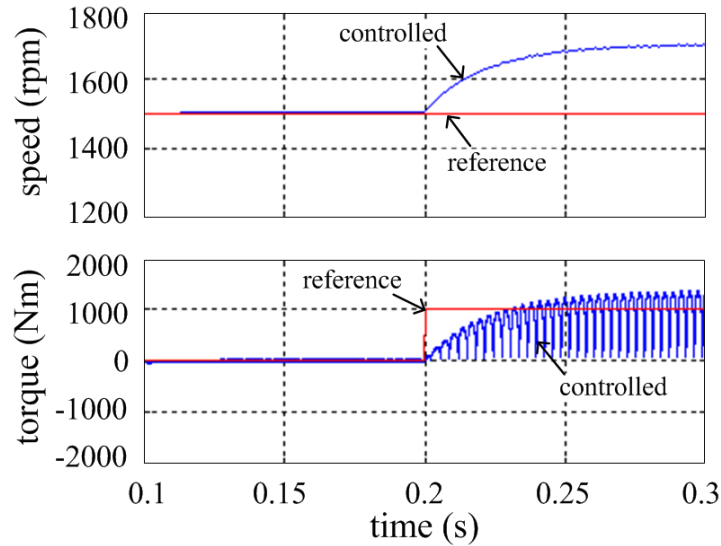
Fig. 2.10. Resulting waveforms of the conventional PI controller when 1000 *Nm* is applied at 0.2 *s*.

On the other hand, the self-tuning FLC inherently has the adaptability which ensures better control performance over a wide range of operating points. Fig. 2.11 shows the resulting waveforms of the proposed controller under the same simulation condition with that of the PI controller. As it can be seen from the figure, the controlled speed of the SRG tracks the reference speed very well when the acceleration torque is applied. In order to keep tracking the reference speed, the proposed controller produces more electromagnetic torque than the PI controller does. It is worth noting that the generated electromagnetic torque of the SRG has high ripple components. This is one of the major disadvantages of the SRG and should be overcome to accelerate market penetration of SRG in the future. This high torque ripple problem will be discussed in the next subchapter.
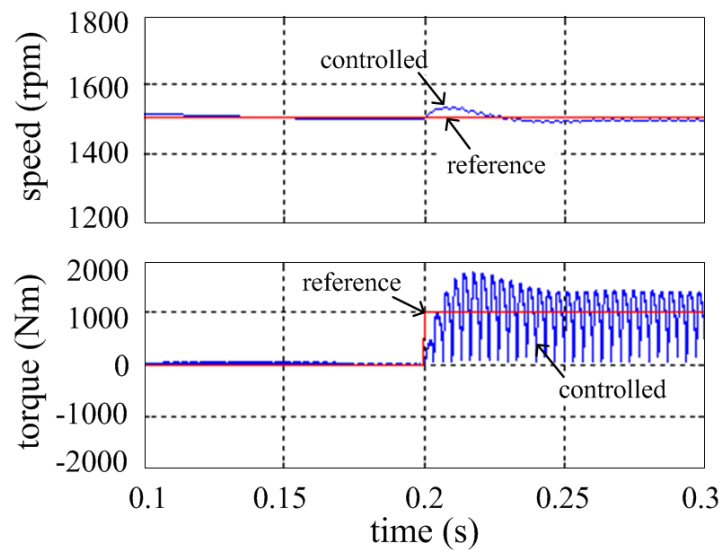

Fig. 2.11. Resulting waveforms of the proposed controller when 1000 *Nm* is applied at 0.2 *s*.

20

Finally, Fig. 2.12 and 2.13 show the simulation results in combination with the wind turbine specified in Table 2.3. The wind speed is varied from 0 to 12 *m/s* in a ramp manner and kept constant after it reaches its base speed (12 *m/s*). The SRG is controlled to extract the maximum power from the wind turbine. As it can be seen from Fig. 2.12, although the SRG tracks the reference speed fairly well at very low wind speeds, the steady-state error becomes bigger as the wind speed increases. Since the rotational speed of the SRG cannot be controlled to track the reference speeds of the Maximum Power Points (MPPs), the wind turbine cannot produce the maximum power either.
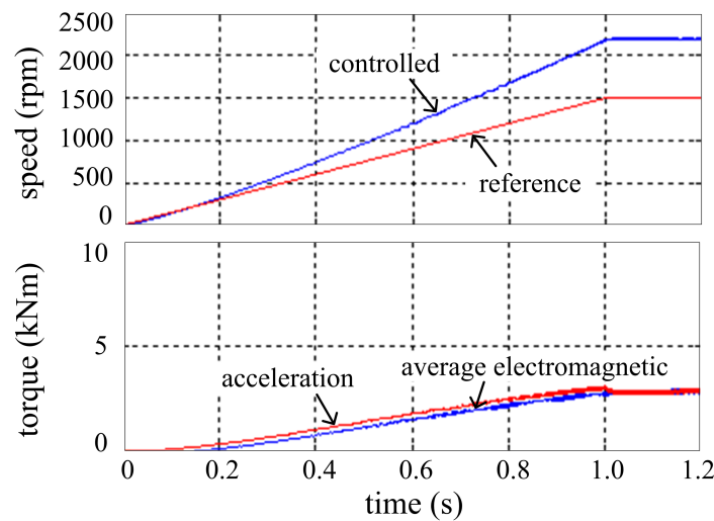
Fig. 2.12. Resulting waveforms of the PI controller in combination with the wind turbine.

On the other hand, the SRG controlled by the proposed control method tracks the reference speed very well over the whole operating range of the wind speed as shown in Fig. 2.13. Since the SRG, now, follows the MMPs very well, the wind turbine produces much larger acceleration torque. The calculated output power of the SRG at the base wind speed is 2.31 times as big when the proposed controller is used. This simulation result verifies that the proposed controller has more adaptability and better performance over a wide range of operating conditions than the conventional PI controller.
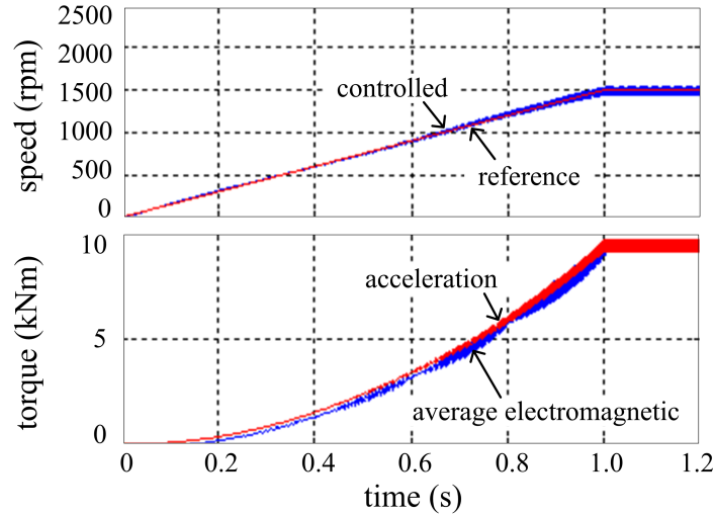
21

Fig. 2.13. Resulting waveforms of the proposed controller in combination with the wind turbine.

2.4 Non-Unity Torque Sharing Function for Torque Ripple Minimization

2.4.1 Main Causes of Torque Ripples

There are several main causes of the torque ripples in the SRG: high nonlinearity, phase commutation, and current switching. If the effect of the magnetic saturation is not neglected, the inductance profile does not vary linearly with respect to the overlap between the stator and rotor poles anymore. Hence, even if the each phase is controlled to draw a constant current, the produced torque is not constant anymore. This nonlinearity usually causes a torque swell when a single phase is solely in charge of producing the entire toque required. Therefore, the phase current should be shaped depending on the nonlinear torque-angle-current (T-θ-i) characteristics of the SRG to produce constant torque.

Another main cause of the torque ripple is the discrete nature of torque producing mechanism due to the doubly salient structure of the SRG. Unlike traditional three-phase generators such as an Induction Generator (IG) or a Permanent Magnet Synchronous Generator (PMSG), the SRG does not utilize a smooth rotating magnetic field. Each phase of the SRG is responsible for producing torque independently using magnetic reluctance force. Therefore, the SRG has a very high torque ripple, usually a torque dip, during the phase commutation period when the torque production is being transferred from the outgoing phase to the incoming phase.

The other cause of the torque ripple is the current switching. The current in each phase should be controlled to track its desired value by switching the power semiconductor

22

switches connected to the phase. As a consequence, these switching current ripples cause additional torque ripples at a switching frequency. The magnitude of the torque ripple depends on the switching frequency and the operating conditions such as an input voltage, a load torque, and/or an operating speed. If the phase current is controlled by a hysteresis current controller as in this thesis, the magnitude of the torque ripple is also significantly dependent upon the size of its hysteresis band.

2.4.2 Traditional Torque Sharing Functions

The Torque Sharing Function (TSF) controls the instantaneous torque of the individual phases by profiling the phase currents optimally during a phase overlapping period between the outgoing and incoming phases. Fig. 2.14 shows the overall torque control scheme of the TSF method. The normalized TSF block produces torque references for the individual phases based on the angular position of the rotor. These normalized torque references are multiplied with the total torque required (T^*) so that the actual torque reference for each phase is obtained separately. Each torque reference is, then, converted into a current reference through the 2-D lookup table of the torque-angle-current (T-θ-i) characteristics which can be directly obtained from the magnetization characteristics of the SRG. To avoid storing large lookup table data, an invertible torque function [18] can be used instead. Finally, the current controller produces switching signals for the power converter based on the reference currents and the measured currents.
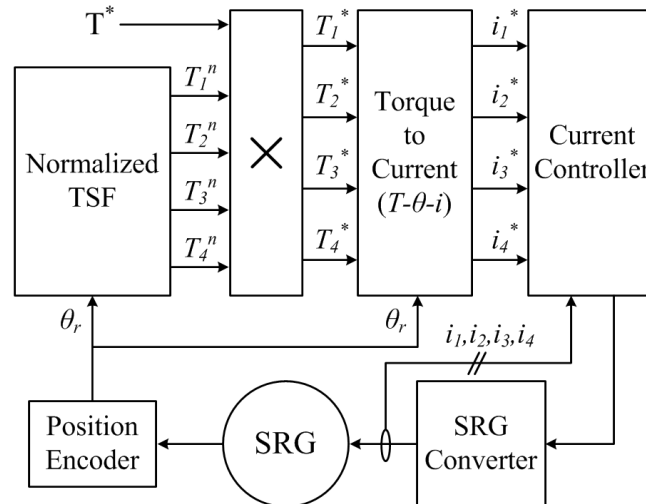
Fig. 2.14. Overall torque control scheme of the TSF method.

Depending on torque sharing curves used for the phase overlapping period, the traditional TSFs can be classified as linear or nonlinear TSFs as shown in Fig. 2.15(a) and (b).

The nonlinear TSFs further can be classified into sinusoidal, cubic, and exponential TSFs. By optimizing the turn-on angle, θ_{on}, and the overlapping angle, θ_{ov}, the traditional TSFs minimize their torque ripples.

Fig. 2.15. Typical profiles of the (a) linear, (b) nonlinear, and (c) asymmetric TSFs.

Although these TSFs have been dominantly developed for the motoring operation, they could be directly employed for the generating operation. However, if the unique characteristic of the SRG is taken into account, the performance of the TSF technique can be enhanced further. Unlike the motoring mode, each phase of the SRG starts being energized

24

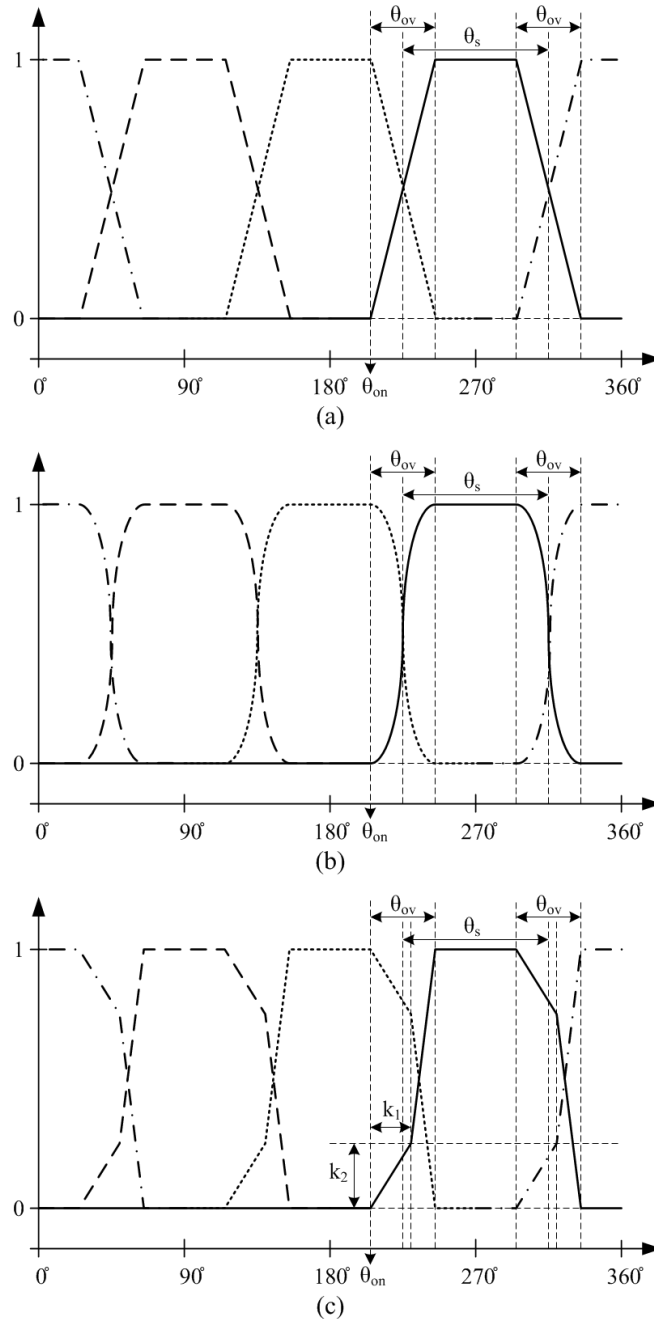when the stator and the rotor are aligned, and deenergized when they are unaligned. In other words, the phase inductance is at its maximum value when the phase starts conducting a current. This high inductance prevents a current from tracking a reference value accurately, especially when the rate-of-change of the reference current is large. This phase current error, in turn, induces additional torque ripples.

In order to solve this problem, the asymmetric TSF which utilizes a piecewise linear curve to lower the rate-of-change of the current reference has been proposed [14] as shown in Fig. 2.15(c). By introducing two more control parameters (k_1 and k_2), the asymmetric TSF utilizes two different slopes during the phase overlapping period. It is worth noting that the stroke angle, θ_s, is determined depending on the number of the phases, N_{ph}, and the number of the rotor poles, N_r, as below.

$$\theta_s = \frac{360°}{N_{ph} \cdot N_r} \tag{2.8}$$

Although the TSFs in Fig. 2.15 have different shapes, they all satisfy a basic requirement as a TSF: the sum of all the normalized phase torque references is always equal to unity. Furthermore, they all assume that the actual current is well controlled to track its reference value. Therefore, the TSF technique is not applicable to the single-pulse voltage mode. The SRG normally enters the single-pulse voltage mode of operation at very high speeds where the shape of a phase current cannot be controlled and the control can be achieved only by advancing the turn-on angle and adjusting the conduction angle.

2.4.3 Proposed Non-unity Torque Sharing Function

Although the asymmetric TSF for the SRG has satisfactory performance at low speeds, its performance deteriorates as an operating speed increases. In this subchapter, the torque ripples at high speeds will be analyzed and a novel non-unity TSF will be introduced to minimize the torque ripple over a wide speed range of operation.

2.4.3.1 Causes of Torque Ripples at High Speeds

Fig. 2.16 shows the waveforms of the produced torque and the phase current and its reference value at the high speed of 1000 rpm when the asymmetric TSF is used. At the beginning of the current conduction in each phase, the rate-of-change of the current reference is still much higher than that of the actual current due to the high phase inductance. During this period, this lack of actual current induces a dip in the output torque (region 'A'). On the

other hand, at the end of the current conduction, the actual current cannot decrease to zero as fast as the reference value at high speeds even though the phase inductance is much lower. This excessive current, in turn, induces a torque swell as shown in the figure (region 'B'). These two torque ripple components prevent the TSF techniques from having a wide speed range of operation.
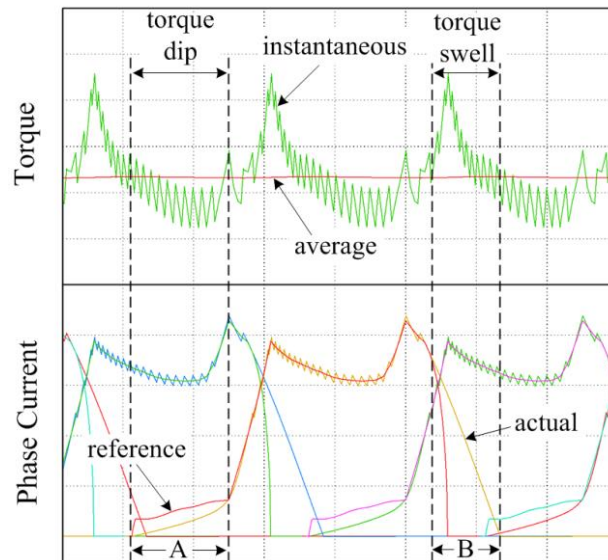

Fig. 2.16. Waveforms of the produced torque and the phase current at the high speed of 1000 rpm.

2.4.3.2 Non-unity Piecewise Quadratic TSF

In order to improve the performance and to extend the operating speed range of the asymmetric TSF, a new non-unity piecewise quadratic TSF is proposed here. Among the traditional symmetric TSFs (linear, sinusoidal, cubic, and exponential), the nonlinear TSFs usually have better performance than the linear TSF because the nonlinear TSFs tend to have lower rate-of-change of the reference current. This idea is also applicable to the asymmetric TSF. Therefore, as shown in Fig. 2.17(a), a piecewise quadratic curve is applied to the proposed TSF to lower the rate-of-change of the reference current especially for the beginning of the current conduction.

In the proposed TSF, two additional control parameters (k_3 and k_4) are introduced as shown in Fig. 2.17(b). k_3 makes the angle, where the TSF curve reaches unity, retreat and induces a dip in the sum of all the individual torque references. On the other hand, k_4 slows the decrease of the reference torque so that it causes a swell in the sum. Hence, the sum of all the individual torque references is not unity anymore as shown in Fig. 2.18. These deliberately inserted ripple components in the torque reference behave in such way that it

26

compensates the actual ripples in the output torque during the high speed operation. Therefore, by optimizing six control parameters (θ_{on}, θ_{ov}, k_1, k_2, k_3, and k_4) at each operating speed, the torque ripple can be minimized significantly over a wider speed range of operation. The optimization can be performed using various optimization algorithms such as a least square method or a Genetic Algorithm (GA). In this thesis, a Sequential Quadratic Programming (SQP) method [15], which is already implemented and can be easily accessed through the function named 'fmincon' in Matlab, is used.
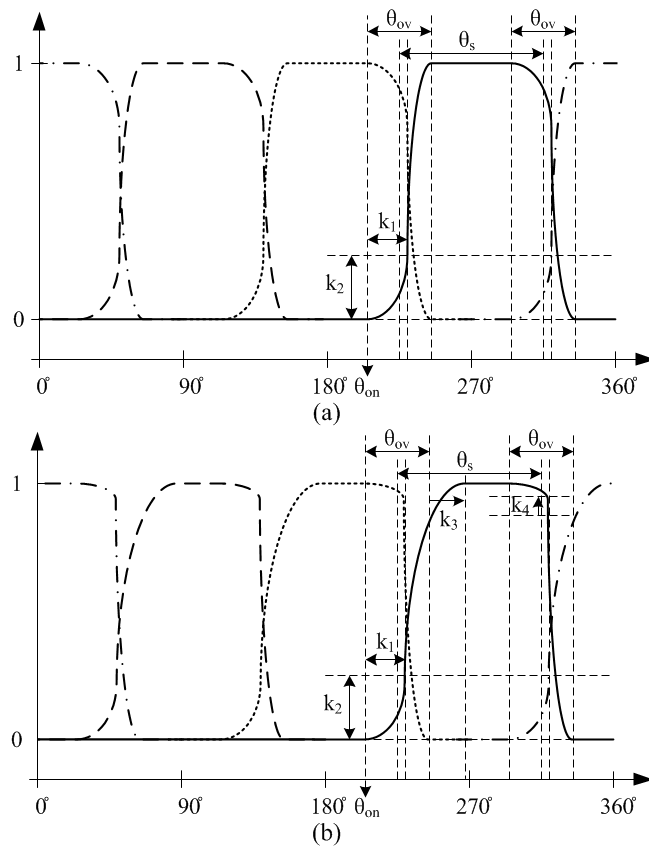

Fig. 2.17. Profiles of (a) the asymmetric TSF with a piecewise quadratic curve and (b) the proposed non-unity TSF.
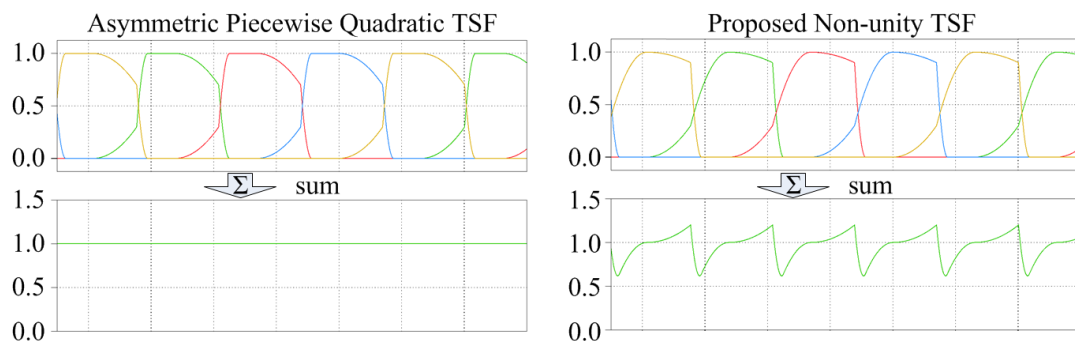

Fig. 2.18. Torque references for the individual phases and the total sum of them.

27

2.4.4 Simulations

Simulations have been performed to verify the effectiveness of the proposed TSF technique using Matlab/Simulink. To compare the performance of the proposed TSF with that of the conventional asymmetric TSF, simulations for both the asymmetric and non-unity TSFs have been performed in parallel at various operating speeds. The SRG model used in this simulation is a 7.5 kW, 4-phase, 8/6-pole generator whose magnetization characteristics are shown in Fig. 2.2. Hysteresis control is used for the current controller and the hysteresis band is set to 2 A for all the operating speeds. The SRG is controlled by a conventional asymmetric half-bridge converter using 280 V_{dc}. Figs. 2.18 to 2.10 show the resulting waveforms of the simulations at various operating speeds. Table 2.4 and 2.5 summarize the simulation results with respect to the torque and phase current characteristics, respectively.

As it can be seen from Fig. 2.19, the torque ripples at 333 rpm are dominantly caused by the current switching for both the TSFs. The magnitude of the torque ripples during the commutation period is kept within that of the torque ripples caused by the switching. Both the asymmetric and non-unity TSFs have almost identical performance at the low speed of 333 rpm. Using the proposed TSF, only 0.13% of the toque ripple is reduced compared with that of the asymmetric TSF at this speed. Furthermore, it is also observed that the maximum peak current and the RMS current are reduced by 4.24% and 2.5%, respectively. Therefore, it can be concluded that the conventional asymmetric TSF has satisfactory performance at low speeds compared with the proposed TSF.
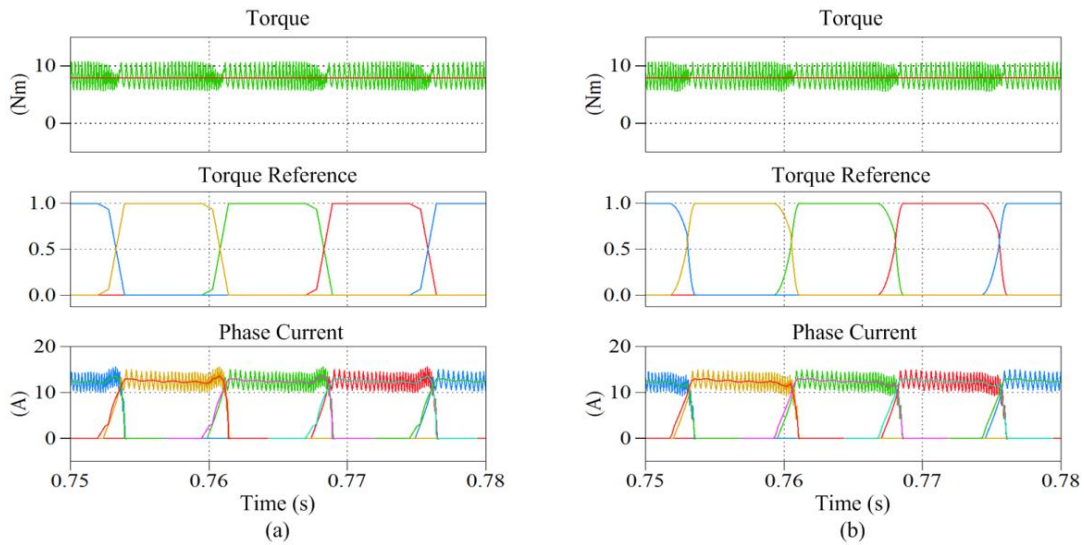

Fig. 2.19. Simulation results of (a) the asymmetric TSF and (b) the proposed non-unity TSF operating at 333 rpm.

Fig. 2.20 shows the simulation results when the SRG is operating at 666 rpm. As the speed increases, the torque ripples during the phase commutation become more observable. Since the asymmetric TSF does not have the ability to compensate the torque ripples caused by errors in the phase currents at beginning and end of the conduction, the torque dips and swells arise. The switching frequency torque ripples are still superimposed on these torque dips and swells. On the other hand, the proposed TSF tries to keep the output torque ripples as small as possible using its compensating ability. Using the non-unity TSF, 10.35% of the toque ripple is reduced at this speed. However, 15.31% of the maximum peak current and 1.66% of the RMS current are increased.
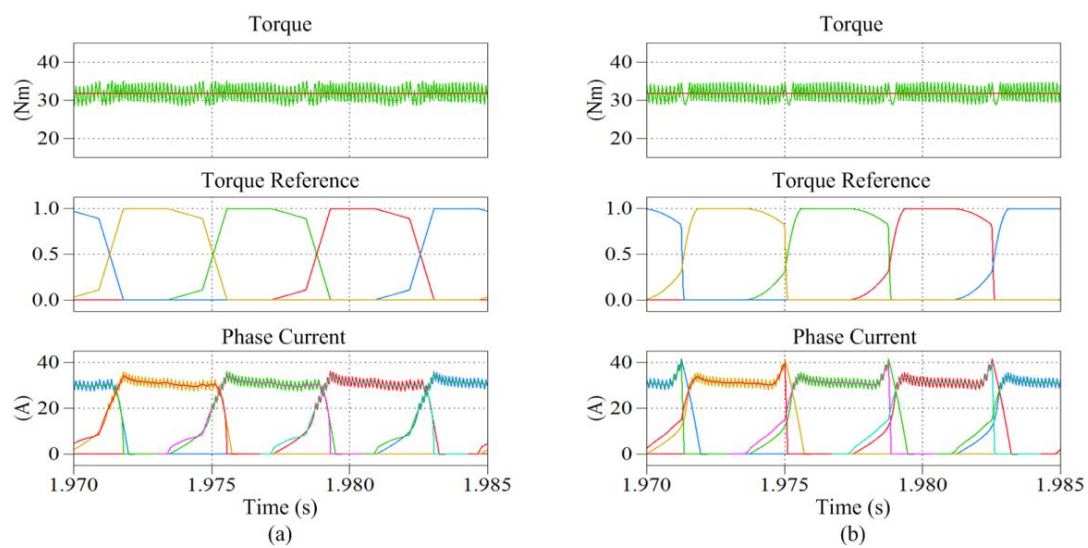
Fig. 2.20. Simulation results of (a) the asymmetric TSF and (b) the proposed non-unity TSF operating at 666 rpm.

If the operating speed of the SRG is increased even further, the effectiveness of the proposed TSF becomes more evident. Fig. 2.21 shows the simulation results when the SRG is operating at 1000 rpm. Now, it can be observed that the magnitudes of these torque dips and swells are much bigger than that of torque ripples caused by the current switching. The asymmetric TSF has the total torque ripple of 22.92%, whereas the proposed non-unity TSF has 8.12%. Therefore, the torque ripple is reduced by 64.57% at this speed. Using the non-unity TSF, the magnitude of the torque ripples is kept almost within that of the torque ripple caused by the current switching. However, the price paid for this torque ripple reduction is the increases of the maximum peak current and the RMS current by 21.76% and 9.35%, respectively.
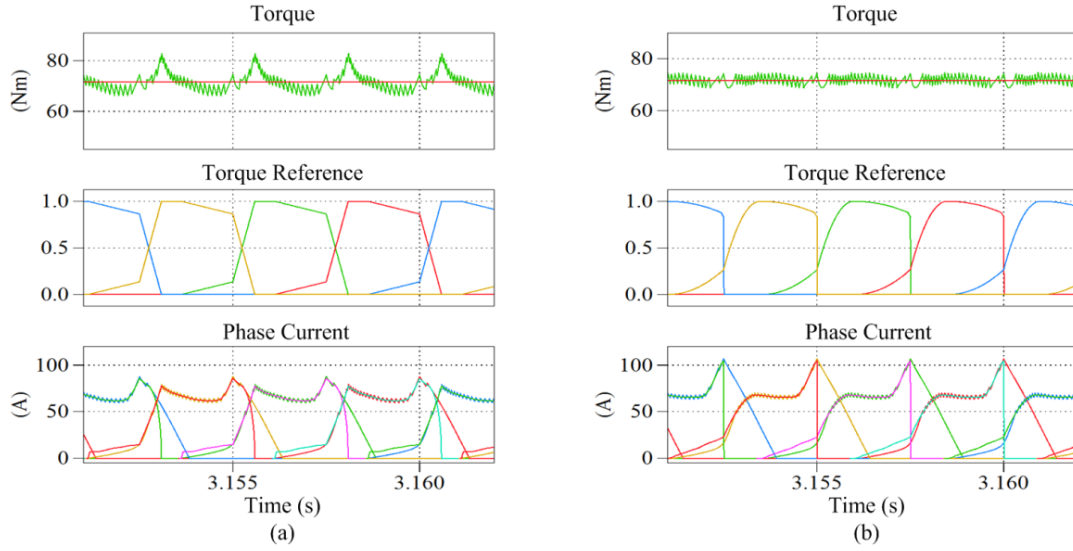
29

Fig. 2.21. Simulation results of (a) the asymmetric TSF and (b) the proposed non-unity TSF operating at 1000 rpm.

Table 2.4. Summary of the Torque Results

	RPM / Torque	333	666	1000
Asymmetric TSF	Max (*Nm*)	10.71	35.00	82.91
	Min (*Nm*)	5.65	28.58	66.22
	Average (*Nm*)	8.28	32.25	72.81
	Ripple (%)	**61.11**	**19.91**	**22.92**
Non-unity TSF	Max (*Nm*)	10.66	34.66	74.68
	Min (*Nm*)	5.57	28.89	68.81
	Average (*Nm*)	8.34	32.33	72.30
	Ripple (%)	**61.03**	**17.85**	**8.12**
Torque Ripple Decrease (%)		**0.13**	**10.35**	**64.57**

Table 2.5. Summary of the Phase Current Results

	RPM / Current	333	666	1000
Asymmetric TSF	Max Peak (*A*)	15.58	35.99	87.58
	RMS (*A*)	6.41	16.25	37.44
Non-unity TSF	Max Peak (*A*)	14.92	41.50	106.64
	RMS (*A*)	6.25	16.52	40.94
Max Peak Current Increase (%)		**-4.24**	**15.31**	**21.76**
RMS Current Increase (%)		**-2.50**	**1.66**	**9.35**

2.5 Summary

In this chapter, a new self-tuning FLC based speed controller of the SRG for wind energy applications has been presented. The proposed controller consists of three main parts: turn-on and turn-off angle determination, self-tuning FLC, and a current controller. Owing to its doubly salient structure and excessive magnetic saturation, the SRG possesses an inherent

characteristic of strong nonlinearity. This nonlinearity makes the application of traditional linear control to the SRG difficult and unsatisfactory. However, the proposed control method has better adaptability which provides better performance over a wide range of operating conditions. The comparative simulations with a traditional PI controller and in combination with a wind turbine have verified the effectiveness and improvement in performance of the proposed controller.

Furthermore, a new non-unity TSF for the SRG at high speeds has been presented. As the name implies, its sum of all the individual phase torque references (normalized) is not unity. The ripple components are inserted deliberately into the torque reference by introducing two additional control parameters. These ripple components in the torque reference behave in such a way that they cancel out the actual ripples in the output torque during the high speed operation. In addition, a piecewise quadratic curve is employed to improve the performance further by reducing the rate-of-change of the current reference. The simulation results show that, even though the conventional asymmetric TSF has satisfactory performance at low speeds, the torque ripples can be reduced significantly by employing the proposed TSF at high speeds. Therefore, the non-unity TSF can minimize the torque ripples over a wider speed range of operation than the conventional TSFs.

References

[1]   D.A. Torrey, "Switched reluctance generators and their control," IEEE Trans. on Industrial Electronics, vol. 49, no. 1, pp. 3-14, Feb. 2002.

[2]   R. Cardenas, T. Pena, M. Peres, J. Clare, G. Asher, and P. Wheeler, "Control of a switched reluctance generator for variable-speed wind energy applications," IEEE Trans. on Energy Conversion, vol. 20, no. 4, pp. 781-791, Dec. 2005.

[3]   I. Kioskeridis and C. Mademlis, "Optimal efficiency control of switched reluctance generators," IEEE Trans. on Power Electronics, vol. 21, no. 4, pp. 1062-1072, July 2006.

[4]   Y. Chang and C. Liaw, "On the design of power circuit and control scheme for switched reluctance generator," IEEE Trans. on Power Electronics, vol. 23, no. 1, pp. 445-454, Jan. 2008.

[5]   L. Xiang and Y. Lingzhi, "Optimization output voltage of SRG wind power generation system," proc. of Power and Energy Engineering Conference (APPEEC), 2011 Asia-Pacific, pp. 1-4, Mar. 2011.

[6]   S. Bolognani and M. Zigliotto, "Fuzzy logic control of a switched reluctance motor drive," IEEE Trans. on Industry Applications, vol. 32, no. 5, pp. 1063-1068, Sep/Oct. 1996.

[7]   S.C. Wang and Y.H. Liu, "A modified PI-like fuzzy logic controller for switched reluctance motor drive," IEEE Trans. on Industrial Electronics, vol. 58, no. 5, pp. 1812-1825, May 2011.

[8]   M. Cheng, Q. Sun, and E. Zhou, "New self-tuning fuzzy PI control of a novel doubly salient permanent-magnet motor drive," IEEE Trans. on Industrial Electronics, vol. 53, no. 3, pp. 814-821, Jun. 2006.

[9]   S. Mir, M.E. Elbuluk, and I. Husain, "Torque-ripple minimization in switched reluctance motors using adaptive fuzzy control," IEEE Trans. on Industry Applications, vol. 35, no. 2, pp. 461-468, Mar./Apr. 1999.

[10]   D.S. Schramm, B.W. Williams, and T.C. Green, "Torque ripple reduction of switched reluctance motors by phase current optimal profiling," Proc. of Power Electronics Specialists Conference (PESC), 1992, pp. 857-860, 29 Jun.-3 Jul. 1992.

[11]   I. Husain and M. Ehsani, "Torque ripple minimization in swithced reluctance drives by PWM current control," IEEE Trans. on Power Electronics, vol. 11, no. 1, pp. 83-88, Jan. 1996.

[12]   X.D. Xue, K.W.E. Cheng, and S.L. Ho, "Optimization and evaluation of toque-sharing-functions for torque ripple minimization in switched reluctance motor drives," IEEE Trans. on Power Electronics, vol. 24, no. 9, pp. 2076-2090, Sep. 2009.

[13]   V.P. Vujicic, "Minimization of torque ripple and copper losses in switched reluctance drive," IEEE Trans. on Power Electronics, vol. 27, no. 1, pp. 388-399, Jan. 2012.

[14]   L. Moreau, M. Machmoum, and M.E. Zaim, "Control and minimization of torque ripple in switched reluctance generator," Proc. of Power Electronics and Applications, 2005 European Conference, pp. 1-8.

[15]   R. Fletcher, *Practical Methods of Optimization*, second edition, Wiley, ISBN: 0-4714-9463-1, May 2000.

[16]   R. Krishnan, *Switched Reluctance Motor Drives – Modeling, Simulation, Analysis, Design, and Application*, CRC Press, ISBN:0-8493-0838-0.

[17]   H. Le-Huy and P. Brunelle, "A versatile nonlinear switched reluctance motor model in Simulink using realistic and analytical magnetization characteristics," proc. of Industrial Electronics Society (IECON), 2005, pp. 1556-1561, Nov. 2005.

[18]   V.P. Vujicic, "Modeling of a switched reluctance machine based on the invertible torque fuction," IEEE Trans. on Magnetics, vol. 44, no. 9, pp. 2186-2194, Sep. 2008

Chapter 3

High-Power DC-DC Converters

3.1 Introduction

Recently, dc grids are regaining much attention internationally owing to the fast increasing penetration of renewable energy sources into power grids. Since modern power electronic interfaces enable the renewable energy sources to produce dc power directly, research on connecting these dc sources directly to a dc distribution system has been carried out extensively. A dc distribution has a great potential to overcome the major technical challenges faced by the traditional ac systems [1]-[4]. In wind power applications, many studies on a High Voltage DC (HVDC) transmission system connecting a large offshore wind farm to an onshore grid have already been conducted [5]-[7] extensively. Furthermore, employing a dc power collecting grid within a wind farm is another hot issue in this field [8]-[12].

The traditional ac power collecting grid in a wind farm could be entirely replaced by a dc grid. By employing the internal dc grid, traditional low-frequency (50 *Hz* or 60 *Hz*) transformers and ac cables can be replaced with medium-frequency transformers and dc cables. Since the size and weight of the medium-frequency transformers and the dc cables are significantly lower than those of the traditional ac ones at the same power ratings, the dc network could be a promising solution especially for the offshore wind farm applications, where the size and weight of components are highly related to the entire system costs in terms of substructure requirements, shipping and installation [13].

High-power dc-dc converters are fundamental and essential components when interconnecting wind turbines using a dc network within a wind farm. Since the success of the dc grids is critically dependent upon the high-power dc-dc converters, active research is currently being undertaken to develop practical high-power dc-dc converters [14]-[16]. Fig. 3.1 shows three different topologies of the most basic and commonly-used unidirectional high-power dc-dc converters: Full-Bridge (FB), LCC resonance, and Single Active Bridge (SAB) dc-dc converters. They all consist of a full-bridge converter on the input side, a diode bridge on the output side, a medium-frequency transformer, and passive components. The only difference is the utilization of the passive components. In this thesis, the unidirectional converters are mainly considered because the bidirectional power flow capability is of less importance for the offshore wind farm applications [14].
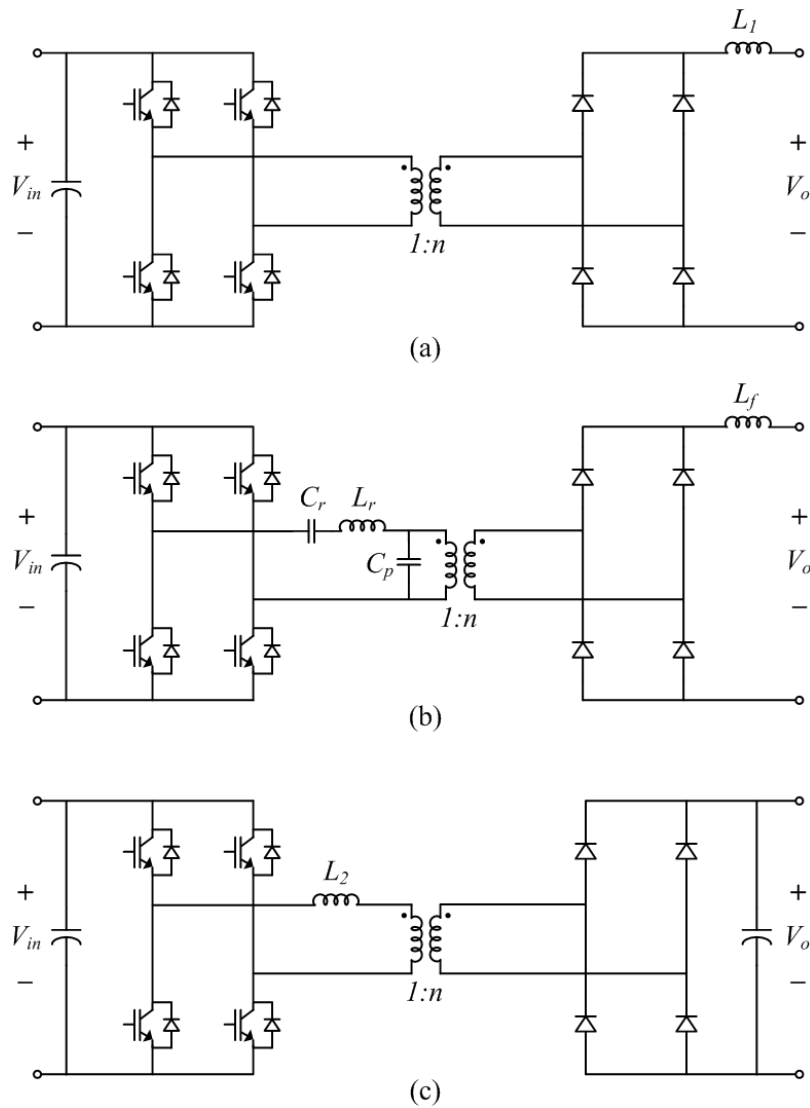

Fig. 3.1. Topologies of (a) Full-Bridge (FB), (b) LCC resonance, and (c) Single Active Bridge (SAB) dc-dc converters.

Max et al. in [10] have presented a detailed study on the losses of these dc-dc converters in a wind farm using an internal dc grid. They have concluded that the FB dc-dc converter (Fig. 3.1(a)) with a hard-switching duty cycle control is the most suitable topology in terms of efficiency for the wind farm application. However, the FB dc-dc converter requires a very large filter inductance (L_1, around tens or hundreds of millihenries) to operate in a Continuous Conduction Mode (CCM). Especially for high-power applications (MW-level), the size and weight of the filter inductor might be unacceptably large. In case of the resonant dc-dc converter (Fig. 3.1(b)), it also requires large resonant inductance and capacitance. In addition, since the resonant dc-dc converter operates in a wide range of frequencies, the dimensioning of these passive components is not an easy task.

To reduce the filter inductance as much as possible and to keep the topology and control as simple as possible, it is worth reconsidering the advantages of the SAB dc-dc converter (Fig. 3.1(c)). Since the SAB dc-dc converter operates in a Discontinuous Conduction Mode (DCM), only a small inductance (L_2) is required to limit the maximum amplitude of the current in the primary side of the transformer. In addition, the leakage inductance of the transformer now can be fully utilized. However, a major disadvantage of the SAB dc-dc converter is its higher current peaks, which could result in higher current ratings in both the input- and output-side power circuits.

A parallel-connected modular concept can be employed to reduce the current rating of each component in the power circuit. By paralleling lower-power modular SAB dc-dc converters, the current rating of each modular converter can be reduced. Furthermore, by interleaving the switching sequences of the modular converters, the magnitudes of input and output current ripples can be significantly reduced and the effective ripple frequency of the overall converter can be increased without increasing switching losses or device stresses.

In this chapter, to realize a practical high-power dc-dc converter, a parallel-connected SAB (PCSAB) dc-dc converter will be proposed first. To reduce the current rating of each power semiconductor switch, modular SAB dc-dc converters are paralleled. In addition, the paralleled converters are controlled to interleave the output currents so that the overall output current ripple can be reduced significantly. Analysis of both the input and output current characteristics and design aspects of its transformer, filter inductor, and input and output filter capacitors will be presented.

Although the PCSAB requires a small amount of the filtering inductance, it still has another problem which hampers the further growth of the power level of the converter, namely, high power losses in the switching devices. From the traditional full-bridge dc-dc

converters, it is already known that the soft-switching technique using the phase-shift control is not beneficial for high-power (MW levels) converters since the circulating current would increase the conduction loss, and additional snubber circuits and precise timing control are required, which will increase the complexity of the system. [17], [18]. Therefore, the hard-switching technique with the simple duty-cycle control seems the preferred choice. If the hard-switching is used, the main source of the converter losses is the switching loss. Therefore, reducing both the power losses and the filter inductance is very important for realizing a practical high-power dc-dc converter.

Therefore, in this chapter, a novel Double Uneven Power (DUP) converter based dc-dc converter and its design and control methods will be introduced as well. The proposed converter utilizes two full-bridge converters in a special way to realize the Zero-Current-Switching (ZCS), where both the turn-on and turn-off switching occur under the zero-current condition. The proposed DUP converter is designed for high power (MW-levels) applications, where the voltage level transformation is required. The main objectives of the proposed converter are (1) to reduce the switching power losses in the power semiconductor devices and (2) to reduce the output filter inductance. The proposed converter is expected to be highly beneficial for high-power applications, such as dc-transmission grid or dc-collection systems in offshore wind farms.

3.2 DC-Grid Wind Farm Configuration

An example of an offshore wind farm configuration with an internal dc-grid is shown in Fig. 3.2. In this configuration, wind turbines are connected in paralleled radials to a 'station' dc-dc converter which is responsible for stepping up the voltage from the collection (distribution) level to the transmission level, and controlling the internal dc grid voltage as constant as possible. Within each wind turbine, a generator is connected to a full-power active rectifier, which is responsible for regulating the power output of the generator, for example to track the Maximum Power Points (MPPs), and the rectifier is connected to an 'internal' dc-dc converter. This 'internal' dc-dc converter is responsible for stepping up the voltage from the generator level to the collection level, and maintaining the internal dc-link voltage as constant as possible.

There are three dc voltage levels (generator, collection, and transmission) in the overall wind farm configuration. The dc-link voltage level for high-power wind turbines usually ranges from several kV up to around 10 kV. The voltage level for the dc collection grid is normally from 30 kV to 60 kV and that for the dc transmission is from 150 kV or even

higher, which depends on the power rating of wind farm and its distance to the shore [5]-[12]. Between these voltage levels, dc-dc converters, which are capable of boosting and handling a large amount of voltage and power, are required. In this thesis, the generator, collection, and transmission voltages are assumed to be 5 kV, 50 kV, and 150 kV, respectively. Therefore, the required voltage gains for the 'internal' and 'station' dc-dc converters are 10 and 3, respectively.
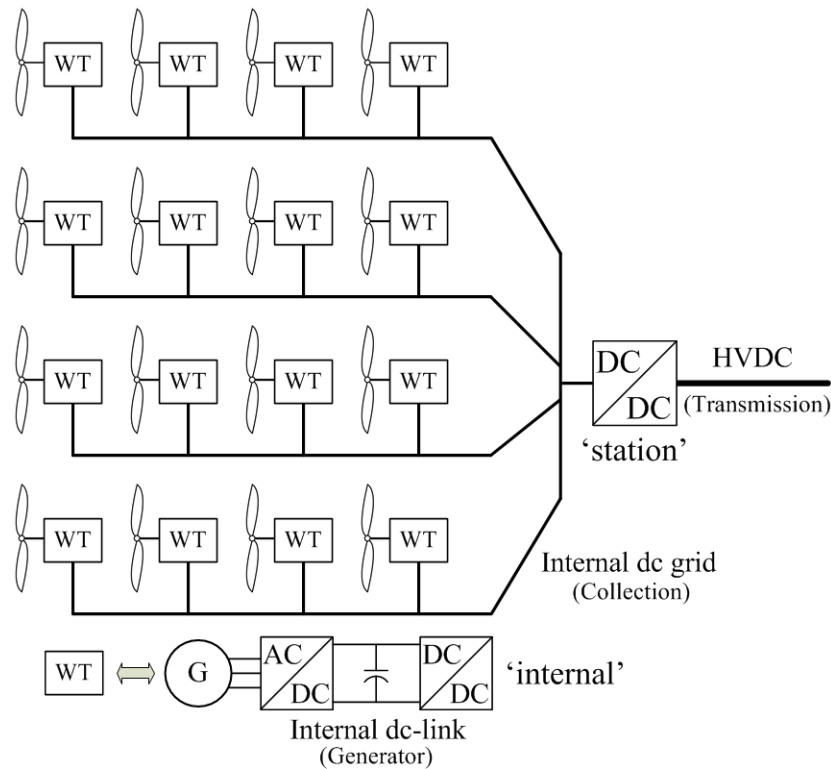

Fig. 3.2. Example of an offshore wind farm configuration with an internal dc collection grid.

3.3 Parallel-Connected Single Active Bridge DC-DC Converter

3.3.1 Review on a Single Active Bridge (SAB) dc-dc converter

3.3.1.1 Steady-State Analysis using an Equivalent Circuit

Equivalent Circuit

Since the SAB dc-dc converter has a voltage stiff output, it has different characteristics from the FB dc-dc converter and should be controlled in a different way. The SAB dc-dc converter can be modelled as a simple buck converter when it is referenced to the primary side of the transformer as shown in Fig. 3.3. Here, V_{in} and V_o are the input and output voltages, respectively, and n is the turn-ratio of the transformer.
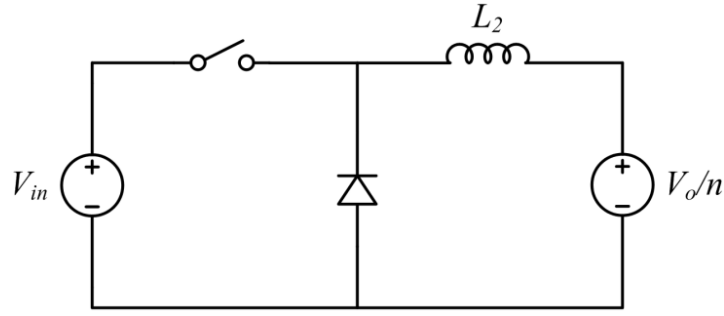
Fig. 3.3. Equivalent circuit for the SAB dc-dc converter.

It should be noted that L_2 represents the filter inductance together with the leakage inductance of the transformer as shown in Fig. 3.1(c). Hence, if the leakage inductance can be designed big enough, no additional filter inductor might be required. Furthermore, due to the full-wave rectification of the diode bridge, to deliver the same amount of power, the equivalent buck converter has a half switching period and a twofold duty-ratio compared with the SAB dc-dc converter as shown in Fig. 3.4, where T_s is the switching period and D is the duty-ratio of the SAB dc-dc converter.

$$T_s' = \frac{T_s}{2}$$

$$D' = 2D$$

(3.1)
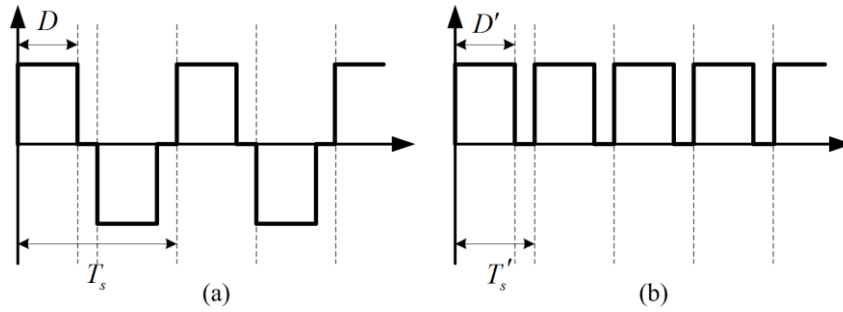
Fig. 3.4. Switching periods and duty-ratios for (a) the SAB dc-dc converter and (b) the equivalent buck converter.

Condition for the Discontinuous Conduction Mode (DCM)

If it is assumed that the equivalent circuit is operating at its rated power with the maximum duty ratio, D'_{max}, the amount of the current rise in the inductor while the switch is turned on can be calculated as

$$\Delta i_L = \frac{V_{in} - V_o/n}{L_2} D'_{max} T_s'.$$

(3.2)

Likewise, the amount of the current fall while the switch is turned off at the rated power can be expressed as

$$\Delta i_L' = \frac{-V_{in} - V_o/n}{L_2}(1 - D'_{max})T_s'. \tag{3.3}$$

Since the amount of the current rise should always be the same as that of the current fall under the steady-state, the maximum duty-ratio for the DCM can be expressed as below.

$$\begin{aligned} |\Delta i_L| &= |\Delta i_L'| \\ D'_{max} &= \frac{1}{2} + \frac{V_o}{2 \cdot n \cdot V_{in}} \end{aligned} \tag{3.4}$$

As it can be noticed from (3.4), the maximum duty-ratio up until which the converter remains in the DCM is restricted by the input and output voltages and the transformer turn-ratio.

Average Output Current in the DCM

The average output current in the DCM can be calculated using the inductor current and the switching function. Since the output current is rectified by the secondary-side diode bridge, the equivalent primary-side current can be represented as Fig. 3.5.
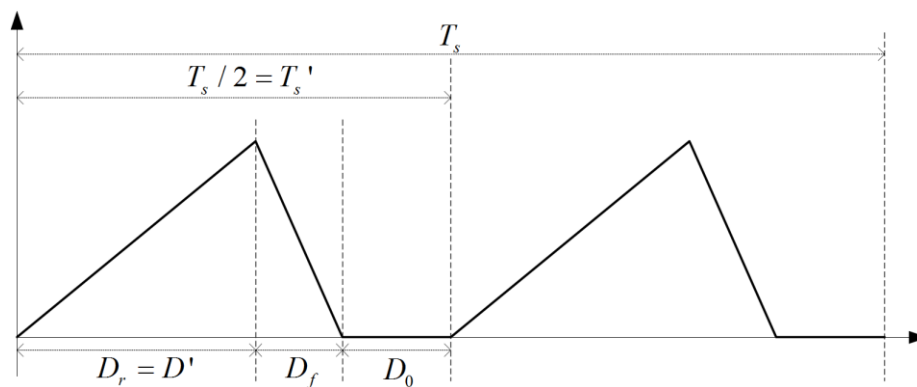

Fig. 3.5. Equivalent primary-side current waveform.

D_r is the duty-ratio for the current rise, D_f for the current fall, and D_0 for the zero conduction period. To calculate the total conduction time, D_f should be obtained first. Since the absolute amplitudes of the current rise and fall should be the same in the steady-state, D_f can be expressed as below.

39

$$\left| \Delta i_r \right| = \left| \Delta i_f \right|$$

$$D_f = \frac{V_{in} - V_o / n}{V_{in} + V_o / n} D_r$$

(3.5)

From (3.5), the total conduction time, t_c, can be calculated as

$$t_c = (D_r + D_f)T_s' = \frac{2V_{in}}{V_{in} + V_o / n} D_r T_s'.$$

(3.6)

Therefore, the average current in the primary side can be expressed as

$$I_{in} = \frac{1}{T_s'}(\frac{1}{2} \cdot \left| \Delta i_r \right| \cdot t_c) = \frac{V_{in}}{L_2} \frac{(V_{in} - V_o / n)}{(V_{in} + V_o / n)} D_r{}^2 T_s'.$$

(3.7)

Finally, since the output side current is ($I_o = I_{in}/n$), the average output current is

$$I_o = \frac{V_{in}}{n \cdot L_2} \frac{(V_{in} - V_o / n)}{(V_{in} + V_o / n)} D_r{}^2 T_s'.$$

(3.8)

As it can be seen from (3.8), the average output current is a nonlinear function of D_r.

3.3.1.2 Design Aspects

In this subchapter, various design aspects of the SAB dc-dc converter will be presented with one exemplary design specification, which is shown in Table 3.1.

Table 3.1. Exemplary Design Specification.

Rated Power	5 MVA
Input Voltage	5 kV
Output Voltage	50 kV
Switching Frequency	1 kHz

Transformer Design

Unlike other conventional dc-dc converters using transformers, the transformer leakage inductance in the SAB dc-dc converter might be a desired component. The leakage inductance can be utilized as the filter inductance without the need for additional inductance in the primary side of the transformer. Since the transformer requires a larger leakage inductance, the primary and secondary windings do not need to be coupled tightly to achieve a high coupling factor, which is much easier to manufacture and has better voltage isolation capability and lower capacitance between the primary and secondary windings. If the leakage

inductance of the transformer is not big enough, then an additional filter inductor might be inserted in series in the primary side of the transformer.

The transformer turn-ratio should be designed by taking into account the worst case where the input voltage is the lowest possible and the output voltage is the highest possible. In addition, a loss of duty-ratio, due to various voltage drops in the power circuits and stray resistances in the transformer and the cables, should be considered as well. Assuming that an allowed peak voltage deviations are ±5% of the nominal voltage level and the loss of duty-ratio is 5%, the transformer turn-ratio, n, can be designed as

$$n = \frac{1.05 \cdot V_o}{0.95 \cdot 0.95 \cdot V_{in}} = \frac{1.05 \cdot 50k}{0.95 \cdot 0.95 \cdot 5k} = 11.63 . \tag{3.9}$$

Therefore, from (3.4), the maximum duty-ratio (D'_{max}) under the DCM is 0.93 for this example.

Filter Inductance

If the allowed ripple size of the output current at the rated power is set to 100 A, which is 100% of the nominal output current, the maximum ripple size of the input current, Δi_{ripple}, should be 1163 (100×11.63) A according to the transformer turn-ratio. Hence, from (3.2), the inductance required in the primary side of the transformer is

$$L_2 = \frac{V_{in} - V_o / n}{\Delta i_{ripple}} D'_{max} T_s' = 139.94 \mu H , \tag{3.10}$$

which is more than 135 (=11.63^2) times as small as the output filter inductance required for the FB dc-dc converter under the same ripple current size condition.

Input Filter Capacitance

Assuming that the average input current, I_{in}, to the input capacitor is constant during one switching period, the current into the converter, i_{conv_in}, at the rated power can be drawn as Fig. 3.6. It is worth noting that the current ripple frequency is twice as high as the switching frequency.
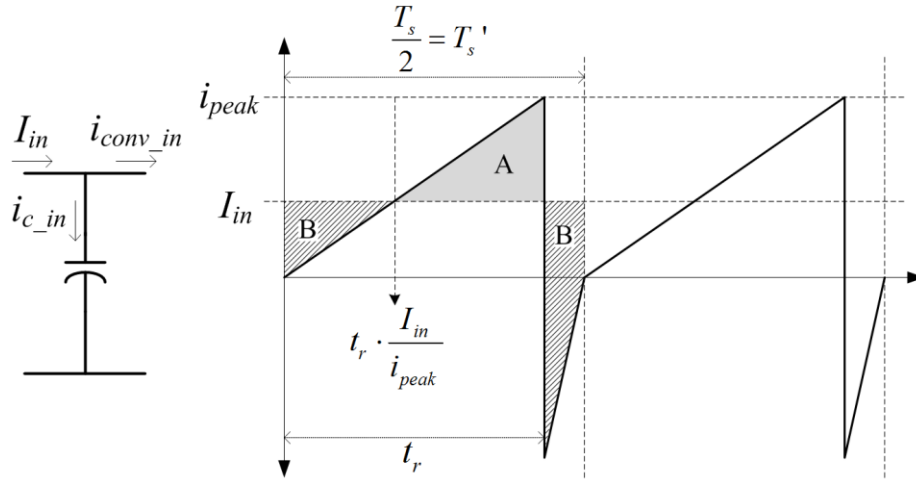
Fig. 3.6. Input current waveform into the SAB converter at the rated power.

Area 'A' represents the amount of excessive charge that is drawn to the converter and Area 'B' represents the excessive charge into the capacitor. Area 'A' causes a voltage drop in the capacitor; on the other hand, Area 'B' causes a voltage rise. Therefore, by calculating the area of either 'A' or 'B', the magnitude of the peak to peak voltage ripple in the capacitor can be obtained. Calculating the area 'A', the voltage ripple can be expressed as

$$\Delta V_c = \frac{1}{C_{in}}\left(\frac{t_r \cdot i_{peak}}{2} - t_r \cdot I_{in}\left(1 - \frac{1}{2}\frac{I_{in}}{i_{peak}}\right)\right), \tag{3.11}$$

where i_{paek} is the peak input current and t_r $(=D_rT_s')$ is the current rise time.

Therefore, by rearranging (3.11) for C_{in}, the minimum capacitance required to restrict the ripple size to ΔV_c can be obtained. Assuming the voltage ripple due to the converter switching is restricted to 5% of its nominal value, the minimum capacitance required for this design example is calculated to be 703 μF.

Output Filter Capacitance

Assuming that the average current to the load, I_{load}, is constant during one switching period, the output current from the converter, i_{conv_o}, at the rated power can be drawn as below. It is worth noting that the voltage ripple frequency in the output is also twice as high as the switching frequency.
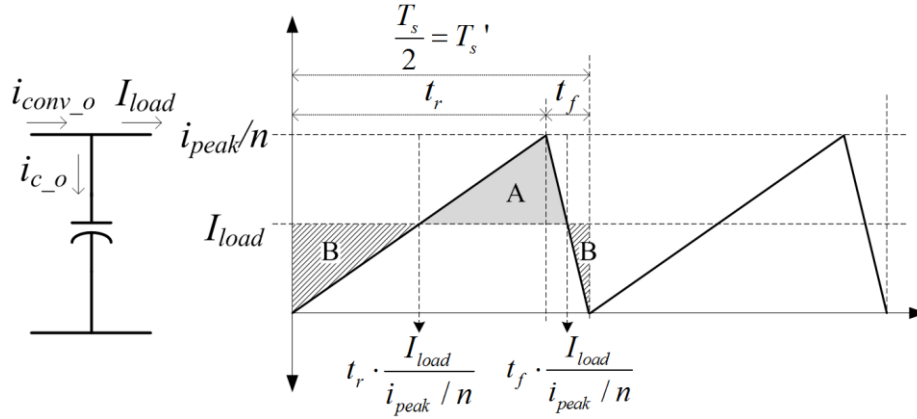
Fig. 3.7. Output current waveform from the SAB converter at the rated power.

Similar to the case of the input filter capacitance, Area 'A' represents the amount of excessive charge that is pushed into the output filter capacitor so that it causes a voltage rise in the output filter capacitor; on the other hand, Area 'B' causes a voltage drop. Therefore, by calculating the area 'A', the voltage ripple can be expressed as below.

$$\Delta V_c = \frac{1}{C_o}\left(\frac{(t_r+t_f)\cdot i_{peak}/n}{2} - (t_r+t_f)\cdot I_{load}\left(1-\frac{1}{2}\frac{I_{load}}{i_{peak}/n}\right)\right) \qquad (3.12)$$

Therefore, by rearranging (3.12) for C_o, the minimum capacitance required to restrict the ripple size to ΔV_c can be obtained. The minimum capacitance required for the design example is calculated to be 5 μF when the ripple caused by the converter switching is restricted to 5% of its nominal value.

It should be mentioned here that the actual input and output capacitances are usually designed by taking into account other factors such as dynamics of sources and loads connected to the dc-dc converter or the dynamic characteristics of the controller used to control its input or output voltage. However, in this subchapter, only the steady-state characteristics of the converter have been analysed.

3.3.2   Steady-State Analysis of a Parallel-Connected SAB DC-DC Converter

The circuit configuration of a parallel-connected SAB dc-dc converter is shown in Fig. 3.8. Paralleling of lower-power modular converters offers higher efficiency, better dynamic response, redundancy implementation, and ease of maintenance [19]. These characteristics are highly beneficial especially for offshore wind farm applications.
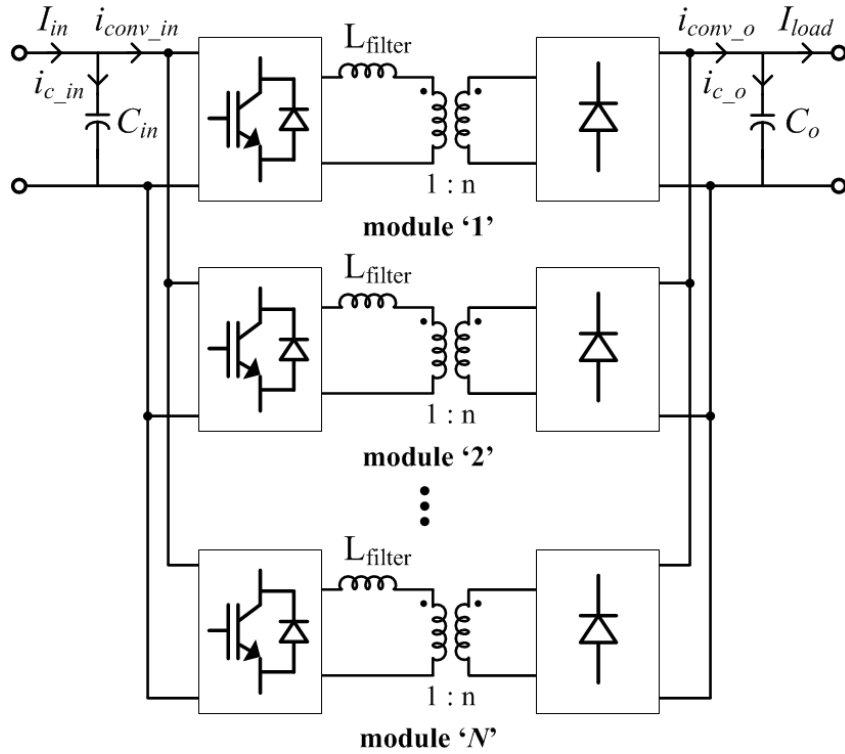
Fig. 3.8. *N*-parallel-connected SAB dc-dc converter.

3.3.2.1 Filter Inductance and Transformer Turn-Ratio

If *N* numbers of the modular converters are connected in parallel, each module can have *N* times as small power, input current, and output current ratings, but the input and output voltage ratings remain the same. Therefore, the filter inductance required, when a single converter is used (*L_s*), is the same as (3.10). Due to (3.1), (3.10) can be rewritten as

$$L_s = \frac{V_{in} - V_o / n}{\Delta i_{ripple}} D_{\max} T_s \tag{3.13}$$

where *V_{in}* and *V_o* are the nominal input and output voltages, *n* is the transformer turn-ratio, and *T_s* is the switching period of the converter. Δi_{ripple} is the maximum peak-to-peak ripple of the input current at the maximum duty-ratio, *D_{max}*, up to which the converter remains in the DCM. Due to (3.1), (3.4) can be rewritten as

$$D_{\max} = \frac{1}{4} + \frac{V_o}{4 \cdot n \cdot V_{in}} \tag{3.14}$$

Since paralleling the converters lowers the input impedance of the overall converter, *N* times as large filter inductance for each module is required in the primary side of the

transformer to transfer the same amount of the overall power. Therefore, the filter inductance required for each module in the N-parallel configuration can be expressed as

$$L_{filter} = N \cdot L_s = N \cdot \frac{V_{in} - V_o / n}{i_{ripple}} D_{max} T_s \qquad (3.15)$$

.

It is worth noting that the filter inductance is a limiting factor for increasing the number of modular converters in parallel, since the size and weight of the filter inductor with large inductance might be unacceptably large for high-power applications. However, unlike the conventional FB converter, each filter inductor in this study is located in the primary-side of the transformer as shown in Fig. 3.8. If the filter inductors were placed in the secondary side, the required filter inductance would have been n^2 times larger than the value calculated by (3.15). Hence, the applications especially with a high value of n can benefit from a large reduction in the required filter inductance compared with the conventional full-bridge converter. Furthermore, the leakage inductance of the transformer can now be fully utilized. In other words, no additional filter inductance would be required if the leakage inductance is designed to be big enough. This characteristic is also highly beneficial when n is quite large.

The same principle also applies to each transformer within the modular converter. The power and current ratings of the transformer is, now, N times as small. However, since the input and output voltage ratings remain the same, the transformer turn-ratio, n, which only depends on the input and output voltages, remains the same as (3.9).

3.3.2.2 *Steady-State Input Current and Voltage*

Assuming the input current to an input capacitor, I_{in}, is constant during a switching period, a current waveform into a 3-paralleled SAB converter, i_{conv_in}, at the rated power can be drawn as Fig. 3.9. The 3-parallel converter is used here only for representation and the rest of the explanation will be given for the N-parallel converter. The input current in each modular converter increases while the switches are turned on ($t_r = D_{max} T_s$), and the current is pushed back into the input capacitor in a regenerative way through the antiparallel diodes while the switches are turned off ($t_f = (0.5 - D_{max}) T_s$). The currents in the modular converters are equally phase-shifted to reduce the ripple size of the total input current.
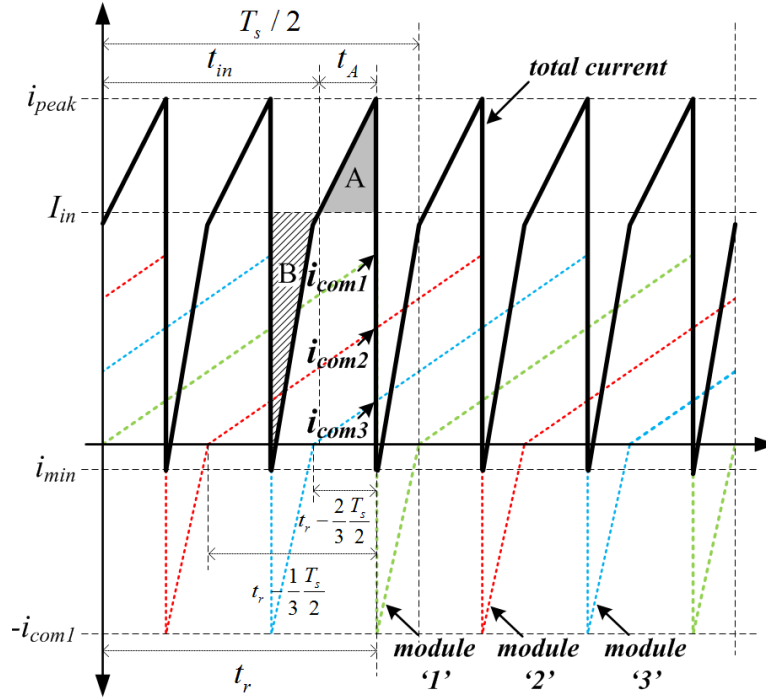
Fig. 3.9. Input current waveform to the 3-paralleled SAB converter at the rated power.

Since the input current to the capacitor is assumed to be constant, the area 'A' represents the amount of excessive charge that is drawn into the converter and the area 'B' represents the excessive charge into the input capacitor. The area 'A' and the area 'B' cause a voltage drop and a voltage rise, respectively. Therefore, by calculating the area of either 'A' or 'B', the magnitude of the peak-to-peak voltage ripple in the input capacitor can be obtained. It is worth noting that the current ripple frequency is $2 \cdot N$ times as high as the switching frequency.

The maximum peak current (i_{peak}) can be obtained by summing up all the component currents (i_{com1}, i_{com2} ... i_{comN}) of the N-parallel converter, when any one of the component currents reaches its maximum value. Therefore, the maximum peak current can be expressed as below.

$$
\begin{aligned}
i_{peak} &= i_{com1} + i_{com2} + ... + i_{comN} \\
&= (\frac{V_{in} - V_o / n}{N \cdot L_s}) D_{max} \cdot T_s \\
&\quad + (\frac{V_{in} - V_o / n}{N \cdot L_s})(D_{max} \cdot T_s - \frac{1}{N} \cdot \frac{T_s}{2}) + \\
&\quad ... + (\frac{V_{in} - V_o / n}{N \cdot L_s})(D_{max} \cdot T_s - \frac{N-1}{N} \cdot \frac{T_s}{2}) \\
&= (\frac{V_{in} - V_o / n}{L_s})(D_{max} - \frac{(N-1)}{4N}) \cdot T_s
\end{aligned}
\tag{3.16}
$$

Since the time when the current to the parallel converter (i_{conv_in}) reaches the value of the input current (I_{in}) is

$$t_{in} = \frac{L_s \cdot I_{in}}{V_{in} - V_o / n} + \frac{N-1}{4 \cdot N} T_s ,$$

(3.17)

and $t_A = D_{max} \cdot T_s - t_{in}$, by calculating the area of 'A', the maximum peak-to-peak voltage ripple due to the converter switching can be expressed as

$$\Delta V_c = \frac{1}{C_{in}} \frac{(i_{peak} - I_{in}) \cdot t_A}{2} ,$$

(3.18)

where C_{in} is the input capacitance. When the input capacitance is designed, the transient requirements of the overall system, such as dynamics of both the source and load connected to the converter, or the dynamic characteristics of the controller used to control its input or output voltage, should be taken into account.

Furthermore, the minimum input current (i_{min}) can be expressed as

$$i_{min} = -i_{com1} + i_{com2} + ... + i_{comN}$$

(3.19)

,

and the maximum peak-to-peak current ripple can be expressed as

$$\Delta i_{conv\_in} = i_{peak} - i_{min} = 2 \cdot i_{com1}$$
$$= 2(\frac{V_{in} - V_o / n}{N \cdot L_s}) D_{max} T_s ,$$

(3.20)

which means the maximum peak-to-peak current ripple is always two times of the peak current of the modular converter (i_{com1}). Since the peak current of the modular converter is inversely proportional to the number of converters (N), the maximum peak-to-peak current ripple is also inversely proportional to the number of converters.

3.3.2.3 Steady-State Output Current and Voltage

Assuming an output current to a load, I_{load}, is constant during a switching period, a current waveform from the 3-paralleled SAB converter, i_{conv_o}, at the rated power can be drawn as Fig. 3.10. The 3-parallel converter is again used here only for representation. Likewise the input current, the output current in each modular converter increases while the switches are turned on (t_r), but the output current simply decreases while the switches are

turned off (t_f). The output currents in the modular converters are also equally phase-shifted so that the ripple size of the total output current is reduced significantly.
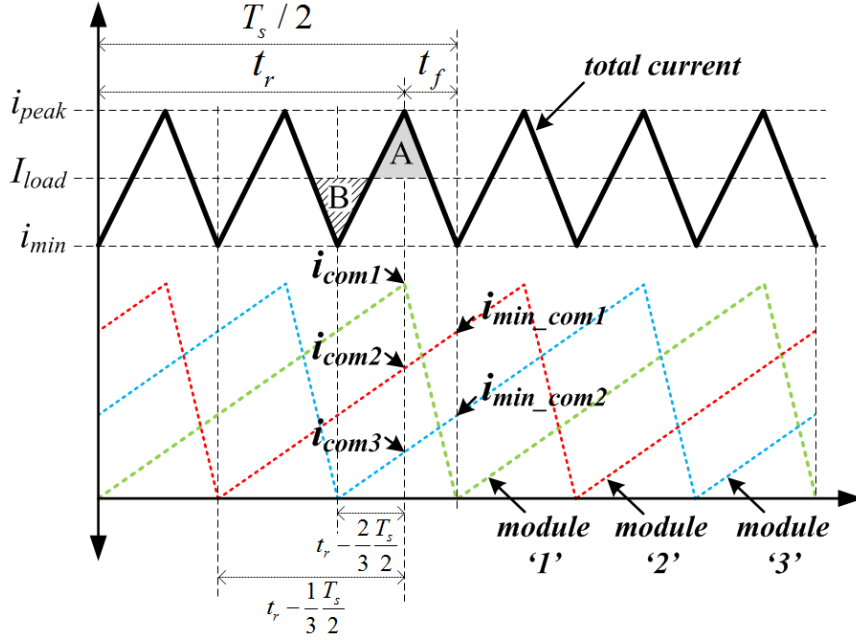

Fig. 3.10. Output current waveform from the 3-paralleled SAB converter at the rated power.

Similar to the case of the input filter capacitance, the area 'A' and 'B' represent the amounts of excessive charge and deficit charge, respectively, in the output filter capacitor. Therefore, by calculating the area of either 'A' or 'B', the magnitude of the peak-to-peak voltage ripple in the output capacitor can be obtained. Again, the effective ripple frequency of the output current is $2 \cdot N$ times as high as the switching frequency.

The maximum peak current (i_{peak}) can also be obtained by summing up all the component currents (i_{com1}, i_{com2} ... i_{comN}), when any one of the component currents reaches its maximum value. Hence, the maximum peak current can be expressed as

$$
\begin{aligned}
i_{peak} &= i_{com1} + i_{com2} + ... + i_{comN} \\
&= \frac{1}{n}\left(\frac{V_{in} - V_o/n}{N \cdot L_s}\right)D_{max} \cdot T_s \\
&\quad + \frac{1}{n}\left(\frac{V_{in} - V_o/n}{N \cdot L_s}\right)\left(D_{max} \cdot T_s - \frac{1}{N} \cdot \frac{T_s}{2}\right) \\
&\quad ... + \frac{1}{n}\left(\frac{V_{in} - V_o/n}{N \cdot L_s}\right)\left(D_{max} \cdot T_s - \frac{N-1}{N} \cdot \frac{T_s}{2}\right) \\
&= \left(\frac{V_{in} - V_o/n}{L_s}\right)\left(D_{max} - \frac{(N-1)}{4N}\right)\frac{T_s}{n}
\end{aligned}
\tag{3.21}
$$

48

By calculating the area of 'A', the maximum peak-to-peak voltage ripple due to the converter switching can be expressed as

$$\Delta V_c = \frac{1}{C_o} \frac{(i_{peak} - I_{load})}{2} \frac{T_s}{4 \cdot N},$$

(3.22)

where C_o is the output capacitance. By rearranging (3.22) for C_o, the minimum capacitance required to restrict the ripple size to ΔV_c can be obtained.

Furthermore, the minimum current (i_{min}) can also be calculated by summing up component currents (i_{min_com1}, i_{min_com2} ... $i_{min\_com(N-1)}$) of the N-parallel converter as

$$i_{min} = i_{min\_com1} + i_{min\_com2} + ... + i_{min\_com(N-1)}.$$

(3.23)

However, since the output current waveform is triangular and the area of 'A' and 'B' should be the same under the steady-state, the minimum current can be easily obtained as below.

$$\begin{aligned} i_{min} &= I_{load} - (i_{peak} - I_{load}) \\ &= 2I_{load} - i_{peak} \end{aligned}$$

(3.24)

Therefore, the maximum peak-to-peak ripple of the output current can be expressed as

$$\begin{aligned} \Delta i_{conv\_o} &= i_{peak} - i_{min} \\ &= 2(i_{peak} - I_{load}). \end{aligned}$$

(3.25)

3.3.2.4 Output Peak and Ripple Currents

The parallel operation of multiple modular converters has a very important advantage, an interleaved switching technique. The interleaved switching means that the multiple modular converters have the same switching pattern, but the switching instants are sequentially phase shifted. For example, if N lower-power modular converters are connected in parallel, all the modular converters are controlled with exactly the same switching pattern, but each switching signal has a (π/N) phase shift among each other. This arrangement reduces the amplitude of the net ripple and increases the effective ripple frequency of the overall converter without increasing switching losses or device stresses [20].

The normalized output peak current (i_{peak_n}) can be obtained as below using (3.21) by dividing the peak output current of an N-parallel converter (i_{paek}) by that of a single converter ($i_{paek(N=1)}$).

$$i_{peak\_n} = \frac{i_{peak}}{i_{peak(N=1)}} = 1 - \frac{(N-1)}{4 \cdot N \cdot D_{\max}} \quad (3.26)$$

Likewise, the normalized ripple current (i_{ripple_n}) can also be obtained as below using (3.25).

$$i_{ripple\_n} = \frac{i_{ripple}}{i_{ripple(N=1)}} = 1 - \frac{(N-1)}{2N \cdot D_{\max}} \quad (3.27)$$

Fig. 3.11 shows the reduction in the output peak and ripple current amplitudes depending on the number of the modular converters (N) when the output current is interleaved. As N increases, the amplitudes of both the output peak and ripple currents decrease. Therefore, determining N is all a matter of designing tradeoff between the current ratings and the filter inductance, because the required filter inductance increases proportionally to N. Although N can be varied depending on system requirements and applications, N for the simulations and experiments in this thesis is chosen to be 3, since the amount of reduction achieved significantly decreases as N increases over 3.
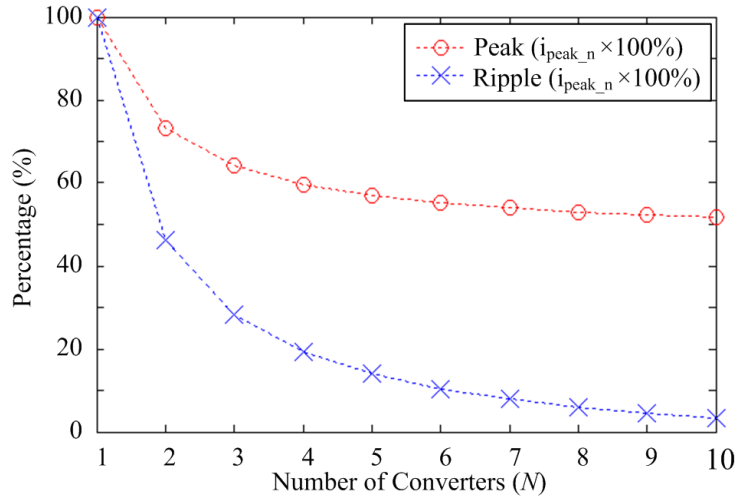
Fig. 3.11. Reduction in the amplitudes of the output peak and ripple currents depending on the number of parallel converters (N) at a rated power (assuming $D_{max} = 0.465$).

3.3.3 Input Voltage Control and Dynamic Analysis

3.3.3.1 Average Input Current

If the dc bus voltage (the output voltage of the dc-dc converter) is assumed to be constant, the input voltage of the dc-dc converter should be controlled to transfer power from the input side to the output side. To control the input voltage at a certain reference value, the

current flowing into the converter has to be controlled. Therefore, the average input current with respect to the duty-ratio of the converter should be obtained first.

Since the SAB converter operates in the DCM, the relationship between the average input current and the duty-ratio is not linear. Assuming that all the modular converters in the parallel configuration are identical, each modular converter draws the same amount of current per switching period. The input current waveform to each modular converter can be represented as Fig. 3.12. D_r is the duty-ratio for the current rise, which is equivalent to the switch turn-on duty-ratio D, D_f is the duty-ratio for the current fall, and D_0 is the duty-ratio for the zero conduction period.
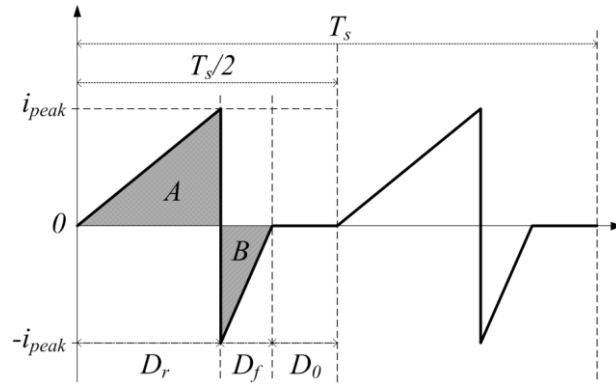

Fig. 3.12. Input current waveform to each modular converter at a certain duty-ratio.

Since the amplitudes of the current rise and fall should be the same ($|\Delta i_r| = |\Delta i_f|$), D_f can be calculated as

$$D_f = \frac{V_{in} - V_o / n}{V_{in} + V_o / n} D_r$$

(3.28)

which is identical to (3.5). Therefore, the average input current to each modular converter can be expressed as

$$
\begin{aligned}
I_{conv\_each} &= \frac{2}{T_s}(\frac{1}{2}i_{peak}D_r T_s - \frac{1}{2}i_{peak}D_f T_s) \\
&= \frac{2V_o \cdot T_s}{n \cdot N \cdot L_s} \frac{(V_{in} - V_o / n)}{(V_{in} + V_o / n)} D^2 \quad .
\end{aligned}
$$

(3.29)

Since N modular converters are connected in parallel, the total average output current is

$$I_{conv} = N \cdot I_{conv\_each}$$

(3.30)

.

3.3.3.2 PI Control based Input Voltage Controller

Since the relationship between the average input current and the duty-ratio is nonlinear, the parallel converter can be regarded as a nonlinear actuator. To compensate the nonlinearity of the actuator, the inverse of the characteristic of the actuator, which is the inverse function of (3.30), can be used [21]. A block diagram of the overall voltage control scheme is shown in Fig. 3.13.
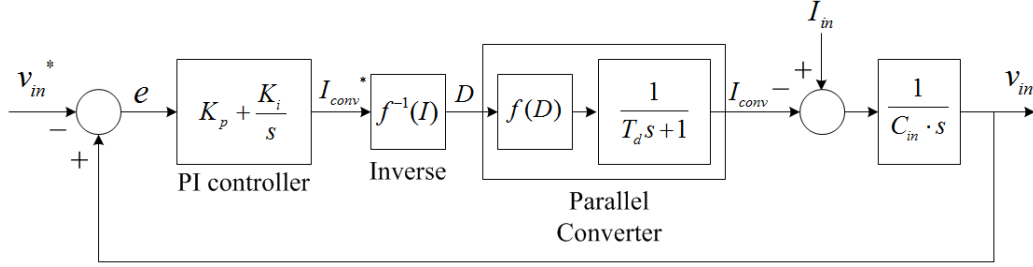

Fig. 3.13. PI control based input voltage control scheme.

As it can be seen from the block diagram, the converter is represented with the nonlinear function of the actuator and a first-order low-pass filter which represents the time delay of the converter system. When operating a real converter, there always exist various sources of time delay such as computational delay and measuring delay. In this system, the total delay for the converter is assumed to be 1.5 times switching period ($T_d=1.5 \cdot T_s$).

The inverse function, which is the inverse function of (3.30), can be expressed as

$$D = \sqrt{\frac{n \cdot L_s}{2 V_o T_s} \frac{(V_{in} + V_o / n)}{(V_{in} - V_o / n)}} \cdot \sqrt{I_{conv}} \tag{3.31}$$

.

As it can be seen from the above equation, the inverse function is a function of n, L_s, T_s, V_{in}, V_o, and I_{conv}. The transformer turn-ratio (n), single filter inductance (L_s) and switching period (T_s) are all known parameters and the input and output voltages (V_{in} and V_o) are measured values. Since it is often sufficient to use a fairly crude approximation for the inverse function [20], the constant nominal values for the input and output voltages under a normal operating condition can be used instead.

3.3.3.3 Gain Tuning for the PI Voltage Controller

If the nonlinearity of the system is compensated using the inverse function, the overall voltage control scheme can be redrawn as Fig. 3.14.
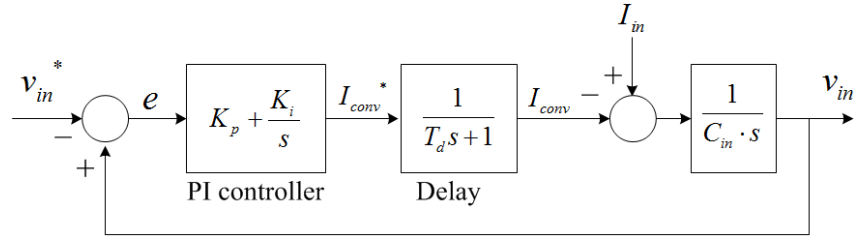
Fig. 3.14. Linearized input voltage control scheme.

To obtain proper gains for the PI controller, the 'symmetrical optimum design' method can be used [22, 23]. This method optimizes the control system behaviour with respect to a disturbance input by maximizing the phase margin at a crossover frequency.

Using the 'symmetrical optimum design' method, the proportional gain and the integral gain are

$$K_p = \frac{C}{a \cdot T_d}, \quad K_i = \frac{K_p}{a^2 \cdot T_d}, \tag{3.32}$$

where 'a' is the symmetrical distance between the corner frequency (K_i/K_p) of the PI controller to the crossover frequency, and the cut-off frequency ($1/T_d$) of the delay to the crossover frequency [24].

The crossover frequency is calculated to be

$$\omega_{co} = \frac{1}{a \cdot T_d}. \tag{3.33}$$

Since the relationship between a damping ratio (ζ) of the oscillatory part of the response and the symmetrical distance (a) is

$$\zeta = \frac{a-1}{2}, \tag{3.34}$$

the symmetrical distance is chosen to be 2.414, assuming $\zeta = 1/\sqrt{2}$.

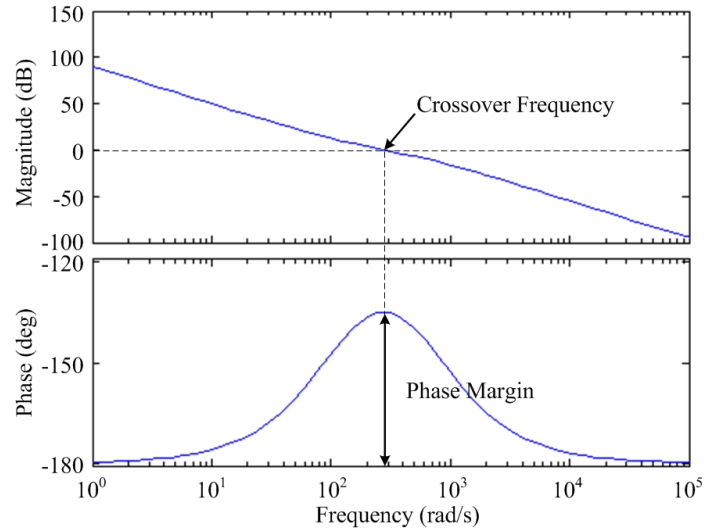A bode plot of the open loop transfer function of the system is shown in Fig. 3.15.

53

Fig. 3.15. Bode plot of the open loop transfer function of the system (a=2.414, T_d=1.5 ms).

3.3.3.4 Design of the Input Capacitance

Once the crossover frequency (or bandwidth) of the control system has been determined by the 'symmetrical optimum design' method, the magnitude of the overshoot due to the step change in the disturbance depends on the input filter capacitance. The relationship between the disturbance and the controlled input voltage can be represented as Fig. 3.16.
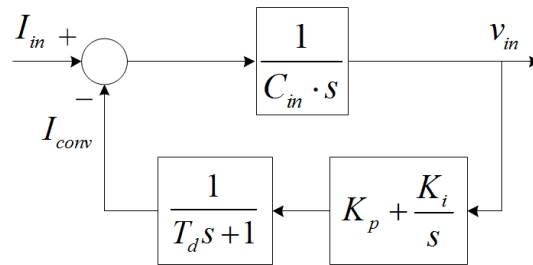
Fig. 3.16. Block diagram of the relationship between the disturbance and the controlled input voltage.

Fig. 3.17 shows the step responses of the system to the input current disturbance depending on various input filter capacitances. It can be observed that the magnitude of the overshoot varies depending on the input filter capacitance. Therefore, by selecting a proper amount of capacitance, the maximum peak voltage in the input capacitor can be restricted to a certain value. For example, if an allowed maximum voltage overshoot is 10% of the nominal voltage of 5 kV, that is 500 V, and an input current from the energy source changes from 0 to its rated value of 1000 A in a step manner, the ratio between the input current and the controlled voltage (or input impedance) should be restricted to 0.5 Ω (500V/1000A). Therefore, according to Fig. 3.17, approximately 6 mF can be chosen for this example.

54

Fig. 3.17. Unit step responses to a disturbance depending on the input filter capacitance.

3.3.3.5 Simulations

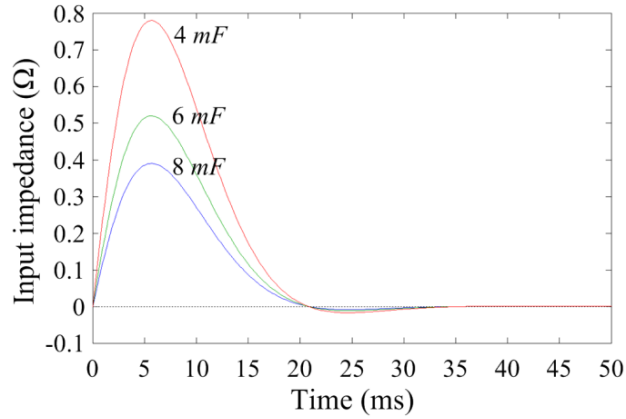Simulations have been performed to verify the analyses and design methods presented in the previous subchapters. Design specifications and designed parameters for the simulation are summarized in Table 3.2. The filter inductance is designed for each modular converter to have the current ripple whose peak-to-peak amplitude is twice as big as its nominal output current at the rated power. The input capacitance is designed to restrict the maximum voltage overshoot under 10% of its nominal input voltage when the input current changes from 0 to the rated current in a step manner. Finally, the output filter capacitance is designed to restrict the voltage ripple under 5% of the nominal output voltage.

Table 3.2. Design Specifications and Parameters for Simulation

Design Specifications	
Overall Rated Power	5 MVA
Input Voltage	5 kV
Output Voltage	50 kV
Switching Frequency	1 kHz
Number of Parallel Converters (N)	3
System Delay (T_d)	1.5 ms
Designed Parameters	
Transformer Turn-ratio (n)	11.63
Filter Inductance for each (L_{filter})	419.82 μH
Input Capacitance (C_{in})	6 mF
Output Capacitance (C_o)	0.472 μF
Proportional Gain (K_p)	1.66
Integral Gain (K_i)	189.56

Fig. 3.18 shows the input, inductor, and output current waveforms of the 3-paralleled SAB converter at its rated power. The peak input current to each modular converter is 776 *A* and the peak value of the total input current is 1492 *A*. Likewise, the peak output current from each modular converter is 67 *A*, the peak value of the total output current is restricted to 128 *A*,

55

and the magnitude of the peak-to-peak ripple current is measured to be 56 *A*, which is 23% of the peak-to-peak ripple current for a single high-power converter as expected.
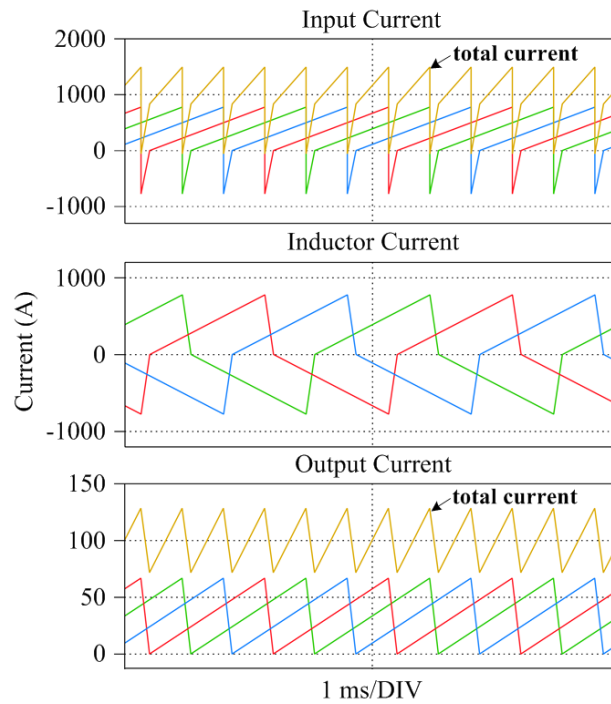
Fig. 3.18. Input, inductor, and output current waveforms of the 3-paralleled SAB converter at the rated power.

Fig. 3.19 shows the dynamic response of the system at the worst case scenario, where a disturbance current changes from 0 to its rated current, in this case, 1000 *A*, in a step manner. According to the simulation results, the maximum voltage overshoot of the input capacitor is well restricted to 455 *V*, which is under 10% of its nominal input voltage as designed. During the transient, both the input and output currents of the converter reach their maximum peak values of 2200 *A* and 189 *A*, respectively. It is also worth pointing out that both the input and output currents start to increase around 2 *ms* after the step change of the disturbance, due to the system delay. However, the overall system reaches steady-state again within 30 *ms* as expected.
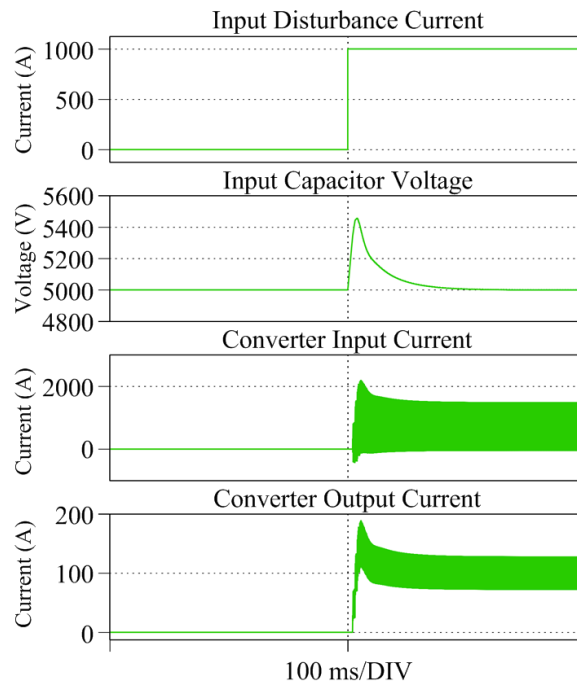
Fig. 3.19. Dynamic response of the system when the disturbance current changes from 0 to 1000 A.

3.3.3.6 Experiments

A small-scaled prototype for laboratory experiment has been built as shown in Fig. 3.20 and its design specifications and designed parameters are summarized in Table 3.3. The filter inductance and input capacitance are designed under the same condition as the simulation. However, the output filter capacitance is designed to be much bigger because the parallel converter's output side is directly connected to a grid connected inverter, which acts as a load. This grid connected inverter is responsible for sending the power back into the grid and keeping the dc-link voltage as constant as possible. Hence, to get rid of the effects of the switching and the dynamics of the dc-link voltage control from the grid-connected inverter, a bigger output filter capacitance has been chosen.

Fig. 3.20. Small-scaled prototype of the 3-Paralleled SAB dc-dc converter for laboratory experiment.

Table 3.3. Design Specifications and Parameters for Experiment

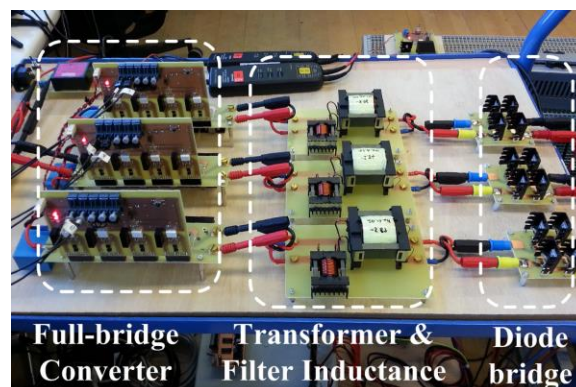| Design Specifications	
Overall Rated Power	1 kVA
Input Voltage	120 V
Output Voltage	600 V
Switching Frequency	10 kHz
Number of Parallel Converters (N)	3
System Delay (T_d)	150 μs
Designed Parameters	
Transformer Turn-ratio (n)	5.82
Filter Inductance for each (L_{filter})	121 μH
Input Capacitance (C_{in})	220 μF
Output Capacitance (C_o)	500 μF
Proportional Gain (K_p)	0.61
Integral Gain (K_i)	695.07

Figs. 3.21 (a), (b) and (c) show the output current waveforms under the steady-state with various duty-ratios. In each figure, the three lower waveforms are the phase shifted output currents from the 3-parallel converter and the upper waveform represents the total output current. Although the total output current is still in the DCM at a low duty-ratio (Fig.16 (a)), the magnitudes of the output peak and ripple currents are significantly reduced and the ripple frequency is increased by 3 times. At higher duty-ratios (Fig.16 (b), (c)), the total output current is in the CCM. The average output currents are measured to be 0.08 A, 0.69 A, and 1.64 A, respectively, and they have a nonlinear relationship with the duty-ratio as expected.

To perform the dynamic analysis, an ideal current source, which is controllable, is required to provide a step input current to the system. However, due to the constraints of available equipment in the laboratory, an additional circuit in combination with a dc power supplier has been implemented as shown in Fig. 3.22. The dc power supplier is set to operate in a constant current mode and to provide the rated input current to the dc-dc converter. The resistor value is chosen to draw the entire input current at the controlled voltage of 120V when the resistor is connected to the circuit through the IGBT switch. When the switch disconnects the resistor from the circuit, the current through the resistor changes its path to the input of the dc-dc converter. The IGBT is used to achieve fast switching and to avoid unwanted noises from a mechanical switch. An additional diode is installed in parallel with the resistor to provide a freewheeling path for the current flowing in the parasitic inductance of the high-power coil resistor. This prevents an unwanted voltage spike in the IGBT switch when it turns off and, in turn, in the input voltage of the dc-dc converter. Therefore the rise time of the input current to the dc-dc converter is solely dependent upon the turn-off time of the IGBT used.
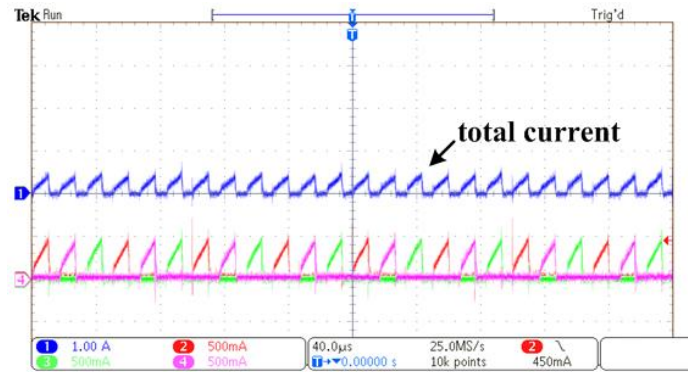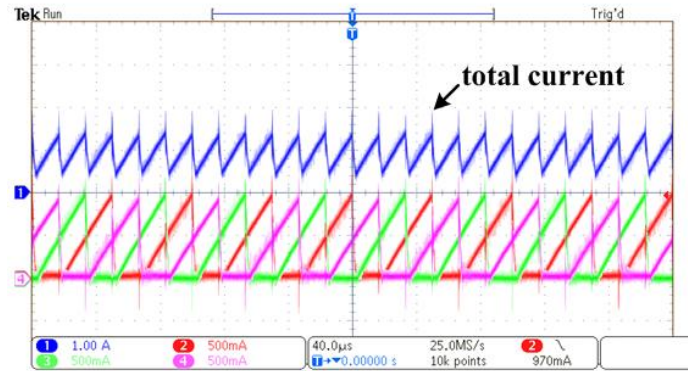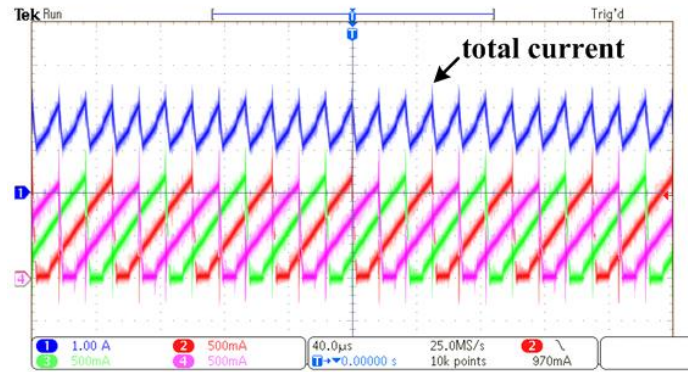
Fig. 3.21. Output current waveforms under the steady-state depending on duty-ratio (D); (a) 0.1, (b) 0.3, and (c) 0.465.

Fig. 3.22. Step current supplying circuit.

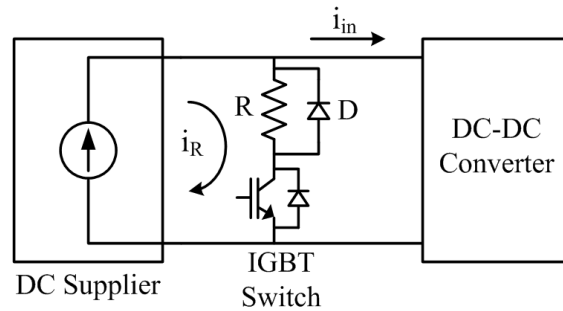Fig. 3.23 shows the dynamic characteristics of the dc-dc converter when the input current is changed from 0 to its rated value of 8.33 *A* in a step manner. The maximum overshoot is measured to be 11 *V*, which is 9.2 % of the nominal voltage. This value is a little bit smaller than the designed value of 12 V, because the input step current is not perfectly ideal. However, this experimental result is good enough to verify the dynamic performance of the dc-dc converter and its input voltage control method. The overall system reaches its steady-state again within 3 *ms*.
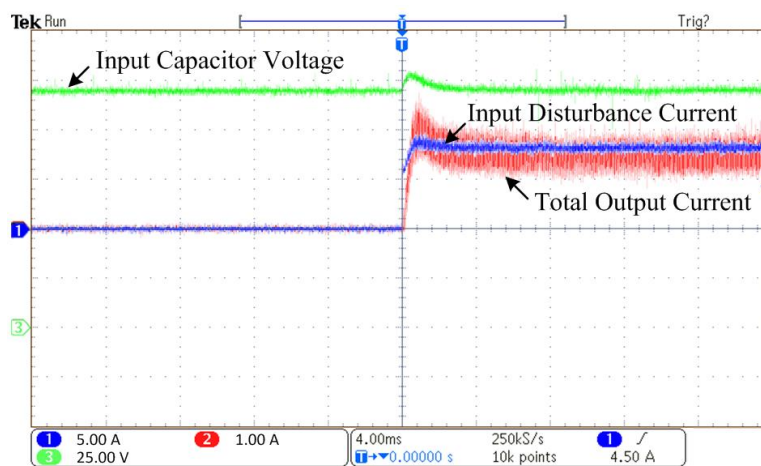
Fig. 3.23. Dynamic response of the system when the disturbance current changes from 0 to 8.33 A.

3.3.4 Reliable Operation of the PCSAB Converter

The reliability has been one of the fast-growing topics in the field of the power conversion systems and much research has been conducted on fault detection and fault-tolerant control of the switching devices in the power conversion systems [25, 26]. There are two different types of the switching device faults: short-circuit fault and open-circuit fault. The short-circuit fault is usually caused by wrong gating signals, overvoltage, or high temperature. Since the short-circuit fault could cause additional damage to other components in the circuit, it should be treated quickly and carefully. Therefore, the fault detection and fault-tolerant control methods for the short-circuit fault are usually based on hardware implementation [26]. Meanwhile, the open-circuit fault is usually due to lifting of the bonding wires in a switch module caused by over-temperature or aging. The open-circuit fault might result in unwanted current distortion, noise, and/or vibration, but it usually does not cause additional serious damage to the system. Hence, the open-circuit fault could be easily dealt with converter switching control to ensure the fault-tolerant operation.

In this subchapter, a new open-circuit fault detection and fault-tolerant control strategy for the PCSAB dc-dc converter will be proposed. Two different types of the open-circuit fault will be defined first, and analysis of the converter under each fault condition will be presented. The proposed fault detection method identifies the location and type of a fault with one current sensor in the output. The proposed fault-tolerant control method uses different approaches to improve the performance of the converter under the fault condition depending on its type of the fault. The feasibility of the proposed fault-detection and fault-tolerant method will be verified by simulations and experiments.

3.3.4.1 *Analysis of the PCSAB Converter under Open-Circuit Faults*

Two different kinds of the open-circuit faults within a modular converter are considered in this thesis. First, Type-1 is defined as when the open-circuit fault occurs only in one of the switching devices or in two switching devices in a special way: the fault occurs in 'positive-switch pair' (S_1 and S_4), or 'negative-switch pair' (S_2 and S_3) at the same time. Therefore, the Type-1 open-circuit faults can be summarized as shown in Fig. 3.24. On the other hand, Type-2 is defined as when the fault occurs in more than two switching devices at the same time. Note that it is assumed that the antiparallel diode within a switch module is not affected by the open-circuit fault and provides a current freewheeling path even under the fault conditions.
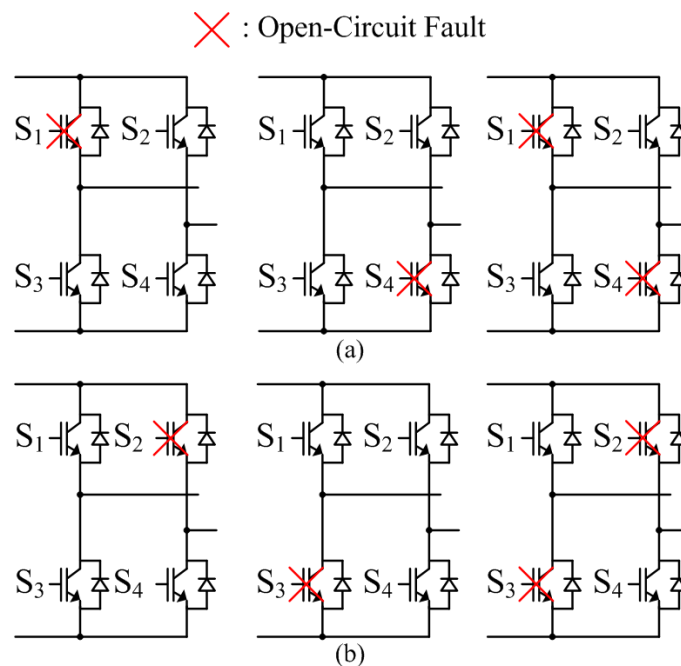

Fig. 3.24. Type-1 open-circuit faults in (a) the positive switch pair (S_1 and S_4) and (b) the negative switch pair (S_2 and S_3).

The modular converters have different performance depending on their fault types. If the Type-1 fault occurs, the modular SAB converter still can operate with half power capacity as shown Fig. 3.25. In the case of open-circuit fault in the positive-switch pair, the positive dc input voltage, V_{dc}, cannot be applied to the input terminals of the transformer. Hence, a positive current cannot be built in the transformer and, in turn, power cannot be transferred to the secondary side. However, the negative dc input voltage, $-V_{dc}$, still can be applied to the transformer by turning on the negative-switch pair. Since the antiparallel diodes in the positive switch pair are assumed to be intact, there is a normal freewheeling current path when the negative-switch pair is turned off. Therefore, power can be transferred to the secondary side without any problem. Similarly, when the open-circuit fault occurs in one or both switches in the negative-switch pair and its antiparallel diodes are intact, power still can be transferred to the secondary side using the positive dc input voltage. Since the current in the secondary side of the transformer is rectified, the Type-1 fault leads to a missing output current pulse in every other output ripple. This decreases the effective ripple frequency of the output current and the power transferred to secondary side by half. In the case of the Type-2 open-circuit fault, the whole modular SAB converter loses its ability to transfer power to the secondary side.
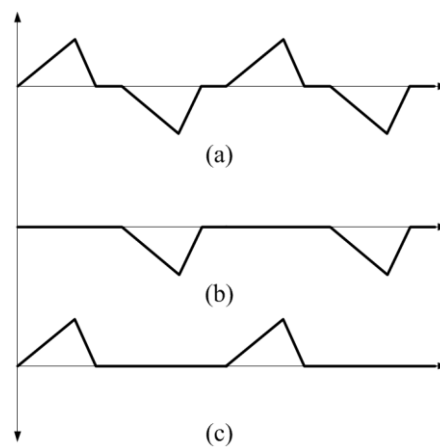
Fig. 3.25. Current waveforms in the filter inductor or the transformer (a) under a normal condition, and when the Type-1 fault occurs (b) in the positive switch pair and (c) the negative switch pair.

Considering an *N*-parallel-connected SAB converter, the Type-1 open-circuit fault leads to loss of *1/(2N)* of the overall power rating and distortion in the output current. The Type-2 open-circuit fault leads to loss of *1/N* of the overall power rating and even more distortion in the output current. Fig. 3.26 shows the input current, the filter inductor current, and the output current of a 3-parallel-connected SAB converter under the Type-1 and Type-2 open-circuit fault conditions, respectively.
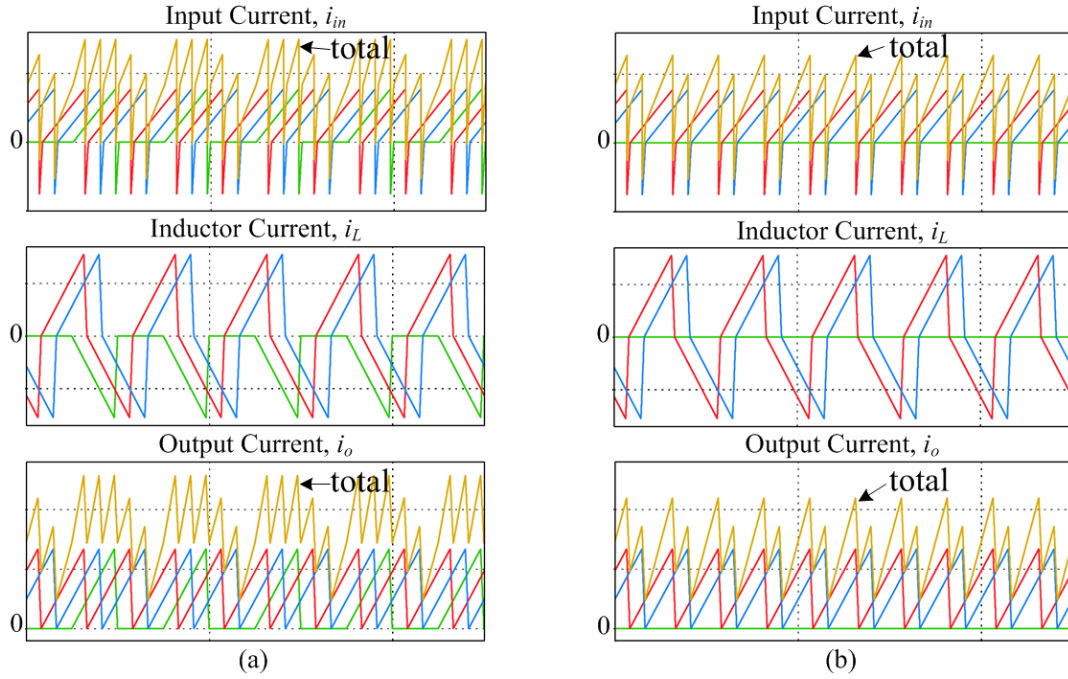
Fig. 3.26. Current waveforms of a 3-parallel-connected SAB converter under the (a) Type-1 and (b) Type-2 open-circuit fault conditions.

3.3.4.2 Open-Circuit Fault Detection Method

To perform any fault-tolerant operation, the location and the type of the fault should be identified first. The easiest way to locate a fault in an *N*-parallel converter is to measure each filter inductor current in every modular converter separately. By observing the shape of each current waveform, the location and the type of the fault can be easily determined. For example, if the positive current pulse is missing from the waveform of a certain modular converter, the open-circuit fault has occurred in either one of S_1 and S_4 (positive-switch pair) or both. On the other hand, if the negative pulse is missing, the open-circuit fault has occurred in either one of S_2 and S_3 (negative-switch pair) or both. Further identification of the exact faulty switch within the switch pair is not necessary since it does not affect the fault-tolerance operation, which will be introduced in the following subchapter. Finally, if zero inductor current is measured all through a switching period even with a non-zero duty-ratio, one can easily conclude that the Type-2 fault has occurred in that modular converter. Again, the further identification of the exact faulty switch within the modular converter is not necessary.

In this thesis, a fault detection method which utilizes only one current sensor in the output is introduced. When an open-circuit fault occurs, the output current is distorted as shown in the previous analysis. By measuring the output current, sufficient information for the fault-tolerant operation can be obtained. To extract valuable information from the total output current which contains high frequency ripples, the current sensor needs to measure the

output current at the instant when each pair of switches is turned off. This is the same instant when the output current of each modular converter reaches its peak value. By tracing the measured current values for each pair of switches in every modular converter separately and by comparing these values between one another, the location and type of the fault can be determined. Owing to the nature of the DCM and depending on the location and instant of the fault, the proposed fault detection method takes no more than two switching periods or even less than one switching period to identify the location and type of the fault.

To facilitate the understating of the proposed fault detection method, the current measuring instants and the measured currents of the 3-parallel-connected SAB converter under normal, Type-1 fault, and Type-2 fault conditions are demonstrated in Fig. 3.27. It should be noted that the measured value for each pair of switches is updated at the same rate of the switching frequency. Therefore, in one switching period, the output currents of all the switch pairs should be measured and compared. As it can be seen from Fig. 3.27(a), when the parallel converter is operating in the normal condition, all the measured currents have the same value. In the case of the Type-1 fault, the switch pair which contains the faulty switch has the lowest measured current value. In Fig. 3.27(b), the switch pair of S_1 and S_4 in the module '2' contains a Type-1 faulty switch. In the case of the Type-2 fault, both the switch pairs in the same module which contains faulty switches have the lowest measured current value. In Fig. 3.27(c), a Type-2 fault has occurred in the module '2'. It is worth noting here that, whenever the measured values are compared between one another to identify the fault condition, it is always recommended to introduce a reasonable threshold value (or a hysteresis band) to avoid false alarms from the system noise or fast transients.
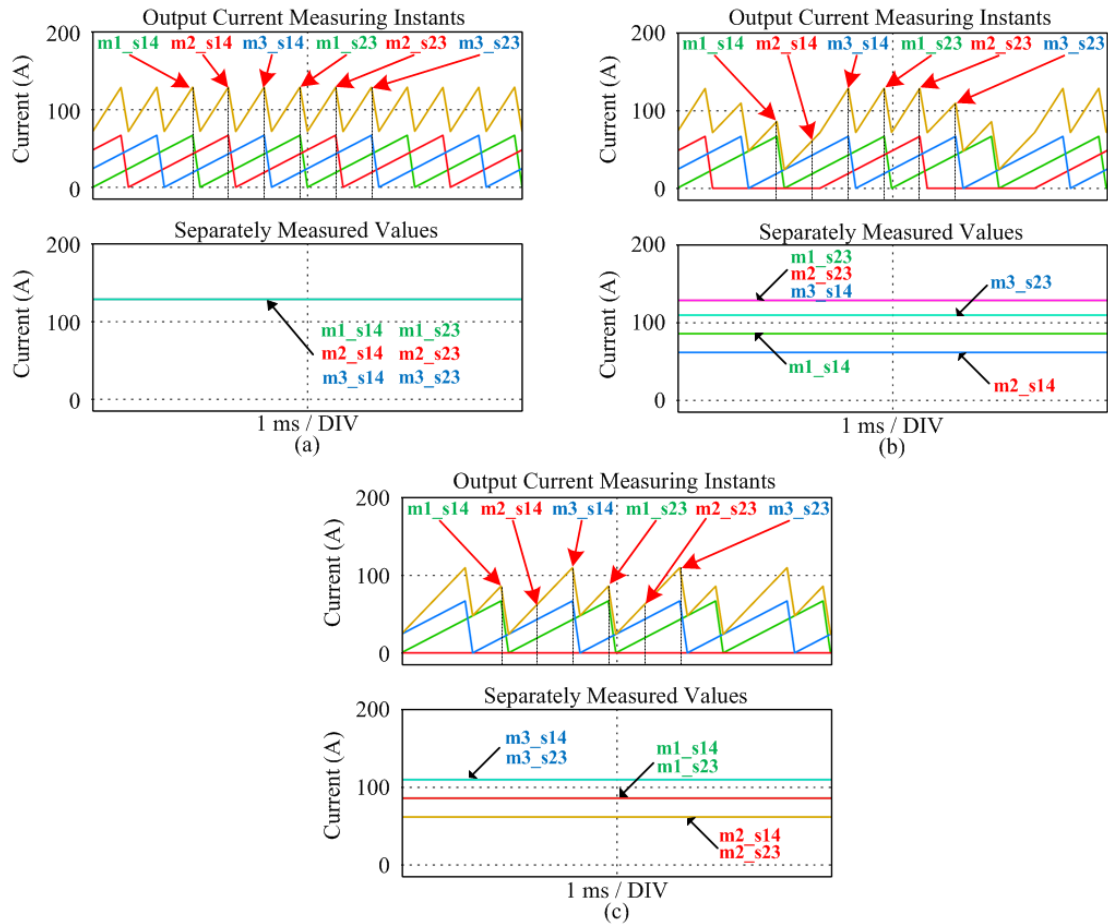
Fig. 3.27. The current measuring instants and the measured currents under (a) normal, (b) Type-1 fault, and (c) Type-2 fault conditions; where mx (x=1, 2, 3) indicates a modular converter, and s14 and s23 indicate the positive and negative switch pairs, respectively, within the modular converter.

3.3.4.3 Fault-Tolerant Operation

Since the location and type of the open-circuit fault has been identified through the diagnosis method presented in the previous subchapter, the proposed fault-tolerant control strategy can be applied to improve the performance of the converter under the fault conditions. The fault-tolerant control strategy varies depending on its type of the fault.

(1) Type-1 Fault

In the case of the Type-1 open-circuit fault, it was already analyzed in the previous subchapters that only half of the power transferring capability is lost in the faulty modular converter because the intact switch pair and the antiparallel diodes in the impaired switch pair still can operate. However, thanks to the discontinuous conduction characteristic of the SAB converter, the converter can be controlled to transfer the full rated power to the secondary side even under the fault condition.

Since the output current is rectified through the diode bridge in the secondary side of the transformer, the Type-1 fault causes a missing pulse in every other output current ripple as shown in Fig. 3.25. Therefore, if the intact switch pair switches again in place of the impaired switch pair, the identical output current without any distortion can be achieved. In other words, the intact switches should continue switching to make the inductor current flow as shown Fig. 3.28. To make the proposed fault-tolerant control possible, it should be first assumed that the switches in the converter are capable to operate at twice as fast switching frequency. Furthermore, the increased switching and conduction losses due to the increased switching frequency should be properly considered in the thermal design of the converter and the transformer also have to be designed by taking the unipolar operation into account. It is true that the converter cannot be designed to transfer the full rated power under the fault condition. This will lead to overdesign of the entire converter. However, this fault-tolerant control method can be effectively utilized under some power limits.
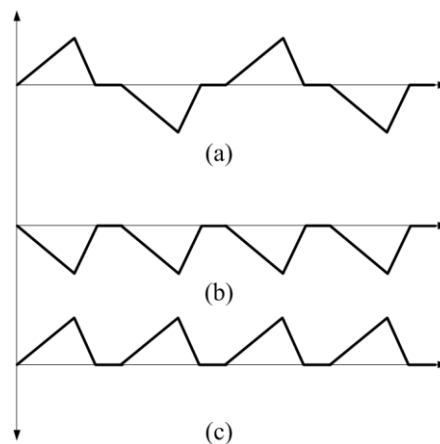
Fig. 3.28. Fault-tolerant current waveforms in the filter inductor or the transformer (a) under a normal condition, and when the Type-1 fault occurs (b) in the positive switch pair and (c) the negative switch pair.

(2) Type-2 Fault

In the case of the Type-2 open-circuit fault, it was analyzed in the previous subchapter that a modular SAB converter loses its entire ability to transfer power to the secondary side because there is no alternative way to energize the transformer. Therefore, when the Type-2 fault occurs, the entire modular converter which contains the faulty switches has to be shut down. However, although the loss of power capacity is unavoidable, the quality of the output current of the *N*-parallel interleaved converter can still be improved by adjusting the phase shift angle among the intact modular converters. In other words, when the Type-2

66

fault occurs, the phase shift angle changes from $\pi/(2 \cdot N)$ to $\pi/(2 \cdot (N-1))$ and only the intact modular converters interleave their output currents with this new angle.

3.3.4.4 Simulations and Experiments

Simulations and experiments have been carried out to verify the validity and effectiveness of the proposed fault detection and fault-tolerant control methods. A 5 MW 3-parallel-connected SAB converter is used for the simulation and the 1 kW small-scaled prototype is used for the experiment. Design specification and parameters are the same as Table 3.2 for the simulation and Table 3.3 for the experiment. For the sake of simplicity, fault identification numbers are defined to indicate the location and type of a fault as shown in Table 3.4.

Table 3.4 Fault Identification Numbers

Fault #	Module	Location (switch pair)	Type
1	1	Positive	Type-1
2	1	Negative	Type-1
3	2	Positive	Type-1
4	2	Negative	Type-1
5	3	Positive	Type-1
6	3	Negative	Type-1
7	1	-	Type-2
8	2	-	Type-2
9	3	-	Type-2

Fig. 3.29 shows the simulation result when the type-1 open-circuit fault has occurred in the positive switch pair of the module '2' at 200 ms. The converter was operating at its rated power before the fault. As it can be seen from the inductor current, the positive current of the module '2' is missing after 200 ms. The fault is detected in one switching period and the identification number is measured to be 3, which means the Type-1 fault has occurred in the positive switch pair of the module '2'. Right after detecting the fault, the fault-tolerant operation has taken place. The negative switch pair in the module '2' starts to operate at twice as fast switching frequency to compensate the missing positive pulse. As a consequence, the shapes of both the input and output current are restored to the ones before the fault.

Fig. 3.29. The simulation result when the Type-1 open-circuit fault has occurred at 200 ms.

Fig. 3.30 shows the experimental result when the type-1 open-circuit fault has occurred in the positive switch pair in one of the modular converters at a certain instance. The converter was operating with 0.28 duty-ratio before the fault. As it can be seen, the type-1 fault is detected within one switching period, which is 100 µs, and the fault-tolerant operation has taken place immediately after the detection. The negative switch pair starts to operate at twice faster switching frequency to compensate the missing positive pulse and, in turn, the shape of the output current is restored very close to its original shape but with some distortion. As it can be seen from the figure, the shape of inductor current pulses during the tolerant operation is slightly different from the one during the normal operation. It is due to the unidirectional core excitation of the transformer during the tolerant operation. However, even though the restored output current is a bit distorted, its average value is perfectly restored.

Fig. 3.30. The experimental result when the Type-1 open-circuit fault has occurred.

68

Fig. 3.31 shows the simulation result when the type-2 open-circuit fault has occurred in the module '2' at 200 ms. The converter was operating at its rated power before the fault. As it can be seen from the inductor current, the module '2' has lost its entire ability to transfer power after the fault. The fault is detected in one switching period and the identification number is measured to be 8, which means the type-2 fault has occurred in the module '2'. Right after the fault detection, the fault-tolerant operation has taken place again. The converter keeps operating with the old phase shift angle ($\pi/3$) until the ongoing switching cycle completes. Then, the converter starts switching with a new phase shift angle ($\pi/2$) to reduce the ripple size of the output current.
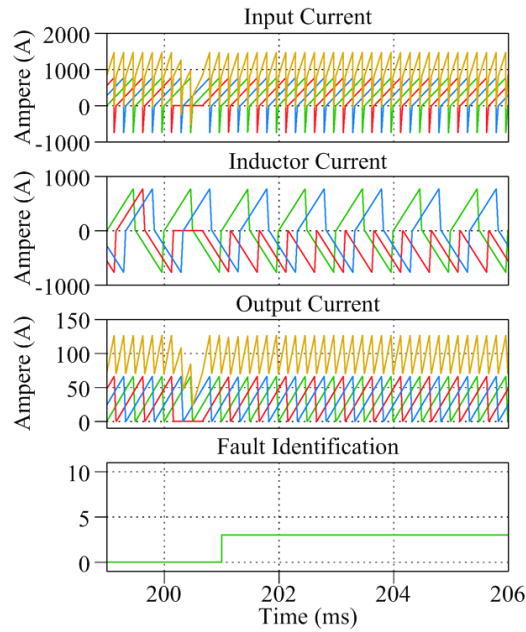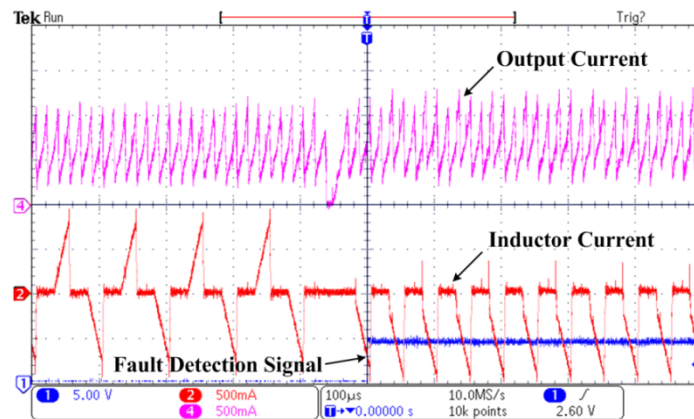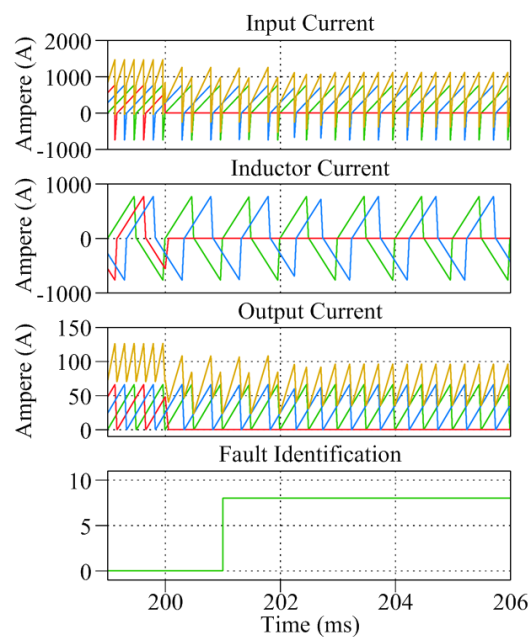

Fig. 3.31. The simulation result when the Type-2 open-circuit fault has occurred at 200 ms.

Fig. 3.32 shows the experimental result when the type-2 open-circuit fault has occurred in one of the modular converters at a certain instance. The converter was operating with 0.28 duty-ratio before the fault. As it can be seen from the inductor current, the modular converter has lost its entire ability to transfer power after the fault. The type-2 fault is detected in one switching period, and right after the detection, the fault-tolerant operation has taken place again. Identical to the simulation result, the converter keeps operating with the old phase shift angle ($\pi/3$) until the ongoing switching cycle completes. Then, the converter starts switching with a new phase shift angle ($\pi/2$) to reduce the ripple size of the output current. Therefore, it only takes 2 switching periods (200 μs) in total for both the fault detection and the full application of the tolerance operation.
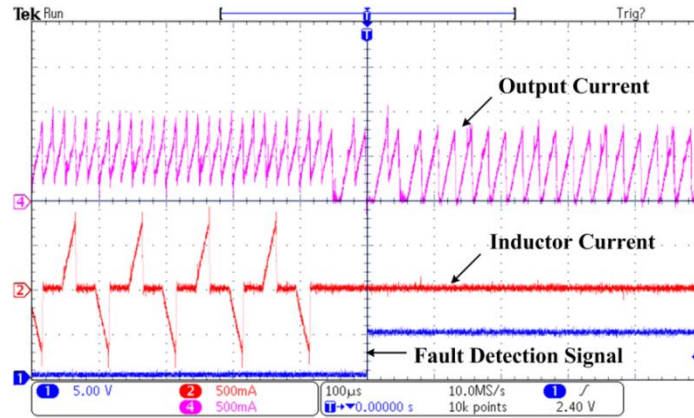
69

Fig. 3.32. The experimental result when the Type-2 open-circuit fault has occurred.

3.4 Double Uneven Power Converter based DC-DC Converter

In this subchapter, a novel Double Uneven Power (DUP) converter based dc-dc converter and its design and control methods will be introduced. The proposed converter utilizes two full-bridge converters in a special way to realize the Zero-Current-Switching (ZCS), where both the turn-on and turn-off switching occur under the zero-current condition. The proposed DUP converter is designed for high power (MW-levels) applications, where the voltage transformation is required. The main objectives of the proposed converter are (1) to reduce the switching power losses in the power semiconductor devices and (2) to reduce the output filter inductance. The proposed converter is expected to be highly beneficial for high-power applications, such as dc-transmission grid or dc-collection systems in offshore wind farms.

3.4.1 Double Uneven Power (DUP) Converter

3.4.1.1 Circuit Configuration

The proposed structure has two full-bridge converters with different power ratings as shown in Fig. 3.33. The 'main' converter processes the majority of power (80~90%) with ZCS and the 'control' converter delivers a small share of power (10~20%) with hard-switching. The proposed DUP converter has two unidirectional full-bridge converters, connected in parallel at the input side and in series at the output side. Since the input sides of the full-bridge converters are connected in parallel, the voltage ratings of the power switches (e.g. IGBT) are the same for both the converters. However, the power switches of the 'main' converter require much larger current ratings than that of the 'control' converter since the 'main' converter needs to process much larger power. On the contrary, since the output sides

70

of the converters are connected in series, both the diode bridges should have the same current rating, but larger voltage rating is required for the diode bridge of the 'main' converter.
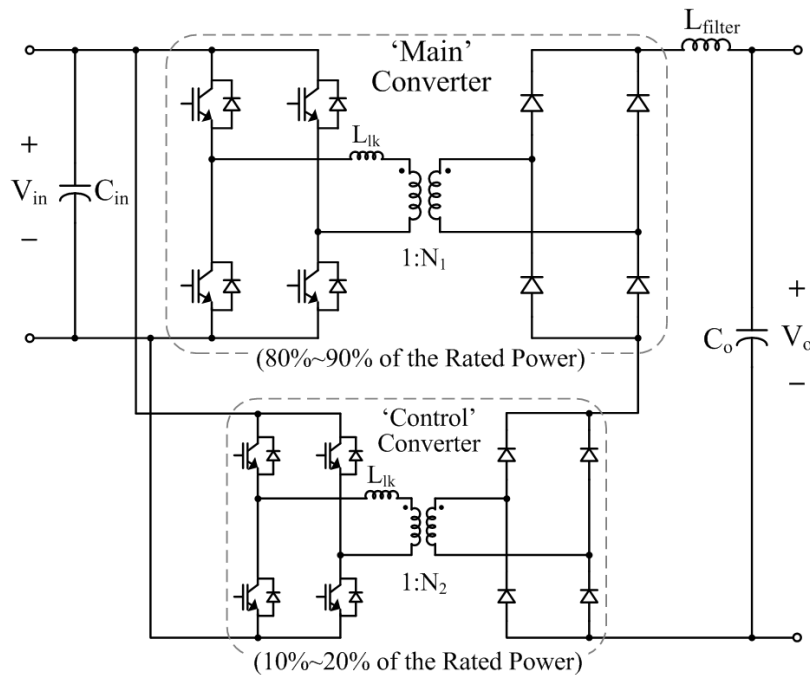
Fig. 3.33. The proposed Double Uneven Power (DUP) converter based dc-dc converter.

The transformer turn-ratio of the 'main' converter, N_1, is designed to be larger than that of the 'control' converter, N_2, so that the 'main' converter performs the majority of the required voltage transformation. Meanwhile, N_2 is generally designed to be a much smaller value, so that the 'control' converter can provide the voltage which is just enough to control the overall power delivery of the system. The detailed design method for the transformer turn-ratios will be presented in the later subchapters.

3.4.1.2 Fundamental Operation

The 'main' converter needs to amplify the input voltage (V_{in}) to the voltage level close to the output voltage (V_o) and to keep this value as constant as possible for a whole switching period. Therefore, the 'main' converter operates with its maximum duty-ratio (0.5) all the time. Since this converter operates with the fixed duty-ratio at a fixed switching frequency, the 'main' converter does not require any further control.

Meanwhile, the 'control' converter controls the overall power flow of the entire converter system by varying its duty-ratio. For the 'control' converter, either duty-cycle control (hard-switching) or phase-shift control (soft-switching) might be used. However, since the 'control' converter operates in the DCM, the soft-switching can be achieved only in

the lagging leg of the full-bridge converter. In addition, the soft-switching would increase the conduction losses. Therefore, the duty-cycle control is adopted here.

Fig. 3.34 shows the switching signals for the 'main' and 'control' converters and the various current waveforms. The figure also shows the switching states and their corresponding current conduction paths.
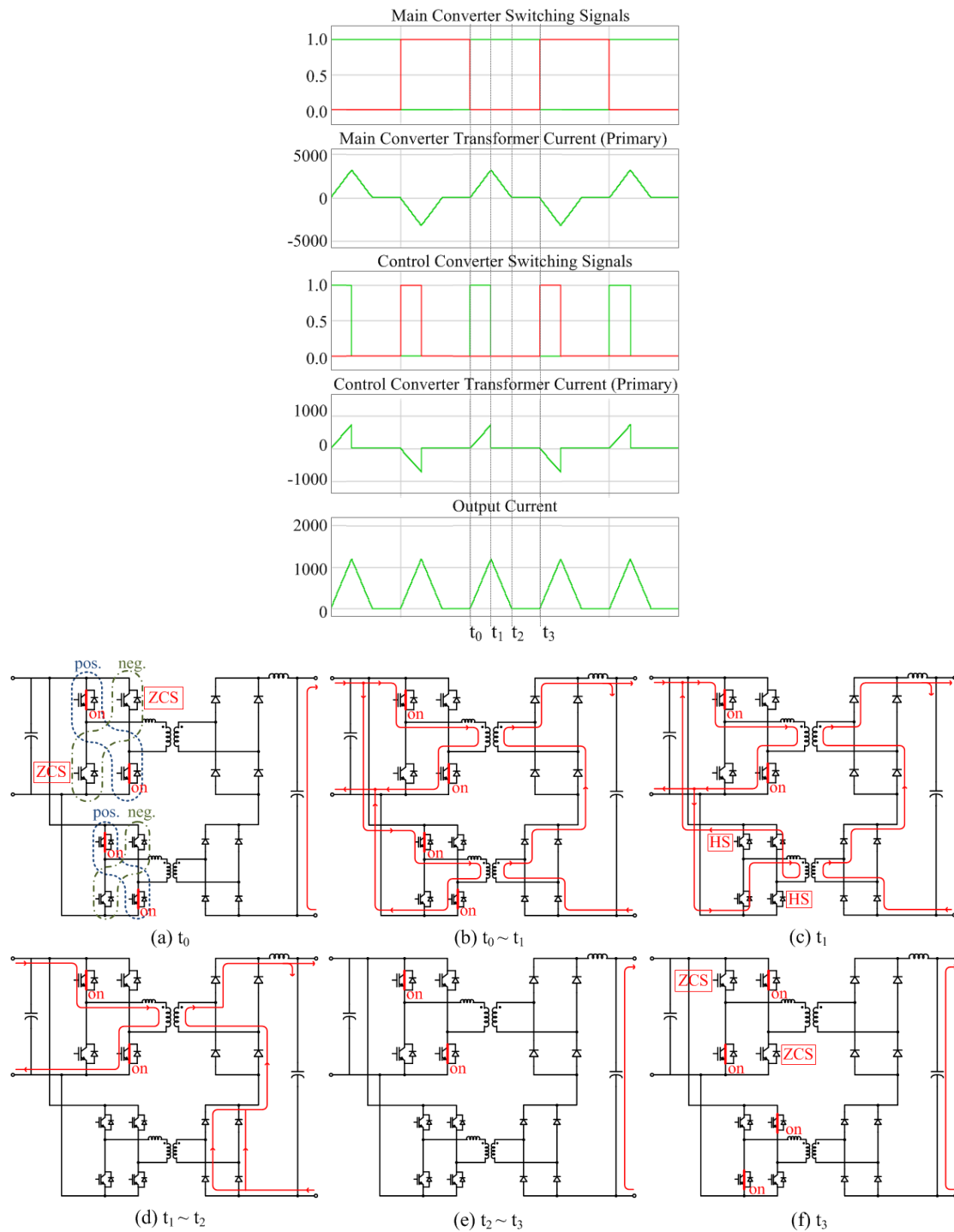

Fig. 3.34. Typical current waveforms and current conduction paths depending on the switching states.

72

(1) t_0: t_0 is the instant when a new switching period starts by turning off the negative switch pair in the 'main' converter and turning on the positive switch pairs in both the 'main' and 'control' converters as shown in Fig. 3.34(a). As it can be seen from the current waveforms, there was no current flowing in the primary and secondary sides of both the transformers prior to t_0. Therefore, the negative switch pair in the 'main' converter is turned off under the ZCS condition and, in turn, there is no turn-off switching loss.

(2) $t_0 \sim t_1$: During this interval, the secondary-side currents in both the converters and the output current, which is identical to the current in the output filter inductor, increase linearly. The rate of the output current change (di_o/dt) is determined by the input and output voltages, the output filter inductance (including the leakage inductances of the transformers), and the transformer turn-ratios. The output filter inductance and the transformer turn-ratios should be designed to limit the peak value of the output current and to make the output current waveform as an isosceles triangle waveform.

(3) t_1: t_1 is the instant when the positive switch pair in the 'control' converter is turned off under hard-switching condition. However, since the power processed by the 'control' converter itself is only a small portion of the overall power of the converter system, the turn-off switching loss in the 'control' converter is not significant. As it can be seen from the figure, there is a regenerative current flowing through the antiparallel diodes of the negative switch pair for a short time period right after turning off the positive switch pair in the 'control' converter. This current is due to the leakage inductance of the transformer in the 'control' converter.

(4) $t_1 \sim t_2$: After the regenerative current vanishes, there is no current flowing in the primary side of the 'control' converter. The output current is now flowing directly through both the legs of the diode bridge in the 'control' converter as shown in Fig. 3.34(d). The output current and the current in the 'main' converter decrease linearly during this period and reaches zero before the next half switching period starts at t_3.

(5) $t_2 \sim t_3$: During this interval, even though the positive switch pair in the 'main' converter still remains turned on, there is no current flowing in both the converters as shown in Fig. 3.34(e).

(6) t_3: t_3 is the instant when a new half switching period starts by turning off the positive switch pair in the 'main' converter and turning on the negative switch pairs in both the 'main' and 'control' converters as shown in Fig. 3.34(f). Since there was no current flowing in the 'main' converter before the positive switch pair is turned off, the ZCS is

achieved. The rest of the switching period is symmetrical to the previous half switching period as explained so far.

It is also worth noting here that both the converters turn their switches on only when the currents are zero. Furthermore, the rates of the current increase (*di/dt*) are restricted by the output filter inductance. This reduces turn-on switching losses substantially for both the converters.

3.4.1.3 Equivalent Circuits

To facilitate the understanding of the operational principle of the proposed converter, equivalent circuits can be utilized as shown in Fig. 3.35. If the 'main' converter is referenced to the secondary side of the transformer, then it can be modelled with a single switch, a single diode, and a voltage source ($N_1 \cdot V_{in}$) as shown in Fig. 3.35(a). The output voltage of the equivalent circuit is $(2 \cdot D_{main})(N_1 \cdot V_{in})$, where D_{main} is the duty-ratio of the 'main' converter. Since the 'main' converter operates with the full duty-ratio (0.5), the equivalent circuit can be further simplified as a single voltage source with the value of $N_1 \cdot V_{in}$ and connected to the output filter inductor in series as shown in Fig. 3.35(b). Likewise, The 'control' converter can be modelled in the same way and the output voltage of the equivalent circuit is $(2 \cdot D_{ctrl})(N_2 \cdot V_{in})$, where D_{ctrl} is the duty-ratio of the 'control' converter. However, the 'control' converter has to operate with the duty-ratio from 0 to 0.25 to ensure the ZCS of the 'main' converter, as will be explained in the next subchapter.
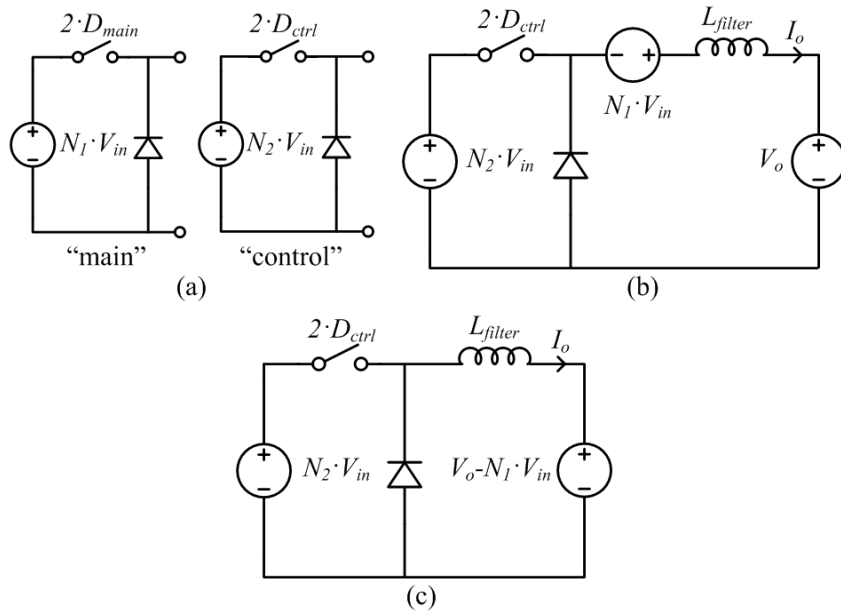

Fig. 3.35. Equivalent circuits; (a) 'main' and 'control' converters, respectively, (b) the overall DUP converter with the output filter inductor, and (c) the further simplified DUP converter.

74

The equivalent circuit can be further simplified into Fig. 3.35(c), which is a typical step-down (buck) converter. Since both the input and output voltages are assumed to be constant during one switching period, the average current in the output filter inductor, in turn, the average power delivered can be controlled by varying the duty-ratio of the 'control' converter, D_{ctrl}. If the output current waveform in the filter inductor is ensured to be an isosceles triangle using the design method explained in the next subchapter, the average output current can be expressed as below.

$$I_o = \frac{2 \cdot T_s}{L_{filter}} ((N_1 + N_2)V_{in} - V_o) \cdot D_{ctrl}^2 \quad , \tag{3.35}$$

where T_s is the switching period. Since both the input and output voltages are the given values (system specifications), the main design parameters are transformer ratios (N_1 and N_2) and the output filter inductance (L_{filter}).

3.4.1.4 Main Design Parameters (N_1, N_2, and L_{filter})

The distribution of the delivering power between the 'main' and 'control' converters can be determined by the transformer turn-ratio of the 'control' converter (N_2). Depending on N_2, the transformer turn-ratio of the 'main' converter (N_1) can be determined in such a way that the output current waveform becomes an isosceles triangle; this means the current rise time ($t_0 \sim t_1$) and the current fall time ($t_1 \sim t_2$) in the output filter inductor are always kept the same as shown in Fig. 3.34. In this way, the least amount of the output filter inductance is ensured at a given peak output current rating.

The amounts of the current rise ($|i_r|$) and the current fall ($|i_f|$) in the output filter inductor can be expressed as

$$\begin{aligned} |i_r| &= \frac{(N_1 + N_2) \cdot V_{in} - V_o}{L_{filter}} \cdot t_r \\ |i_f| &= \frac{V_o - N_1 \cdot V_{in}}{L_{filter}} \cdot t_f \end{aligned} \quad , \tag{3.36}$$

where t_r and t_f is the current rise time and the current fall time, respectively.

Since $|i_r|$ and $|i_f|$ are the same under the steady-state, the following relationship can be achieved by equating the current rise time to the current fall time in the output filter inductor.

$$N_1 \cdot V_{in} + \frac{N_2 \cdot V_{in}}{2} = V_o \tag{3.37}$$

75

In other words, N_1 and N_2 should be designed in such a way that the sum of the average output voltages from the 'main' and 'control' converters (at their maximum duty-ratios, 0.5 and 0.25, respectively) should be the same as the average output voltage of the overall converter (V_o). For example, if the input voltage (V_{in}) is 50 kV and the output voltage (V_o) is 150 kV, the relationship between N_1 and N_2 satisfying (3.37) is shown in Fig. 3.36. Since the 'control' converter is designed to process only a small portion of the overall power, N_2 should be chosen as small as possible. In this way, the output current waveform is ensured to be an isosceles triangle.
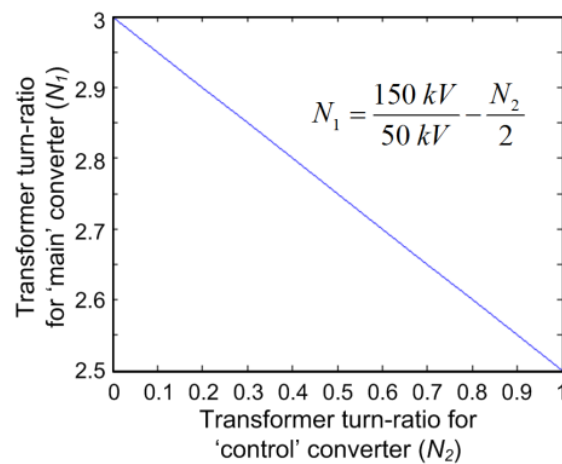
Fig. 3.36. Design example of the transformer turn-ratios (N_1 and N_2), when the input and output voltages are 50 kV and 150 kV, respectively.

The power distribution between the 'main' and 'control' converters is also determined by N_2. When the switches in the 'control' converter are turned on, the secondary-side currents of both the converters are identical to the output current, i_o, as shown in Fig. 3.34(b). Hence, the primary-side currents of the 'main' and 'control' converters (i_{main_p} and i_{ctrl_p}) during the current rise can be expressed as below, respectively.

$$i_{main\_p} = i_o \cdot N_1 = i_o (\frac{V_o}{V_{in}} - \frac{N_2}{2}),$$
$$i_{ctrl\_p} = i_o \cdot N_2$$

(3.38)

When the switches in the 'control' converter are turned off, the secondary-side current of the 'control' converter becomes 0 instantly, but the secondary-side current of the 'main' converter still flows until the output current reaches 0 as shown in Fig. 3.34(d). The duration of the current decrease is identical to that of the current increase because the waveform of the output current is kept as an isosceles triangle. Therefore, instantaneous currents in the primary sides during the current fall can be expressed as below.

$$i_{main\_p} = i_o \cdot N_1 = i_o(\frac{V_o}{V_{in}} - \frac{N_2}{2}), \tag{3.39}$$

$$i_{ctrl\_p} = 0$$

From (3.38) and (3.39), the average currents of the primary sides of both the converters (I_{main_p} and I_{ctrl_p}) for one switching period can be expressed as below.

$$I_{main\_p} = \frac{2}{T_s} \int_0^{2 \cdot D_{ctrl} \cdot T_s} i_o \cdot (\frac{V_o}{V_{in}} - \frac{N_2}{2}) dt,$$

$$I_{ctrl\_p} = \frac{2}{T_s} \int_0^{D_{ctrl} \cdot T_s} i_o \cdot N_2 \, dt \tag{3.40}$$

Since the average input voltage is the same for both the converters, the average power distribution ratio between the converters can be expressed as

$$P_{main} : P_{ctrl} = V_{in} \cdot I_{main\_p} : V_{in} \cdot I_{ctrl\_p}$$

$$= I_{main\_p} : I_{ctrl\_p} = 2\frac{V_o}{V_{in}} - N_2 : N_2. \tag{3.41}$$

For example, if the input voltage (V_{in}) is 50 kV and the output voltage (V_o) is 150 kV again, the average power distribution is shown in Fig. 3.37. If N_2 is designed to be 0.6 and N_1 is designed according to (3.37), which is 2.7, then the power will be distributed in a way that 90% of the total power is processed by the 'main' converter and 10% by the 'control' converter.
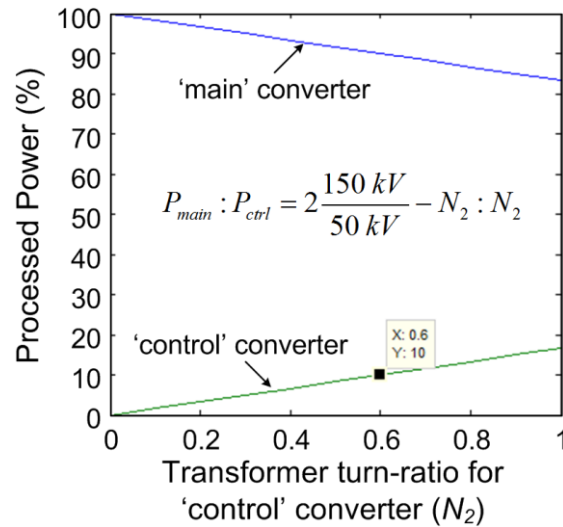

Fig. 3.37. Power distribution example when the input and output voltages are 50 kV and 150 kV, respectively.

It should be noted that N_2 should be designed depending on applications, and the input and output voltage conditions. The larger the variations in both the input and output voltages from their nominal values, the bigger N_2 should be to ensure the robust operation. However, if N_2 is increased, then more power will be processed by the 'control' converter and, in turn, the efficiency of the overall system can be lowered. Therefore, a system designer should decide N_2 by taking into account the trade-off between the robustness and the efficiency.

The output filter inductance (L_{filter}) can, now, be designed to limit the maximum peak value of the output current at the rated power. Since the output current has an isosceles triangular shape obeying (3.37), the maximum duty-ratio that the 'control' converter can have is 0.25 and this is also the boundary condition for the DCM. Therefore, the required filter inductance can be easily achieved using the following equation.

$$L_{filter} = \frac{(N_1 + N_2) \cdot V_{in} - V_o}{i_{peak}} \cdot \frac{T_s}{4} \tag{3.42}$$

where i_{peak} is the maximum peak current at the rated power. In this way, the output filter inductance can be significantly reduced compared with that of conventional dc-dc converters.

3.4.1.5 Leakage Inductance in the Transformers

Every practical transformer inevitably possesses leakage inductance due to the leakage flux which does not link with all the turns of the imperfectly-coupled windings. The leakage inductance can be beneficial or harmful to the overall performance of the system depending on how the current in the transformer is controlled to transfer power.

In the case of the 'main' converter of the proposed DUP converter, no regenerative current is caused by the leakage inductance (L_{lk_main}) because the converter switches under the ZCS condition. The leakage inductance only acts as a current limiting filter and is connected in series with the output filter inductance (L_{filter}). Therefore, the transformer for the 'main' converter can be designed to have large leakage inductance so that the required output filter inductance can be reduced even further. Furthermore, allowing large leakage inductance facilitates manufacturing transformers especially with high-voltage isolating requirements. Therefore, it is clear that the leakage inductance in the 'main' converter is beneficial and can be fully utilized in the DUP converter.

On the other hand, the leakage inductance in the 'control' converter (L_{lk_ctrl}) causes the regenerative current in the input side owing to the hard switching as shown in Fig. 3.34(c).

When the leakage inductance is referenced to the secondary side of the transformer, it can be regarded as being connected to both the output filter inductance (L_{filter}) and the leakage inductance of the 'main' converter (L_{lk_main}) in series. However, the output current flows in this leakage inductor only when the output current is in the state of rising (during On-state) as shown in Fig. 3.34(b). In other words, L_{lk_ctrl} causes difference in the total output filter inductance depending on the switching states. Therefore, the leakage inductance in the 'control' converter may not benefit the overall performance and should be avoided as much as possible.

3.4.1.6 *Input and Output Filter Capacitors (C_{in} and C_o)*

Since the proposed DUP converter operated in the DCM over the entire operating range, the input and output currents contain high current ripple components. The DUP converter is normally installed in between two long power transmission cables which have considerable amounts of resistance. To reduce the voltage fluctuations caused by the current ripples on both the input and output sides, the filter capacitors, C_{in} and C_o, are required to be placed as close as possible to the input and output terminals. The high-voltage power capacitor technology, such as a power ring film capacitor [27], has been developed recently due to the rapid development of HVDC systems and might be used to effectively suppress the voltage ripples caused by the high current ripples.

The design of input filter capacitance (C_{in}) is closely related to an input voltage control method and, in turn, the dynamic performance of the overall system. However, the focus of this subchapter is restricted to introducing the topology and analyzing the steady-state performance of the proposed converter. The same voltage control method introduced in subchapter 3.3.3 can be directly employed here, since both the converters have basically the same control objective.

On the other hand, the design of output filter capacitance (C_o) to suppress the voltage ripples caused by the high output current ripples is quite straightforward. Assuming that the average current to the output load, I_{load}, is constant during one switching period, the output current from the converter, i_{conv_o}, at the rated power can be drawn as Fig. 3.38.
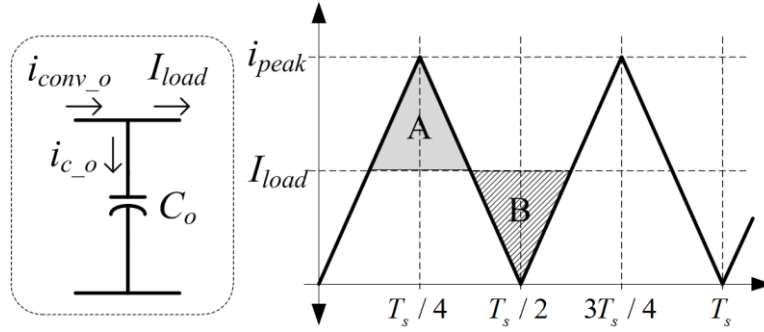
Fig. 3.38. Output current waveform from the DUP converter at the rated power.

Area 'A' represents the amount of excessive charges that is pushed to the output filter capacitor so that it causes a voltage rise in the output filter capacitor; on the contrary, Area 'B' represents the amount of deficit charges and causes a voltage dip. Therefore, by calculating the area either 'A' or 'B', the voltage peak-to-peak ripple can be expressed as below.

$$\Delta V_{pp} = \frac{1}{C_o}(\frac{i_{peak} - I_{load}}{2})\frac{T_s}{4}$$ (3.43)

Since I_{load} is equal to half of i_{peak} at the steady-state, the minimum capacitance required to restrict the ripple to ΔV_{pp} can be obtained as

$$C_o = \frac{i_{peak} \cdot T_s}{16 \cdot \Delta V_{pp}}.$$ (3.44)

3.4.2 Comparative Simulation for the DC-Grid Wind Farm Application

To verify the effectiveness of the proposed converter, comparative simulation has been performed. A Continuous Conduction Mode Full-Bridge (CCMFB) dc-dc converter, a Discontinuous Conduction Mode Full-Bridge (DCMFB) dc-dc converter and the proposed DUP converter based dc-dc converter have been compared in terms of the required output filter inductance and the power losses in the power switching devices. The selected application for the comparative simulation is a dc-grid wind farm, more specifically, the dc-dc converter station which transfers all the power in the collection grid to an HVDC transmission line by stepping up the voltage level as shown in Fig. 3.2. The simulation in this subchapter has focused only on the steady-state analysis assuming that both the input and output voltages are kept at constant values.

The specifications of the target system can be summarized as 150 MW rated power, 50 kV input voltage, and 150 kV output voltage. The CCMFB converter serves as a baseline.

It is assumed that the allowed peak-to-peak current ripple at the output terminal is 40% of the nominal output current at the rated power. The DCMFB converter is also included in this analysis in an effort to reduce the output filter inductance. The peak-to-peak output current ripple of the DCMFB is set to twice (200%) the nominal output current at the rated power. Finally, the proposed converter is also assumed to have the same peak-to-peak output current ripple with the DCMFB. According to the above assumptions, the maximum voltage and current stresses on the switching devices at certain transformer turn-ratios can be summarized as Table 3.5.

For the IGBT switches at the input side, 5SNA 2000K450300 from ABB [28], which is specially designed for series connection (failures being a stable shorted state), has been chosen. The rated current (I_c) is 2000 A and the rated voltage (V_{ces}) is 4500 V. It is assumed that each switch should withstand a dc voltage of 2800 V in steady-state to have some margin for transients and faults. For the power diodes in the output side, 5SDF 28L4520 also from ABB [29], which is a press-pack type, has been chosen. The maximum average on-state current ($I_{F(AV)M}$) is 2620 A and its repetitive peak reverse voltage (V_{RRM}) is 4500V. It is assumed that each diode should withstand a dc voltage of 2800 V. According to the above ratings and the maximum stresses, the number of semiconductor modules required in series and parallel can be summarized as the Table 3.6. In order to keep the semiconductor modules well within the safe operating region, the numbers of devices are determined based on the maximum stresses.

Table 3.5. Maximum Voltage and Current Stresses on the Switching Devices

Maximum Stresses		CCMFB	DCMFB	DUP	
				Main	Control
Input (IGBT)	Voltage (kV)	50	50	50	50
	Current (A)	3960	6600	5400	1200
Output (Diode)	Voltage (kV)	165	165	135	30
	Current (A)	1200	2000	2000	2000
Trans. Turn-Ratio		1:3.3	1:3.3	1:2.7	1:0.6

Table 3.6. Number of Modules Required in Series and Parallel

# of Modules		CCMFB	DCMFB	DUP	
				Main	Control
Input (IGBT)	Series	18	18	18	18
	Parallel	2	4	3	1
Output (Diode)	Series	59	59	48	11
	Parallel	1	1	1	1

Simulations have been performed to estimate the power losses in the semiconductor devices using the thermal modelling of PLECS®. It is assumed that all the semiconductor devices are operating at 125℃ under the rated power condition. All the transformers are

assumed to be ideal with 10 μH leakage inductance (losses of the transformers are all assumed to be the same and not included in the calculation). The power losses at the rated power are summarized in Table 3.7 and the power losses at different wind speeds are shown in Fig. 3.39. As it can be seen from the simulation results, the proposed converter not only requires the least filter inductance, but also has the least power losses in the semiconductor devices.

Table 3.7. Power Losses at the Rated Power (150 MW)

Losses		CCMFB	DCMFB	DUP		
				Main	Ctrl	Sum
IGBT	Con.(kW)	335.2	265.8	250.1	22.5	272.6
	Sw.(kW)	1482.7	2497.2	0	463.9	463.9
Diode Bridge(kW)		180.9	196.4	165.4	33.2	198.6
Total Loss (kW)		1998.8	2959.4	415.5	519.6	935.1
Total Loss (%)		**1.33**	**1.97**	**0.62**		
Required Filter Inductance (mH)		**17.0**	**3.3**	**1.8**		
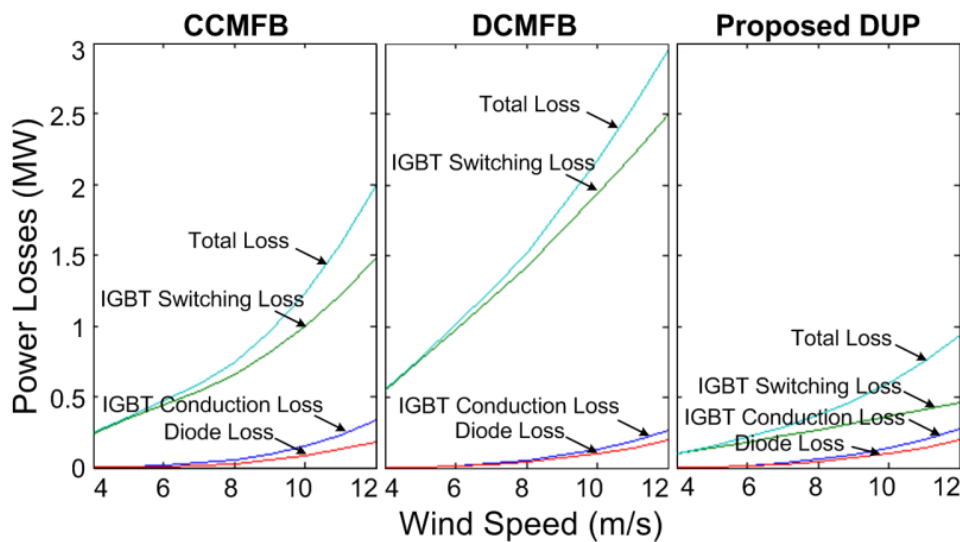
Fig. 3.39. Power losses of the dc-dc converters at different wind speeds.

Fig. 3.40 shows the power losses and the required filter inductance of the proposed DUP converter with respect to the operating switching frequency ranging from 500 Hz to 4 kHz at its rated power of 150 MW. Since there is no switching loss in the 'main' converter and the rated power of the overall converter is kept constant, the total power loss of the 'main' converter is constant regardless of the switching frequency. On the other hand, since the switching loss dominates in the 'control' converter, the total power loss of the 'control' converter increases proportionally to the operating switching frequency. The total loss of the overall converter is also shown in the figure and it is also proportional to the switching

frequency. Since the rated power of the overall converter is kept constant, the required filter inductance is inversely proportional to the operating switching frequency.
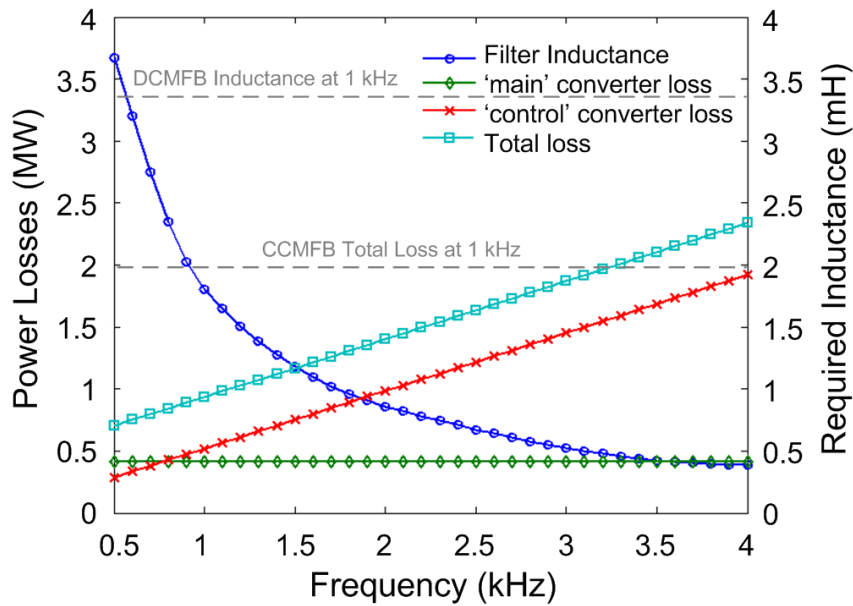
Fig. 3.40. Power losses and required filter inductance of the proposed DUP converters with respect to the operating switching frequency at the rated power.

It is worth noting that, if the total power loss of the DUP converter is allowed up to that of the CCMFB converter with 1 kHz switching frequency, the proposed DUP converter can operate at 3.3 kHz with filter inductance of only 0.42 mH. Furthermore, if the filter inductance is allowed up to that of the DCMFB converter at 1 kHz, the proposed DUP converter can now operate at 580 Hz with the total power loss of only 742 kW. This comparative analysis well proves superiority of the proposed DUP converter in terms of the switching device power losses and the required filtering inductance.

3.4.3 Experiments

A small-scaled prototype for the laboratory experiment has been built to verify the operational principle of the proposed DUP converter based dc-dc converter as shown in Fig. 3.41. The specifications for the prototype are summarized in Table 3.8.

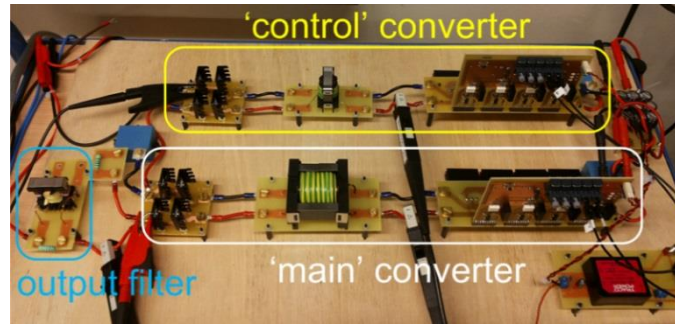Fig. 3.41. Small-scaled prototype of the proposed DUP converter for laboratory experiment.

Table 3.8. The Prototype Specifications

Power		1 kW
Input voltage		208 V
Output voltage		630 V
Switching Frequency		10 kHz
Trans. turn-ratio	'main'	2.75
	'control'	0.57
Leakage Inductance	'main'	2 µH
	'control'	1 µH
Filter Inductance		455 µH

Fig. 3.42 shows the typical experimental voltage and current waveforms with various duty-ratios of the 'control' converter. As can be seen from the figures, the full-bridge of the 'main' converter always switches at its full duty-ratio (0.5) regardless of the duty-ratio of the 'control' converter. The transformer input current of the 'main' converter always reduces to zero before any switching occurs in the full-bridge of the 'main' converter. In this way, the ZCS is always ensured in the 'main' converter. In addition, due to the large filter inductance, the currents in both the 'main' and 'control' converters increase slowly when the IGBT is turning on.

Fig. 3.43 shows the voltage and current waveforms of one IGBT switch in the 'main' converter at the full duty-ratio. Due to the large filter inductance, the current increases slowly when the IGBT is turning on. As it can be seen from Fig. 3.43(b), the current increases slowly after the voltage drops to zero first. Therefore, the switching loss for the IGBT turn-on is negligible. When the switch is turning off, current decreases near to zero first, and the voltage starts to increase as shown in Fig. 3.43(c). Therefore the switching loss for the IGBT turn-off is also very small. It is worth noting that the IGBT current never reaches zero when the switch turns off because there always exists the magnetization current of the transformer. However, the magnetization inductance of the transformer is usually designed to be large enough to limit the amplitude of the magnetization current to a small value. Therefore, the switching loss will be very small too.
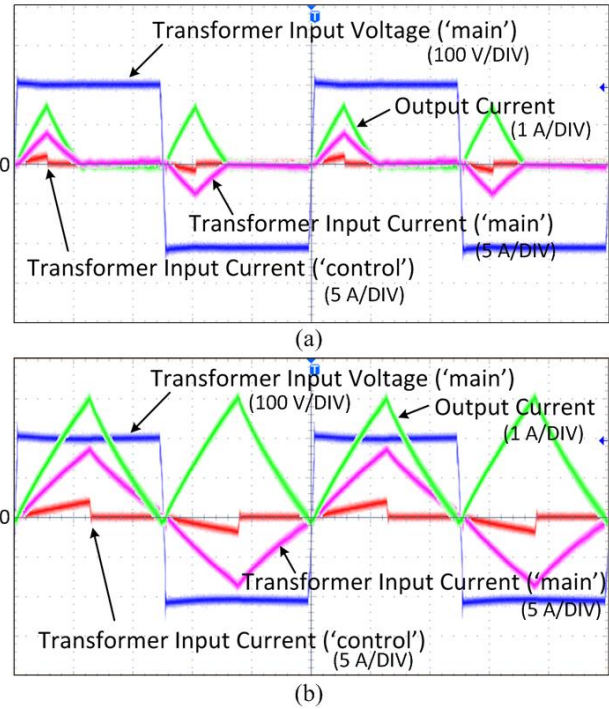
Fig. 3.42. Typical voltage and current waveforms when the duty-ratio of the 'control' converter is (a) 0.1 and (b) 0.25 (rated power).
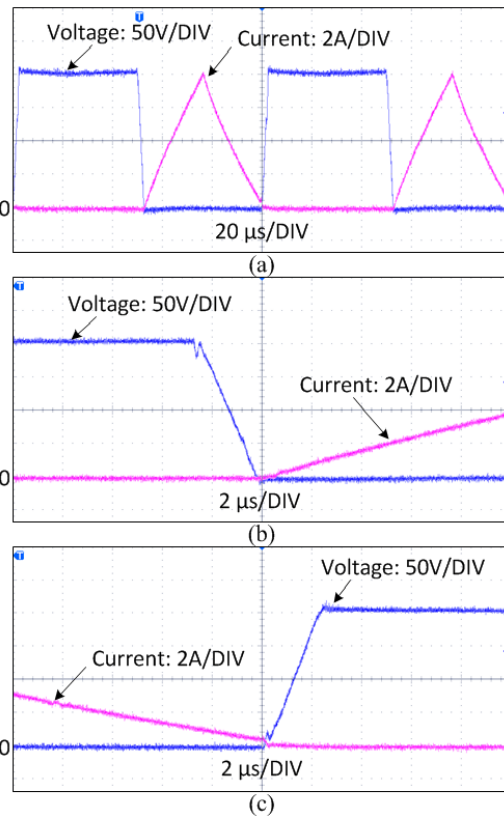

Fig. 3.43. Voltage and current waveforms of one IGBT switch in the 'main' converter at the rated power; enlarged waveforms (b) at the switch turn-on and (c) at the switch turn-off.

To calculate the turn-off switching loss in the 'main' converter, both the voltage and current data for every 80 ns has been extracted from the snapshot of the IGBT voltage and current waveforms. From the extracted data, the energy loss per switching has been obtained by multiplying the voltage and current data and integrating them. It measures 7.32 μJ for this experiment. By multiplying the frequency (10 kHz) to the energy, the turn-off switching loss can be achieved as 73.2 mW. Since there are four IGBT switches in the 'main' converter, the overall turn-off switching loss of the 'main' converter is 0.29 W, which is 0.029% of the rated power.

Fig. 3.44 shows the voltage and current waveforms of one IGBT switch in the 'control' converter at the full duty-ratio. Likewise the 'main' converter, when the IGBT is turning on, the current increases slowly due to the large filter inductance as shown in Fig. 3.44(b). Therefore, the switching loss for the IGBT turn-on is negligible too. When the IGBT is turning off, however, the situation differs from the 'main' converter. The 'control' converter performs hard-switching. Therefore, there exists a turn-off switching loss due to the trailing current of the IGBT as can be seen from Fig. 3.44(c). This turn-off switching loss is the major cause of the overall switching losses of the proposed DUP converter.
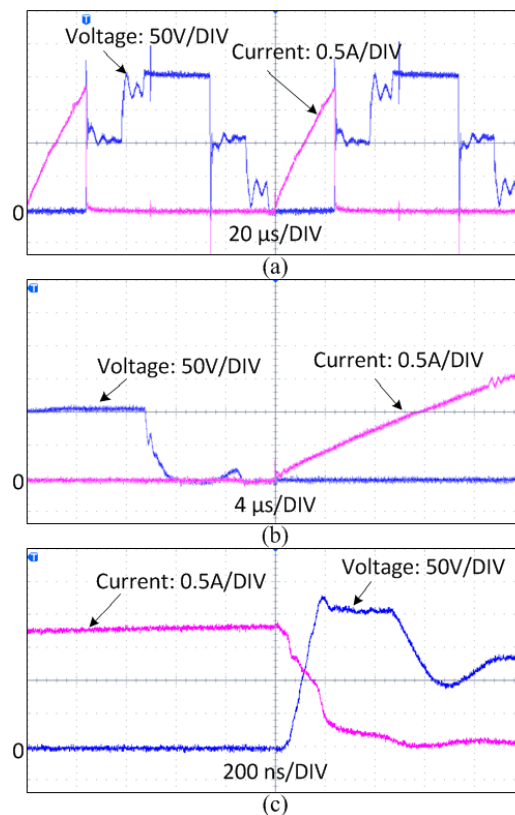

Fig. 3.44. Voltage and current waveforms of one IGBT switch in the 'main' converter at the rated power; enlarged waveforms (b) at the switch turn-on and (c) at the switch turn-off.

To calculate the turn-off switching loss in the 'control' converter, both the voltage and current data for every 20 ns has been extracted from the snapshot of the IGBT voltage and current waveforms. From the extracted data, the power loss has been calculated as 304.83 mW. Since there are four IGBT switches in the 'control' converter the overall turn-off switching loss in the 'control' converter is 1.22 W, which is 0.122% of the rated power.

Therefore, the overall turn-off switching loss of the DUP converter is 0.29 W + 1.22 W = 1.51 W, which is 0.151% of the rated power. It is worth noting that the switching loss of the 'main' converter is around 24% as small as that of the 'control' converter, even though the 'main' converter processes around 9.6 times as much power as the 'control' converter.

3.5 Summary

In this chapter, both the steady-state and dynamic analyses of the interleaved PCSAB dc-dc converter have been presented. Various equations describing the steady-state and dynamic characteristics of the converter have been derived. The design and control methods have been proposed based on these equations and verified by means of simulation and experiment. Both the structural and operational characteristics of the PCSAB dc-dc converter have been proven to be well suited for high-power applications.

In addition, a new open-circuit fault detection method and its tolerant control strategy for the PCSAB dc-dc converter have been presented. The proposed fault detection method can identify the location and type of the fault in no more than two switching periods using only one current sensor in the output. The proposed fault-tolerant operation can transfer the full rated power even under the fault condition when the Type-1 open-circuit fault has occurred. In the case of the Type-2 open-circuit fault, it still improves the quality of the input and output currents by adjusting the phase shifting angle among intact modular converters. The feasibility and effectiveness of the proposed fault detection and fault-tolerant methods also have been verified by simulation and experiment.

Finally, a novel DUP converter based dc-dc converter and its design and control methods have been introduced. The main objectives of the proposed converter are to reduce the power losses in the power semiconductor devices and to reduce the output filter inductance. The proposed converter utilizes two full-bridge converters in a special way to reduce the power losses and the output filter inductance. The proposed converter is expected to be highly beneficial for high-power applications where the dc voltage transformation is required. To verify the effectiveness of the converter for the high-power applications, a

comparative analysis especially for the dc-grid wind farm application has been presented. The proposed converter not only requires the least filter inductance, but also has the least power losses in the semiconductor devices. Finally, a small-scaled prototype and its experimental results have been presented to verify the operational principle of the proposed converter.

References

[1]   M.E. Baran and N.R. Mahajan, "Dc distribution for industrial systems: Opportunities and challenges," IEEE Trans. on Industry Apllications, vol. 39, no. 6, pp. 1596-1601, Nov/Dec 2003.

[2]   D.J. Hammerstrom, "Ac versus dc distribution systems-Did we get it right?" in Proc. IEEE Power Eng. Soc. General Meeting, pp. 1-5, Jun. 2007.

[3]   X. Liu, P. Wang, and P.C. Loh, "A hybrid ac/dc microgrid and its coordination control," IEEE Trans. on Smart Grid, vol. 2, no. 2, pp. 278-286, Jun. 2001.

[4]   Z. Wang and H. Li, "An integrated three-port bidirectional dc-dc converter for PV application on a dc distribution system," IEEE Trans. on Power Electronics, vol. 28, no. 10, pp. 4612-4624, Oct. 2013.

[5]   D. Jovcic, "Interconnecting offshore wind farms using multiterminal VSC-based HVDC" in Proc. IEEE Power Eng. Soc. General Meeting, pp. 1-7, Jun. 2006.

[6]   S.M Muyeen, R. Takahashi, and J. Tamura, "Operation and control of HVDC-connected offshore wind farm," IEEE Trans. on Sustainable Energy, vol. 1, no. 1, pp. 30-37, Apr. 2010.

[7]   L. Wang, K.H. Wang, W.J. Lee, and Z. Chen, "Power-flow control and stability enhancement of four parallel-operated offshore wind farms using a line-commutated HVDC Link," IEEE Trans. on Power Delivery, vol. 25, no. 2, pp. 1190-1202, Apr. 2010.

[8]   C. Meyer, M. Höing, A. Peterson, and W.D. Doncker, "Control and design of dc grids for offshore wind farms," IEEE Trans. on Industry Applications, vol. 43, no. 6, pp. 1475-1482, Feb. 2007.

[9]   J. Robinson, D. Jovcic, and G. Joos, "Analysis and design of an offshore wind farm using a MV DC grid," IEEE Trans. on Power Delivery, vol. 25, no. 4, pp. 2164-2173, Oct. 2010.

[10]   L. Max and S. Lundberg, "System efficiency of a DC/DC converter-based wind farm," Wind Energy, vol. 11, pp. 109-120, Oct. 2008.

[11]   F. Deng and Z. Chen, "Control of improved full-bridge three-level dc/dc converter for wind turbines in a dc grid," IEEE Trans. on Power Electronics, vol. 28, no. 1, pp. 314-324, Jan. 2013.

[12]   W. Chen, A. Huang, C. Li, G. Wang, and W. Gu, "Analysis and comparison of medium voltage high power dc/dc converters for offshore wind energy systems," IEEE Trans. on Power Electronics, vol. 28, no. 4, pp. 2014-2023, Apr. 2013.

[13]   F. Deng and Z. Chen, "An offshore wind farm with dc grid connection and its performance under power system transients" in Proc. IEEE Power and Energy Society Genernal Meeting, pp. 1-8, Jul. 2011.

[14]   N. Denniston, A. Massoud, S. Ahmed, and P. Enjeti, "Multiple-module high-gain high-voltage dc–dc transformers for offshore wind energy systems," IEEE Trans. on Industrial Electronics, vol. 58, no. 5, pp. 1877-1886, May, 2011.

[15]   S.-J. Cheng, Y.-K. Lo, H.-J. Chiu, and S.-W. Kuo, "High-efficiency digital-controlled interleaved power converter for high-power PEM fuel-cell applications," IEEE Trans. on Industrial Electronics, vol. 60, no. 2, pp. 773–780, Feb. 2013

[16]   F.S. Garcia, J.A. Pomilio, and G. Spiazzi, "Modeling and control design of the interleaved double dual boost converter," IEEE Trans. on Industrial Electronics, vol. 60, no. 8, pp. 3283-3290, Aug. 2013.

[17]   G. Ortiz, J. Biela, and J.W. Kolar, "Optimized design of medium frequency transformers with high isolation requirements" in Proc. IECON 2010 – 36th Annual Conference on IEEE Industrial Electronics Soc., pp. 631-638, 2010.

[18]   K. Park and Z. Chen, "Analysis and design of a parallel-connected single active bridge dc-dc converter for high-power wind farm application" will be presented in 15th European Conference on Power Electronics and Applications, Sep. 2013.

[19]   B.T. Irving and M.M. Jovanovic, "Analysis, design, and performance evaluation of droop current-sharing method" in Proc. 15th Annu. IEEE Appl. Power Electon. Conf., 2000, pp. 235-241.

[20]   B.A. Miwa, D.M. Otten, and M.F. Schlecht, "High efficiency power factor correction using interleaving techniques" in Proc. Applied Power Electronics Conference and Exposition, 1992, pp. 557-568.

[21]   K.J. Astrom and B. Wittenmark, Adaptive control, ISBN: 0201558661, Prentice Hall; 2 edition, Dec. 1994.

[22]   V. Blasko and V. Kaura, "A new mathematical model and control of a three-phase ac-dc voltage source converter," IEEE Trans. on Power Electronics, vol. 12, no. 1, pp. 116-123, Jan 1997.

[23]   C. Bajracharya, M. Molinas, J. A. Suul, and T. Undeland, "Understanding of tuning techniques of converter controllers for VSC-HVDC," in Proceedings of NORPIE 2008, Helsinki, Finland, 09-11 June 2008.

[24]   W. Leonhard, *Control of electrical drives*, ISBN: 3540418202, Springer; 3rd edition, Aug. 2001.

[25]   Y.J. Ko, K.B. Lee, D.C. Lee, and J.M. Kim, "Fault diagnosis of three-parallel voltage-source converter for a high power wind turbine," IET Power Electronics, vol. 5, no. 7, pp. 1058-1067, Aug. 2012.

[26]   U.M. Choi, K.B. Lee, and F. Blaabjerg, "Diagnosis and tolerant strategy of an open-switch fault for T-type three-level inverter systems," IEEE Trans. on Industry Applications, IEEE Early Access Articles, 2013.

[27]   T.A. Hosking and M.A. Brubaker, "Stacked annular form factor film capacitors for high voltage and high current applications" in Proc. 16th IEEE Pulsed Power Conf., pp. 290-293, 2007.

[28]   5SNA 2000K450300 Data Sheet (Mar. 2013) [online]. Available: http://www.abb.com/semiconductors

[29]   5SDF 28L4520 Data Sheet (Feb. 2013) [online]. Available: http://www.abb.com/semiconductors

Chapter 4

Modelling and Control of a DC-Grid Wind Farm

4.1 Introduction

This chapter presents modelling and control of a dc-grid wind farm with the Parallel-Connected Single Active Bridge (PCSAB) dc-dc converters introduced in Chapter 3.3. A short review on a dc-grid wind farm configuration and a PCSAB dc-dc converter are given first. The dc-grid wind farm is modelled in two different ways depending on the requirements of the simulation: an average model and a switching model. The average model considers only the average characteristics of the system, so that it requires less simulation time and provides insight into the overall performance of the system. Meanwhile, the switching model provides much detailed information, though it requires longer simulation time. The control of the dc-grid wind farm is developed based on the obtained models and evaluated through various simulation studies. The developed models and control methods are expected to be useful for further studies on the operation of a dc-grid wind farm under various input and fault conditions.

4.2 Short Review on a DC-Grid Wind Farm and a PCSAB dc-dc Converter

4.2.1 DC-Grid Wind Farm Configuration

An example of a dc-grid offshore wind farm configuration is shown in Fig. 4.1. Each Wind Turbine (WT) consists of a generator, a full-power active rectifier, which is responsible for regulating the power output of the generator, and an 'internal' dc-dc converter, which

keeps the internal dc-link voltage constant at its rated value by controlling the power flow in the system. WTs are connected in paralleled-radial dc cables to the 'station' dc-dc converter, which maintains the internal dc-grid voltage as constant as possible at its rated value.

There are three different rated dc voltage levels (generator, collection, and transmission) in the entire wind farm configuration. The internal dc-link voltage levels for high-power (several MWs) generators usually range from several kV up to around 10 kV. The dc-grid (collection) voltage levels are normally from 30 kV to 60 kV, and the dc-transmission voltage levels are from 150 kV or even higher, which depends on the power rating of an offshore wind farm and its distance to the shore [1]-[7]. In this thesis, the generator, collection, and transmission voltages are assumed to be 5 kV, 50 kV, and 150 kV, respectively.
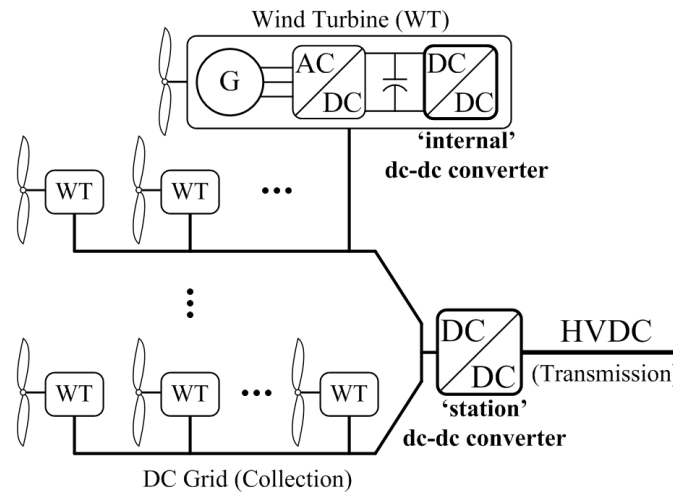

Fig. 4.1. Example of an offshore dc-grid wind farm configuration.

4.2.2 PCSAB DC-DC Converter

A circuit configuration of a PCSAB dc-dc converter is shown in Fig. 4.2. The PCSAB dc-dc converter employs Single Active Bridge (SAB) converter as a modular converter. Since each SAB converter operates in a Discontinuous Conduction Mode (DCM), only a small filter inductance is required. Since the leakage inductance of the transformer is connected with the filter inductance in series, it can be fully utilized as a part of the filter inductance. By paralleling lower-power modular converters, not only the power ratings of each modular converter can be reduced to manageable levels, but also the redundancy implementation and the ease of maintenance can be achieved. By interleaving the switching sequences among the modular converters, both the input and output current ripples can be reduced and the effective ripple frequency can be increased significantly. These characteristics of the PCSAB dc-dc

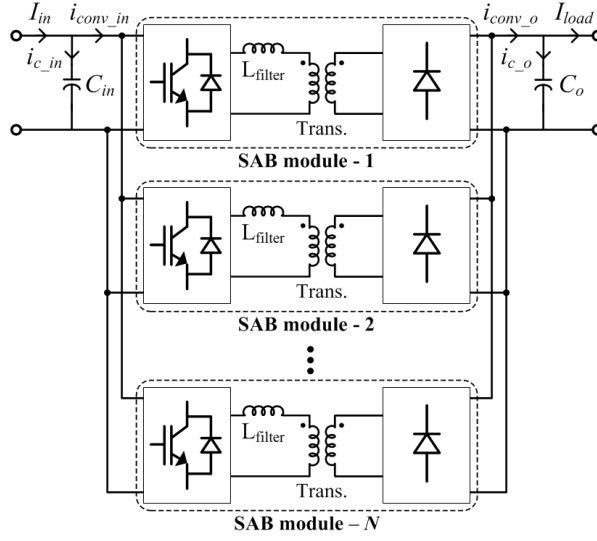converter are expected to be highly beneficial especially for the offshore wind farm applications [8, 9].

Fig. 4.2. *N*-parallel-connected SAB dc-dc converter.

4.3 Modelling of a DC-Grid Wind Farm

4.3.1 Wind Power Conversion System

4.3.1.1 Wind Turbine

If the wind turbine is controlled to keep tracking the Maximum Power Points (MPP) at various wind speeds, the power captured from the turbine can be expressed as a function of the cube of the wind speed as shown below [10].

$$P_m = T_m \omega_T = C \cdot V^3 , \qquad (4.1)$$

where T_m is the mechanical torque and ω_T is the rotational speed of the turbine. V is the wind speed and C is the constant which can be defined as below.

$$C = \frac{1}{2} \pi \rho C_p (\lambda, \beta) R^2 , \qquad (4.2)$$

where ρ is the air density (typically 1.25 kg/m^3), $C_p(\lambda, \beta)$ is the power coefficient, λ is the tip-speed ratio, β is the pitch angle, and R is the blade radius. The power coefficient can be controlled by changing the tip-speed ratio and the pitch angle of the blade. The MPP Tracking (MPPT) control implies that the wind turbine is controlled to keep the power coefficient at its maximum value over a certain wind speed range.

93

4.3.1.2 Generator

Typical generators, which operate with a full-power converter, are Induction Generator (IG) and Permanent Magnet Synchronous Generator (PMSG). Although the IG and PMSG are ac machines, both can be regarded as a simple dc machine if the generators are controlled by an active rectifier with vector control (or field-oriented control) and the cross-coupling components are assumed to be compensated well [11]. Hence, in this thesis, the generator is represented by a simple DCG with permanent-magnet field.

The electric part of a DCG can be modelled as

$$v_{emf} - v_t = L_g \frac{di_g}{dt} + R_g i_g ,$$ (4.3)

where v_t and i_g are the terminal voltage and the armature current, respectively, of the generator, L_g and R_g are the inductance and resistance, respectively, in the generator armature windings, and v_{emf} is the back electromotive-force. v_{emf} is proportional to the speed of the generator ($v_{emf}=k_b \cdot \omega_g$, where k_b is the voltage constant and ω_g is the speed of the generator).

The mechanical part of a dc machine can be modelled as

$$T_m - T_e = J \frac{d\omega_g}{dt} + B\omega_g ,$$ (4.4)

where T_e is the electromagnetic torque which is proportional to the armature current ($T_e=k_t \cdot i_g$, where k_t is the torque constant), J and B are the total equivalent inertia and damping, respectively, of the wind turbine rotor-generator combination.

4.3.1.3 Active Rectifier

The active rectifier is modelled as an ideal variable transformer which applies v_t to the armature terminals of the DCG to determine i_g. Assuming no power loss in the ideal variable transformer, it simply determines output current (i_{ro}) based on the input power ($v_t \cdot i_g$) and the output voltage (v_{dc_link}) of the active rectifier, which is the internal dc-link voltage of the wind turbine, as

$$i_{ro} = (v_t \cdot i_g) / v_{dc\_link} .$$ (4.5)

The overall modelling of the generator and the active rectifier is summarized as a block diagram in Fig. 4.3.
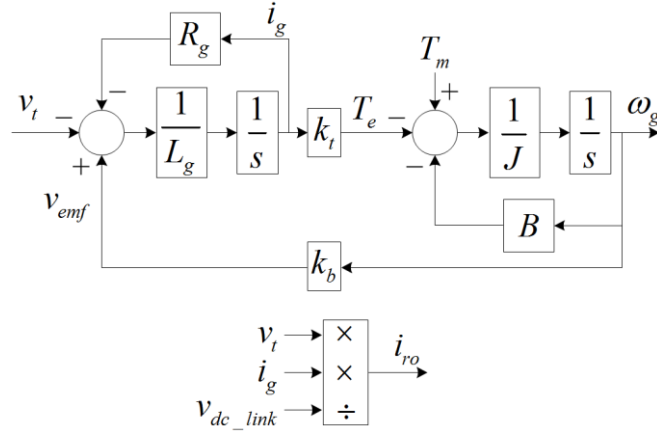
94

Fig. 4.3. Overall modelling of the generator and the active rectifier.

4.3.2 DC-DC Converters

The dc-dc converters (both 'internal' and 'station') in Fig. 4.1 can be modelled in two different ways depending on the requirements of the simulation: an average model and a switching model. The average model considers the average characteristics of the system, but cannot be used for detailed investigations of the switching behavior of the converter. The switching model enables the detailed investigations, but requires a short simulation time step and, in turn, will take much more simulation time than the average model.

Assuming no power loss in the dc-dc converter, the average model can be simply modelled with two current sources as shown in Fig. 4.4. The input current to the converter (i_{conv_in}) is determined by an input voltage control method, which will be explained in the next section, and the output current from the converter (i_{conv_o}) is determined by

$$i_{conv\_o} = \frac{v_{in} \cdot i_{conv\_in}}{v_o}.$$ (4.6)
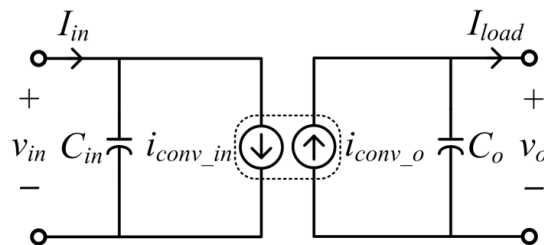

Fig. 4.4. Equivalent circuit for the average model of the dc-dc converter.

The switching model can be constructed as shown in Fig. 4.2 using actual power switch, such as IGBT, power diode, and transformer models.

95

4.3.3 DC Cables

The dc cables in the dc-grid wind farms can be modelled with the π-section model as shown in Fig. 4.5(a) [12]. The dc cables between the wind turbines are located between two capacitors, which are the output filter capacitors (C_o) for the 'internal' dc-dc converter. Since the distances between wind turbines are normally short (1 km in this thesis), the cable capacitance (C_{cable}) is much smaller than C_o. Hence, if the output filter capacitor is moved to the cable model, the cable capacitor can be simply replaced with the filter capacitor as shown in Fig. 4.5(b). By the same token, the dc cable between the first wind turbines in the strings and the 'station' dc-dc converter can be modelled as shown in Fig. 4.5(c), where C_{in_st} is the input capacitor of the 'station' dc-dc converter.
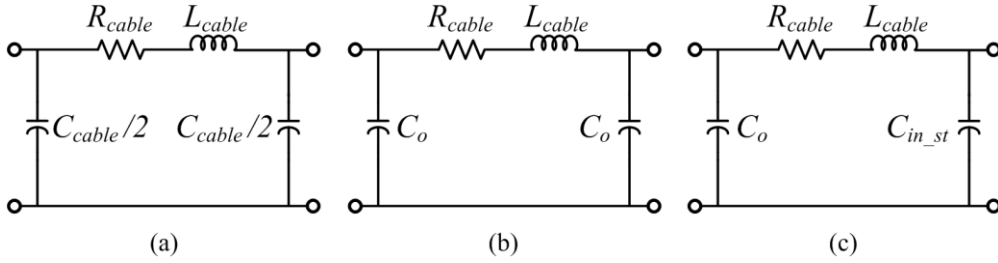

Fig. 4.5. The π-section dc cable models: (a) general, (b) between wind turbines, and (c) between the first wind turbines and the 'station' dc-dc converter.

4.4 Control of a DC-Grid Wind Farm

4.4.1 Control of the Wind Turbines

4.4.1.1 Maximum Power Point Tracking

As mentioned in subchapter 4.3.1, the generated power from a wind turbine is a function of the wind speed and the power coefficient which is, in turn, a function of the tip speed of the blade. Wind turbines have different functions of the power coefficient depending on their structural designs and pitch control. To obtain available power from the wind turbine as much as possible, the active rectifier connected to the generator has to perform a control called Maximum Power Point Tracking (MPPT). The MPPT is a process that, under a certain wind speed, the rotational speed of the generator is adjusted to a certain value, so that the power from the turbine can be the maximum. If the turbine is controlled to maintain an optimal tip-speed ratio, λ_{opt}, at various wind speeds, they can achieve their own maximum power coefficients.

Fig. 4.6 shows the mechanical output power of a wind turbine at various wind speeds. For every wind speed within the rated range, there exists a maximum power point (MPP) where the turbine is operating with the maximum power coefficient. The value of the tip-speed ratio is constant for all MPPs, while the rotational speed of the turbine is related to the wind speed as

$$\omega_T^* = \lambda_{opt} \frac{V}{R},$$
(4.7)

where ω_T^* is the optimal rotational speed of the wind turbine at a certain wind speed. In other words, in order to capture the maximum power from the wind stream, the wind turbine should be regulated to operate at the optimal rotational speed at every given wind speed. Many useful MPPT methods are already available in the literature [13].
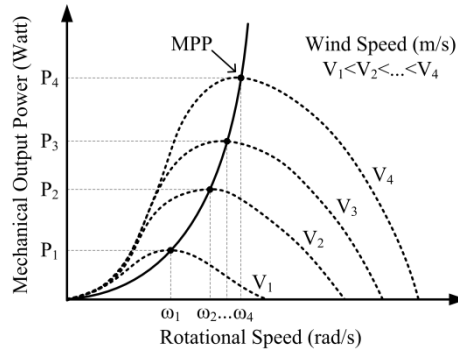

Fig. 4.6. Output power curves of the wind turbine.

4.4.1.2 Control of the Generator

To make the wind turbine operate at its optimal rotational speeds, the speed of the generator has to be controlled. Here, the wind turbine is assumed as a direct-driven type (no gearbox) and a stiff shaft is also assumed to simplify the model of the turbine. The speed of the generator can be controlled by varying the electromagnetic torque (T_e) of the generator. The electromagnetic torque can be controlled by the armature current of the generator (i_g). Therefore, it is common to use double-loop feedback control to control the speed of the generator as shown in Fig. 4.7. k_{p_xx} are the proportional gains (sc: speed control and cc: current control), k_{i_xx} are the integral gains, and k_{a_xx} are the anti-windup gains. The gains are summarized in Table 4.1. The bandwidth of the current controller (f_{cc}) is normally designed to be 1/10~1/20 of the converter switching frequency and that of speed controller (f_{sc}) to be 1/5~1/10 of f_{cc}. Since both control loops have the limiters in the output, the anti-windup loops are added to prevent the saturation in the integrators. In addition, the back-emf, v_{emf}, is feedforwarded to improve the dynamic performance of the control system.
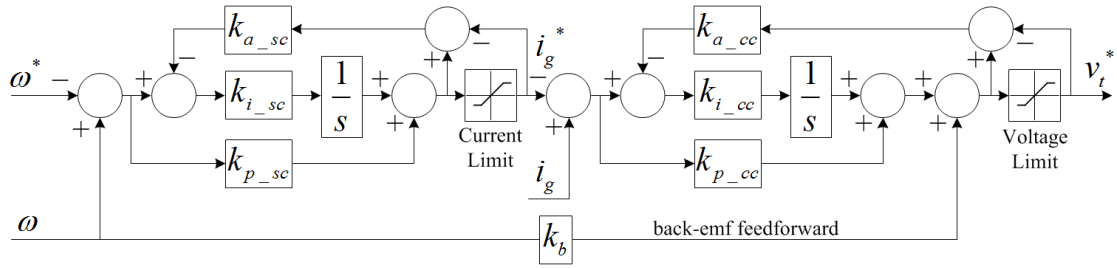
Fig. 4.7. Double-loop feedback control to control the speed of the generator (*sc*: speed control and *cc*: current control).

Table 4.1. Gain Design of the Controllers

Speed Controller (sc)	
ω_{sc}	$2\pi \cdot f_{sc}$
k_{p_sc}	$J \cdot \omega_{sc}/k_t$
k_{i_sc}	$k_{p\_sc} \cdot \omega_{sc}/5 = J \cdot \omega_{sc}^2/(5 \cdot k_t)$
k_{a_sc}	$1/k_{p\_sc} = k_t/(J \cdot \omega_{sc})$
Current Controller (cc)	
ω_{cc}	$2\pi \cdot f_{cc}$
k_{p_cc}	$L_g \cdot \omega_{cc}$
k_{i_cc}	$R_g \cdot \omega_{cc}$
k_{a_cc}	$1/k_{p\_cc} = 1/(L_g \cdot \omega_{cc})$

4.4.2 Control of the DC-DC Converters

Both 'internal' and 'station' dc-dc converter are responsible for maintaining the input voltages (v_{in}) as constant as possible at their rated values. The input voltage of the dc-dc converter can be controlled by controlling the amount of power delivered to the output of the converter depending on the incoming power from the power source. Since each modular SAB converter operates in the DCM, the PCSAB has a nonlinear characteristic and can be regarded as a nonlinear actuator. If the nonlinearity of the actuator is compensated using the inverse function of the nonlinearity [14], a block diagram of the overall input voltage control scheme can be drawn as Fig. 4.8. K_p and K_i are the proportional and integral gains, respectively. T_d is the total converter system delay and is assumed to be 1.5 times of the switching period ($T_d=1.5 \cdot T_s$).
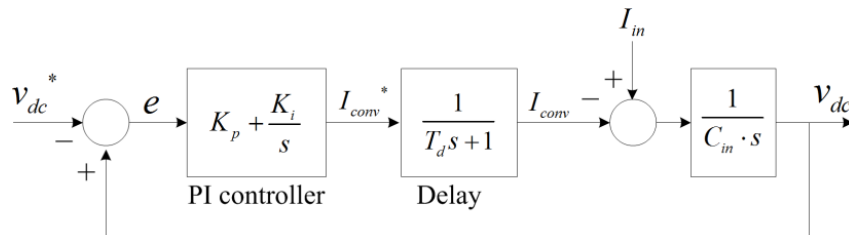

Fig. 4.8. Linearized input voltage control scheme for the PCSAB dc-dc converter.

Using the 'symmetrical optimum design' method, which optimizes the control system behaviour with respect to a disturbance input by maximizing the phase margin at the crossover frequency [15, 16], the proportional gain and the integral gain are

$$K_p = \frac{C}{a \cdot T_d}, \quad K_i = \frac{K_p}{a^2 \cdot T_d},$$
(4.8)

where 'a' is the symmetrical distance which is related to the damping ratio (ζ) of the control system as

$$a = 2\zeta + 1.$$
(4.9)

4.4.3 Control of the Overall DC-grid Wind Farm under Grid Faults

Although it is not presented in Fig. 4.1, another converter station, where the dc power coming in from the sea is converted into ac power at a voltage level in line with an existing ac grid, is usually installed onshore. The onshore station is responsible for maintaining the HVDC transmission voltage level at its nominal value with limited margins by controlling active power. If the onshore station converter is of a VSC type, it can also provide and consume reactive power as the ac grid requires.

If a fault occurs in the ac-grid side, the HVDC transmission voltage level might increase rapidly, since the onshore station converter cannot transfer enough power into the ac grid. To reduce the peak over voltage, a Dynamic Braking Resistor (DBR) can be used to dissipate excessive power in the dc transmission system. However, the amount of power which can be dissipated through this method is much smaller than required. Therefore, the amount of generated power from the wind turbine should be controlled to keep the overall wind farm robust and stable under the fault condition. To realize this, the wind turbine should recognize the fault first either by measuring and monitoring voltage levels within the system or by communication. Using communication within the wind farm and introducing possible feed-forwards between the source and load converters can reduce the required capacitances for the dc-links in the system [17]. In this thesis, control of the overall dc-grid wind farm without communication will be discussed.

If the voltage level of the HVDC transmission line is increased due to the fault in the ac grid, the 'station' dc-dc converter is now facing the increased output terminal voltage. The main objective of the 'station' converter is to maintain its input voltage (dc collection grid voltage) at its nominal value using the control method introduced in the previous subchapter.

However, since the dc-dc converter topologies introduced in this thesis all have fixed voltage transfer ratios, the amount of power, which the dc-dc converters can deliver, decreases as the output terminal voltage increases over its nominal value. Consequently, the input voltage of the 'station' converter also increases. Furthermore, each 'internal' dc-dc converter in the wind turbine is now suffering the increased output terminal voltage. Due to the same reason with the 'station' dc-dc converter, the input voltage of the 'internal' dc-dc converter ('internal' dc-link voltage) also increases as its output terminal voltage increases over its nominal value. Therefore, a fault in the ac grid propagates to the 'internal' dc-link and results in voltage rise at the dc-link as shown in Fig. 4.9.
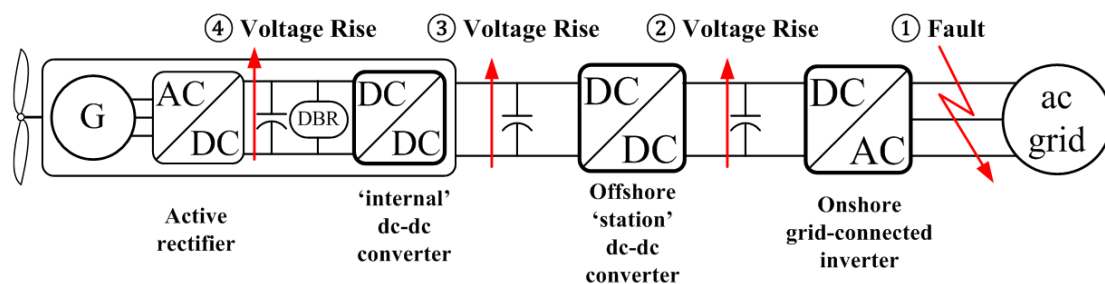

Fig. 4.9. Fault propagation from the ac grid to the 'internal' dc-link.

The active rectifier within the wind turbine synthesizes necessary voltage waveforms using the 'internal' dc-link voltage to control the amount of power production. Therefore, the 'internal' dc-link is an appropriate point to monitor for a fault condition. If the dc-link voltage suddenly increases above a certain pre-set value due to the grid fault, an emergency control scheme can take over the control and try to decrease the amount of power production from the wind turbine by performing the pitch control of the blade or accelerating the turbine momentarily and converting excessive energy into kinetic energy. Furthermore, a DBR can be installed in the dc-link to dissipate the excessive energy much faster. Much research on the wind turbine fault ride-though techniques has already been carried output extensively [18, 19] and these techniques can be easily employed in the dc-grid wind farm applications too.

4.5 Simulation Studies

4.5.1 Average Model of the DC-Grid Wind Farm

To simulate a dc-grid wind farm, an average model of a 150 MW wind farm consisting of 6 strings of 5 wind turbines (each 5 MW) has been built based on the model and control explained in the previous subchapters using Matlab Simulink. The overall simulation

configuration is summarized in Fig. 4.10 and simulation parameters are summarized in Table 4.2.
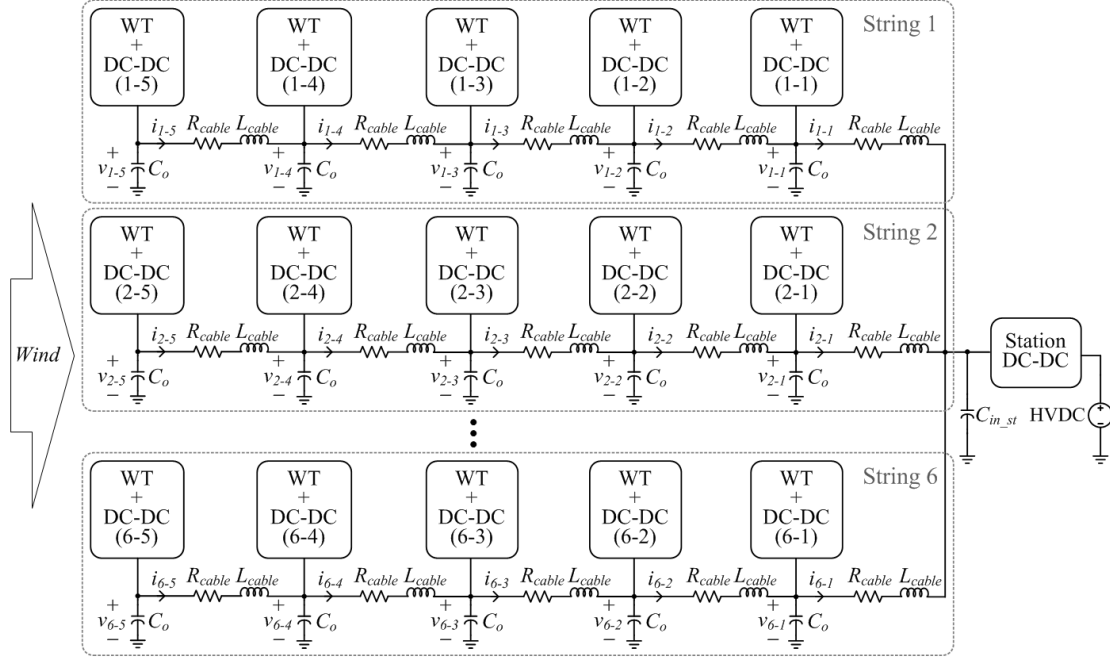

Fig. 4.10. Overall simulation configuration of a 150 MW dc-grid wind farm. (x-n: x is the string number and n is the turbine number)

Table 4.2. Parameters for Simulation

Wind Turbine	
Rated Power	5 MW
Rated Wind Speed	12 m/s
Rated Rotor Speed	15 rpm
Generator Winding Resistance (R_g)	0.65 Ω
Generator Winding Inductance (L_g)	30 mH
Torque and Voltage Constants (k_t, k_b)	1719
Total Equivalent Inertia (J)	$4.96 \cdot 10^6$ kg-m^2
Total Equivalent Damping (B)	0.1 Nm/(rad/s)
Current Controller Bandwidth (f_{cc})	50 Hz
Speed Controller Bandwidth (f_{sc})	5 Hz
'Internal' DC-DC Converter	
Rated Power	5 MVA
Rated Input Voltage (V_{in})	5 kV
Rated Output Voltage (V_o)	50 kV
Switching Frequency ($f_s=1/T_s$)	1 kHz
Number of Parallel Converters (N)	3
System Delay (T_d)	1.5 ms
Transformer Turn-ratio (n)	11.63
Filter Inductance for each (L_{filter})	419.82 μH
Input Capacitance (C_{in})	10 mF
Output Capacitance (C_o)	50 μF
Proportional Gain (K_p)	1.67
Integral Gain (K_i)	69.44

'Station' DC-DC Converter	
Rated Power	150 MVA
Rated Input Voltage (V_{in_st})	50 kV
Rated Output Voltage (V_{o_st})	150 kV
Switching Frequency ($f_{s\_st}=1/T_{s\_st}$)	1 kHz
Number of Parallel Converters (N_{st})	3
System Delay (T_{d_st})	1.5 ms
Transformer Turn-ratio (n_{st})	3.49
Filter Inductance for each (L_{filter_st})	1.40 mH
Input Capacitance (C_{in_st})	3 mF
Output Capacitance (C_{o_st})	160 µF
Proportional Gain (K_{p_st})	0.5
Integral Gain (K_{i_st})	20.83
DC Cable	
Cable Resistance (R_{cable})	106.4 mΩ/km
Cable Inductance (L_{cable})	2.8 µH/km

Fig. 4.11 shows the input wind data for the simulation studies. As it can be seen from Fig. 4.10, the wind is assumed to blow from the last wind turbine (WT$_{x-5}$) side to the first wind turbine (WT$_{x-1}$) side in each string and all the strings see the same wind so that every string has the same loading condition. 10 minutes long wind data with stochastic variations from the average value of 9.2 m/s, which is the measured value of Horns Rev 2 offshore wind farm in Denmark [20], are generated as an input wind speed [21], considering simple wake effect [22] and time delay of the wind to each turbine in the string.
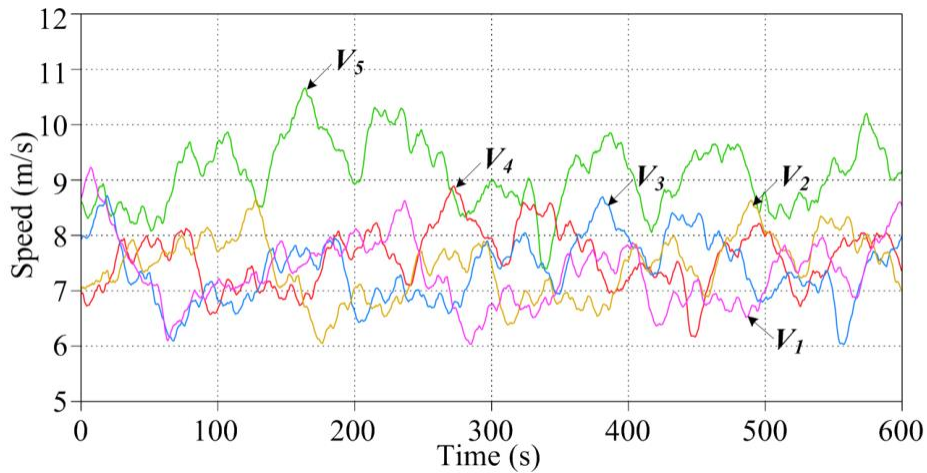
Fig. 4.11. Input wind data. (V_n: wind speed to WT$_{x-n}$)

Fig. 4.12 shows the simulation waveforms of the average model of the 150 MW dc-grid wind farm. Fig. 4.12(a) shows major information about the wind turbine, which is situated at the end of the first string (WT$_{1-5}$). The rotational speed of the turbine changes depending on the input wind speed to track the maximum power points at various wind speeds and, in turn, the generated power from the generator changes accordingly. In other

words, the generated power is the maximum power that the turbine can generate at a given input wind speed.

Fig. 4.12(b) shows major information about the average model of the 'internal' dc-dc converter in the same wind turbine (WT_{1-5}). Although the input current into the dc-dc converter varies depending on the input wind speeds, the input voltage of the 'internal' dc-dc converter is well kept constant at 5 kV. This implies that the input voltage control method introduced in the previous subchapter has satisfactory performance under this input current disturbance condition.

Fig. 4.12(c) shows voltage and current waveforms at different points of the dc cable in the first string. The input voltage to the 'station' dc-dc converter has the lowest value at around 50 kV, but the dc cable voltage increases as the cable is located farther away from the 'main' station. This is mainly due to the resistance of the dc cable. If thinner dc cables with higher resistance are used, the situation will be aggravated. Hence, the 'internal' dc-dc converters in the wind turbines situated farther away from the 'main' station have to be designed considering this increased output terminal voltage conditions. As it can be seen from the current waveforms, the dc cable closer to the 'main' station carries more current. Therefore, using thicker cables with lower resistance for the dc cable sections closer to the 'main' station is obviously beneficial not only for the efficiency of the overall system, but also for alleviating the increased dc cable voltage problem.

Fig. 4.12(d) shows major information about the average model of the 'station' dc-dc converter. Likewise with the 'internal' dc-dc converter, the input current into the dc-dc converter, which is the disturbance to the converter, varies depending on the input wind speeds. However, the voltage of the 'station' input capacitor is well kept constant at 50 kV. In this simulation, the output voltage of the 'station' dc-dc converter, which is the HVDC transmission line voltage, is assumed to be constant at 150 kV. However, the effect of the voltage variations in the HVDC transmission caused by various faults might be tested using this simulation model.
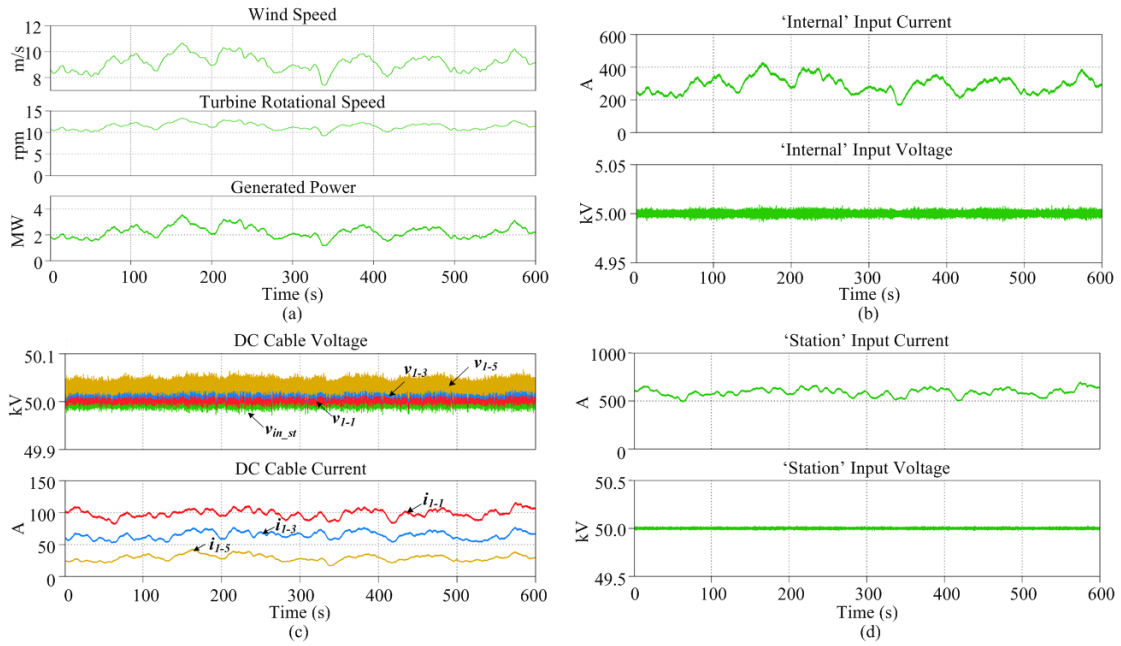
Fig. 4.12. Simulation waveforms of the "average" model of the 150 MW dc-grid wind farm: (a) wind turbine (WT_{1-5}), (b) 'internal' dc-dc converter (WT_{1-5}), (c) dc-cable, and (d) 'station' dc-dc converter.

4.5.2 Switching Model of the DC-Grid Wind Farm

Fig. 4.13 shows the simulation waveforms of the switching model of the 150 MW dc-grid wind farm. The 5MW 'internal' dc-dc converters in the wind turbines and the 150 MW 'station' dc-dc converter are replaced with the switching models. Fig. 4.13(a) shows major information of the same wind turbine (WT_{1-5}). For the switching model, only the beginning 10 seconds of the same wind data are used as an input wind speed, since the switching model requires much smaller simulation step size and, in turn, generates much larger amount of data. Likewise with the average model, the rotational speed of the turbine varies depending on the input wind speed to generate the maximum power at a given wind speed.

Fig. 4.13(b) shows major information about the switching model of the 'internal' dc-dc converter in the same wind turbine (WT_{1-5}). Since the average model is still used for the wind turbine, the input current from the generator to the dc-dc converter is almost identical to the previous model. However, the voltage ripples due to the switching behaviour of the converter can now be observed in the input voltage waveform, though the input voltage is still well controlled at around 5 kV. This also implies that the input voltage control method designed in this simulation study has satisfactory performance under the input current disturbance and switching conditions.

Fig. 4.13(c) shows voltage and current waveforms at different points of the dc cable in the first string. Now, both the dc cable voltages and the dc cable currents contain ripple components due to the switching action of the dc-dc converters. However, the dc cable sections located closer to the 'station' converter still have lower cable voltages and higher cable currents than the ones located farther away from the 'station' converter.

Fig. 4.13(d) shows major information about the switching model of the 'station' dc-dc converter. Due to the switching action of the dc-dc converters, the input current into the 'station' dc-dc converter contains huge amount of ripple components. Likewise, the voltage of the input capacitor also contains large ripples, though its average value is well kept constant at 50 kV. This implies that the input voltage control method designed for the 'station' dc-dc converter also has satisfactory performance under the input current disturbance and switching conditions.
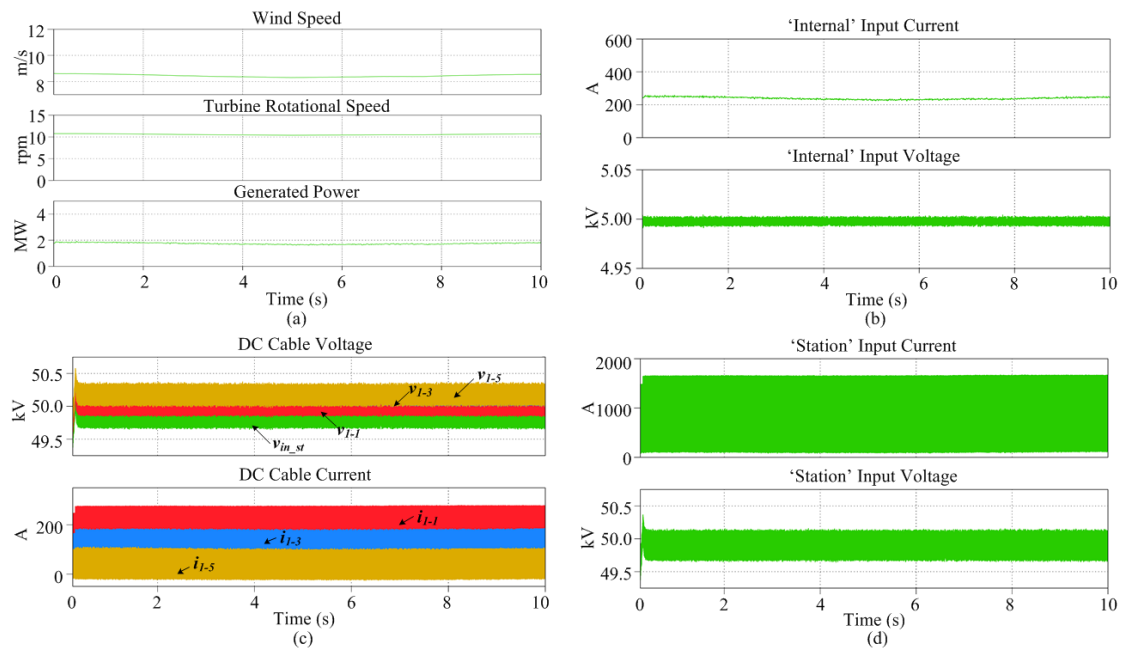

Fig. 4.13. Simulation waveforms of the "switching" model of the 150 MW dc-grid wind farm: (a) wind turbine (WT$_{1-5}$), (b) 'internal' dc-dc converter (WT$_{1-5}$), (c) dc-cable, and (d) 'station' dc-dc converter.

Fig. 4.14 shows the enlarged waveforms at 5 *s* for the duration of one switching period of the dc-dc converter (1 *ms*). As can be seen from the figure, the enlarged waveforms offer more detailed information such as the magnitude and frequency of the ripples. For example, Fig. 4.14(c) shows the dc cable currents whose frequencies are 6 times as high as the switching frequency owing to the output current characteristics of the 3-parrallel-connected SAB converters. It can also be observed that the peaks of dc cable currents at different positions have delays among them owing to the dc cable inductance. Based on such

detailed information under different input wind scenarios, actual stresses on the active and passive components of the system can be determined. Consequently, the optimized design requirements for the essential components of the dc-grid wind farm might be obtained by studying this simulation model further.
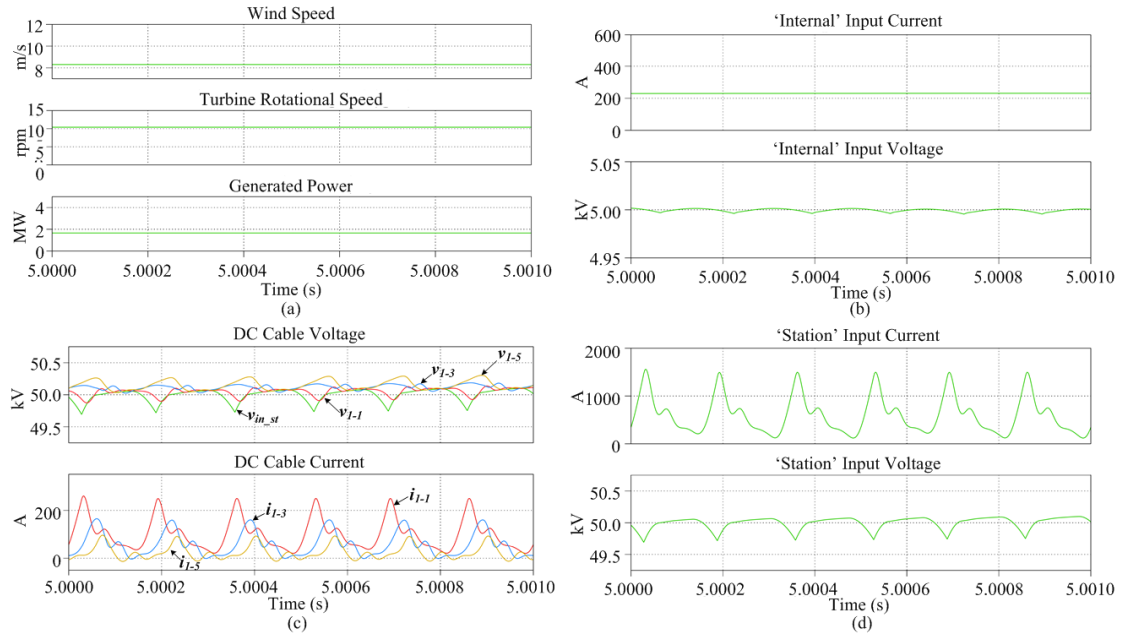

Fig. 4.14. Enlarged simulation waveforms of the "switching" model of the 150 MW dc-grid wind farm: (a) wind turbine (WT$_{1-5}$), (b) 'internal' dc-dc converter (WT$_{1-5}$), (c) dc-cable, and (d) 'station' dc-dc converter.

4.6 Summary

In this chapter, modelling and control of a dc-grid wind farm using the PCSAB dc-dc converters have been presented. The control of the dc-grid wind farm have been developed based on the obtained models and evaluated through various simulation studies. From the simulation studies, it is clear that the average model and the switching model have their own merits. The average model considers only the average characteristics of the system, so that the simulation requires much less simulation time and provides insight into the overall performance of the system. Hence, it is thought to be more suitable for tuning various controllers in the system. Meanwhile, the switching model provides much detailed information, such as actual peak values of the ripple components, though it requires much longer simulation time. Therefore, it is thought to be more suitable for selecting power devices and designing filters in the system. The developed models and control methods in this

106

chapter are expected to be useful for further studies on the operation of the dc-grid wind farm under various input wind speeds and/or fault conditions.

References

[1]   C. Meyer, M. Höing, A. Peterson, and W.D. Doncker, "Control and design of dc grids for offshore wind farms," IEEE Trans. on Industry Applications, vol. 43, no. 6, pp. 1475-1482, Feb. 2007.

[2]   J. Robinson, D. Jovcic, and G. Joos, "Analysis and design of an offshore wind farm using a MV DC grid," IEEE Trans. on Power Delivery, vol. 25, no. 4, pp. 2164-2173, Oct. 2010.

[3]   G. Ortiz, J. Biela, and J.W. Kolar, "Optimized design of medium frequency transformers with high isolation requirements" in Proc. IECON 2010 – 36th Annual Conference on IEEE Industrial Electronics Soc., pp. 631-638, 2010.

[4]   F. Deng and Z. Chen, "Control of improved full-bridge three-level dc/dc converter for wind turbines in a dc grid," IEEE Trans. on Power Electronics, vol. 28, no. 1, pp. 314-324, Jan. 2013.

[5]   W. Chen, A. Huang, C. Li, G. Wang, and W. Gu, "Analysis and comparison of medium voltage high power dc/dc converters for offshore wind energy systems," IEEE Trans. on Power Electronics, vol. 28, no. 4, pp. 2014-2023, Apr. 2013.

[6]   N. Denniston, A. Massoud, S. Ahmed, and P. Enjeti, "Multiple-module high-gain high-voltage dc–dc transformers for offshore wind energy systems," IEEE Trans. on Industrial Electronics, vol. 58, no. 5, pp. 1877-1886, May, 2011.

[7]   L. Max and S. Lundberg, "System efficiency of a DC/DC converter-based wind farm," Wind Energy, vol. 11, pp. 109-120, Oct. 2008.

[8]   K. Park and Z. Chen, "Analysis and design of a parallel-connected single active bridge dc-dc converter for high-power wind farm applications" in Proc. European Conference on Power Electronics and Applications (EPE), pp. 1-10, Sep. 2013.

[9]   K. Park and Z. Chen, "Open-circuit fault detection and tolerant operation for a parallel-connected SAB dc-dc converter" in Proc. Applied Power Electronics Conference and Exposition (APEC), pp. 1966-1972, Mar. 2014.

[10]   E. Muljadi and C.P. Butterfield, "Pitch-controlled variable-speed wind turbine generation," IEEE Trans. on Industry Apllications, vol. 37, no. 1, pp. 240-246, Jan/Feb 2001.

[11]   D.W. Novotny and T.A. Lipo, Vector control and dynamics of ac drives, ISBN:0198564392, Oxford University Press; Sep. 1996.

[12]   P. Karlsson and J. Svensson, "DC bus voltage control for a distributed power system," IEEE Trans. on Power Electronics, vol. 18, no. 6, pp. 1405-1412, Nov. 2003.

[13]   J. Chen, J. Chen, and C. Gong, "Constant-bandwidth maximum power point tracking strategy for variable-speed wind turbines and its design details," IEEE Trans. on Industrial Electronics, vol. 60, no. 11, pp. 5050-5058, Nov. 2013.

[14]   K.J. Astrom and B. Wittenmark, *Adaptive control*, ISBN: 0201558661, Prentice Hall; 2nd edition, Dec. 1994.

[15]   V. Blasko and V. Kaura, "A new mathematical model and control of a three-phase ac-dc voltage source converter," IEEE Trans. on Power Electronics, vol. 12, no. 1, pp. 116-123, Jan 1997.

[16]   C. Bajracharya, M. Molinas, J. A. Suul, and T. Undeland, "Understanding of tuning techniques of converter controllers for VSC-HVDC," in Proceedings of NORPIE 2008, Helsinki, Finland, 09-11 June 2008.

[17]   L. Max, "Design and control of a dc collection grid for a wind farm," PhD Thesis, Dep. of Energy and Environment, Chalmers University of Technology, Sweden, 2009.

[18]   A. Mullane, G. Lightbody, and R. Yacamini, "Wind-turbine fault ride-through enhancement," IEEE Trans. on Power Systems, vol. 20, no. 4, pp. 1929-1937, Nov. 2005.

[19]   H.G Jeong and K.B. Lee. "A control scheme to fulfill the grid-code under various fault conditions in the grid-connected wind turbines." Electrical Engineering vol. 96, no.2, pp. 199-210, 2014.

[20]   Horns Rev 2 [online]. Available: http://www.dongenergy.com/hornsrev2

[21]   P. Rosas, "Dynamic influences of wind power on the power system," PhD dissertation, Technical University of Denmark, 2003.

[22]   I. Katic, J. Højstrup, and N. O. Jensen, "A simple model for cluster efficiency" in Proc. Eur. Wind Energy Assoc. Conf., pp. 407–410, 1986

Chapter 5

Conclusions

5.1   Summary of the Thesis

This research project has investigated the control of the Switched Reluctance Generator (SRG) for wind energy applications and the high-power dc-dc converters for dc-grid wind farm applications. Furthermore, modelling and control of an overall dc-grid wind farm have been studied.

Due to the nonlinear characteristics of the SRG, it is very difficult to achieve satisfactory control performance using the traditional linear controllers. To overcome this problem, a new self-tuning FLC based speed controller, which has better adaptability and performance over a wide range of operating conditions, has been proposed. The comparative simulations with a traditional PI controller and in combination with a wind turbine have verified the effectiveness and improvement in performance of the proposed controller.

Furthermore, a new non-unity TSF for torque ripple minimization has been proposed. The proposed method inserts deliberate ripple components into the torque reference to cancel out the actual ripples in the output torque during the high speed operation. In addition, a piecewise quadratic curve is employed to improve the performance further by reducing the rate-of-change of the current reference. The simulation results have shown that the proposed TSF can reduce the torque ripples significantly at high speeds.

High-power dc-dc converters are fundamental and essential components when interconnecting wind turbines using a dc network within a wind farm. Since the success of the dc grids is critically dependent upon the high-power dc-dc converters, two new high-power

dc-dc converter topologies have been investigated in this thesis: the PCSAB dc-dc converter and the DUP converter based dc-dc converter.

First, both the steady-state and dynamic analyses of the PCSAB dc-dc converter have been carried out and various equations describing the steady-state and dynamic characteristics of the converter have been derived. The design and control methods have been proposed based on these equations and verified by means of simulation and experiment. In addition, a new open-circuit fault detection method and its tolerant control strategy have been proposed. The feasibility and effectiveness of the proposed fault detection and fault-tolerant methods also have been verified by simulations and experiments.

Furthermore, to realize a more practical dc-dc converter with low power losses and small filtering inductance, a new DUP converter based dc-dc converter and its design and control methods have been proposed. To verify the effectiveness of the converter for the high-power applications, a comparative analysis especially for the dc-grid wind farm application has been performed. The proposed converter not only requires the least filtering inductance, but also has the least power losses in the semiconductor devices. Therefore, the proposed converter is expected to be highly beneficial for high-power applications. A small-scaled prototype and its experimental results have also verified the operational principle of the proposed converter.

Finally, modelling and control of a dc-grid wind farm using the PCSAB dc-dc converters have been presented in this thesis. The control of the dc-grid wind farm have been developed based on the obtained models and evaluated through various simulation studies. The developed models and control methods in this thesis are expected to be useful for further studies on the operation of the dc-grid wind farm under various input wind speeds and/or fault conditions.

5.2 Future Work

Some other interesting and relevant topics are identified during the process of the research work. The important research topics that could be considered for further investigation in the future are listed as follows.

1) In this research, two control methods for the SRG have been proposed and their feasibility and effectiveness have been verified only by simulation studies. To verify the performance of the proposed control methods in actual applications,

experimental studies could be carried out using a prototype of the SRG system which is already built in the laboratory.

2) The high current ripple problem of the SRG has been tackled only by a control approach in this thesis. However, a mechanical design approach, such as excitation assistance or multi-layered structure of the SRG, or the combination of the control and mechanical design approaches could be used to solve the problem more effectively.

3) There are still no operating high-power (above several MWs) SRG for wind energy application. More studies on achieving a SRG with high power density could be an interesting topic.

4) The prototypes for the dc-dc converters introduced in this thesis have been built and various experimental studies have been carried out. However, the voltage and power levels of the prototypes were suitable only for verifying the operational principles. More useful and practical information and experience could be achieved by scaling up the prototypes.

5) The modelling and control of an overall dc-grid wind farm have been developed in this thesis. Further studies on the operation of the dc-grid wind farm under various input wind speeds and/or fault conditions could be carried out using the developed models and control methods.